

INTEGRATED NEUROMUSCULOSKELETAL MODELING WITHIN A FINITE
ELEMENT FRAMEWORK TO INVESTIGATE MECHANISMS AND TREATMENT
OF NEURODEGENERATIVE CONDITIONS

by

Victoria L. Volk



A dissertation

submitted in partial fulfillment

of the requirements for the degree of

Doctor of Philosophy in Materials Science and Engineering

Boise State University

August 2022

© 2022

Victoria L. Volk

ALL RIGHTS RESERVED

BOISE STATE UNIVERSITY GRADUATE COLLEGE

DEFENSE COMMITTEE AND FINAL READING APPROVALS

of the dissertation submitted by

Victoria L. Volk

Dissertation Title: Integrated Neuromusculoskeletal Modeling within a Finite Element Framework to Investigate Mechanisms and Treatment of Neurodegenerative Conditions

Date of Final Oral Examination: 18 April 2022

The following individuals read and discussed the dissertation submitted by student Victoria L. Volk, and they evaluated the student's presentation and response to questions during the final oral examination. They found that the student passed the final oral examination.

Clare Fitzpatrick, Ph.D. Chair, Supervisory Committee

Scott Phillips, Ph.D. Member, Supervisory Committee

Trevor Lujan, Ph.D. Member, Supervisory Committee

Paul Rullkoetter, Ph.D. Member, Supervisory Committee

The final reading approval of the dissertation was granted by Clare Fitzpatrick, Ph.D., Chair of the Supervisory Committee. The dissertation was approved by the Graduate College.

DEDICATION

To my Mom.

For her love, belief in me, and always telling me to *Be Like the Sun*.

ACKNOWLEDGMENTS

Many thanks need to be given to a large group of individuals who have helped support, guide, and encourage me throughout my time working on this research. First and foremost is my graduate advisor, Dr. Clare Fitzpatrick. I cannot begin to express my thanks to you for your unwavering guidance and belief in my ability to become a researcher. To the rest of my committee, I sincerely appreciate your support and direction.

My thanks to my family and friends over the last few years is beyond description. I am extremely grateful to my parents, siblings, and boyfriend for being there for me when I needed you and for always encouraging me to be the best version of myself.

Research is a team effort and without the team of collaborators who contributed to these projects, it would not have been possible. I want to thank all my collaborators for sharing your expertise and valuable work.

Thanks also to my past and present fellow researchers in the Computational Biosciences Lab for the cherished time spent together and for loving my dog, Winston.

I gratefully acknowledge this work was supported by (1) the National Science Foundation Graduate Research Fellowship Program under Grant No. 1946726, (2) the NIH National Institute of Arthritis and Musculoskeletal and Skin Diseases, National Institute of Biomedical Imaging and Bioengineering, and the National Institute of Child Health and Human Development grant U01 AR072989, (3) Medtronic, and (4) the NIH Grant Nos. P20GM109095 and P20GM103408 and NSF Grant No. DUE-1644233.

ABSTRACT

Neurodegenerative and neurodevelopmental disorders are a group of conditions that stem from irregularities in the nervous system that lead to complications in function and movement. The goal of this work is to develop computational tools that: (1) measure the accuracy of surgical interventions in neurodegenerative and neurodevelopmental conditions, and (2) integrate neural and musculoskeletal frameworks to provide a platform to better investigate neurodegenerative and neurodevelopmental disorders. Parkinson's disease (PD) is a neurodegenerative condition projected to affect over 1.2 million people by 2030 in the US. It is caused by atypical firing patterns in the basal ganglia region of the brain that leads to primary motor symptoms of tremor, slowness of movement, and rigidity. A potential treatment for PD is deep brain stimulation (DBS). DBS involves implanting electrodes into central brain structures to regulate the pathological signaling. Electrode placement accuracy is a key metric that helps to determine patient outcomes postoperatively. An automated measurement system was developed to quantify electrode placement accuracy in robot-assisted asleep DBS procedures (Chapter 2). This measurement system allows for precise metrics without human bias in large cohorts of patients. This measurement system was later modified to measure screw placement accuracy in spinal fusion procedures for the treatment of degenerative musculoskeletal conditions (Chapter 3).

DBS is an effective treatment for PD, but it is not a cure for the cause of the disease itself. To cure neurodegenerative and neurodevelopmental diseases, the

underlying disease mechanisms must be better understood. A major limitation in studying neural conditions is the infeasibility of performing in vivo experiments, particularly in humans due to ethical considerations. Computational modeling, specifically fully predictive neuromusculoskeletal (NMS) models, can help to accumulate additional knowledge about neural pathways that cannot be determined experimentally. NMS models typically include complexity in either the neuromuscular or musculoskeletal system, but not both, making it difficult or infeasible to investigate the relationship between neural signaling and musculoskeletal function. To overcome this, a fully predictive NMS model was developed by integrating NEURON software within Abaqus, a finite element (FE) environment (Chapter 4). The neural model consisted of a pool of motor neurons innervating the soleus muscle in a FE human ankle model. Software integration was verified against previously published data, and the neuronal network was verified for motor unit recruitment and rate coding, which are the two principles required for in vivo muscle generation. To demonstrate the applicability of the model to study neurodegenerative and neurodevelopmental diseases, a fully predictive mouse hindlimb NMS model was developed using the integrated framework to investigate Rett syndrome (RS) (Chapter 5). RS is a neurodevelopmental disorder caused by a mutation of the *Mecp2* gene with hallmark motor symptoms of a loss of purposeful hand movement, changes in muscle tone, and a loss of speech. Recent experimental analysis has found that the axon initial segment (AIS) in mice that model RS has torsional morphology compared to wildtype littermate controls. The effects these neural morphological changes have on joint motion will be studied using the mouse NMS model. This work encompasses a range of research that uses computational models to study the underlying mechanisms

and design targeted treatment options for neurodegenerative and neurodevelopmental disorders. The outcomes of this work have quantified the accuracy at which surgical interventions for these conditions can be performed and have resulted in a neuromusculoskeletal model that can be applied to understand how neural morphology, and associated changes due to these disorders, affects musculoskeletal function.

TABLE OF CONTENTS

DEDICATION	iv
ACKNOWLEDGMENTS	v
ABSTRACT	vi
LIST OF TABLES	xii
LIST OF FIGURES	xiii
LIST OF ABBREVIATIONS	xviii
CHAPTER ONE: INTRODUCTION	1
1.1 Background.....	1
1.2 Application of Automated Measurement System	13
1.3 Summary of Scientific Contributions.....	18
CHAPTER TWO: ELECTRODE PLACEMENT ACCURACY IN ROBOT-ASSISTED ASLEEP DEEP BRAIN STIMULATION*	20
Abstract	22
2.1 Introduction.....	22
2.2 Materials and Methods	26
2.2.1 Patient Inclusion and Demographics	26
2.2.2 Surgical Procedure.....	27
2.2.3 Electrode Accuracy.....	31
2.3 Results	34
2.4 Discussion.....	37

2.5 Author Justification.....	42
CHAPTER THREE: PEDICLE SCREW PLACEMENT ACCURACY IN ROBOT-ASSISTED SPINAL FUSION IN A MULTICENTER STUDY*	
Abstract.....	46
3.1 Introduction.....	47
3.2 Materials and Methods.....	49
3.2.1 Patient Inclusion and Demographics.....	49
3.2.2 Surgical Procedure.....	50
3.2.3 Screw Placement Accuracy.....	51
3.2.4 Measurement Uncertainty.....	53
3.2.5 Grading Scale Placement Accuracy.....	55
3.2.6 Manual Measurement Comparison.....	56
3.2.7 Statistical Metrics.....	56
3.3 Results.....	56
3.4 Discussion.....	60
3.5 Conclusions.....	64
3.6 Acknowledgements.....	64
3.7 Author Justifications.....	65
CHAPTER FOUR: INTEGRATION OF NEURAL ARCHITECTURE WITHIN A FINITE ELEMENT FRAMEWORK FOR IMPROVED NEUROMUSCULOSKELETAL MODELING*	
Abstract.....	68
4.1 Introduction.....	68
4.2 Methods.....	72
4.2.1 Verification of Software Integration.....	75

4.2.2 Verification of in vivo Neural Behavior	76
4.2.3 Incorporation of Tissue Mechanics Predictions	78
4.3 Results	78
4.3.1 Verification of in vivo Neural Behavior	79
4.3.2 Incorporation of Tissue Mechanics Predictions	82
4.4 Discussion.....	83
4.5 Data Availability.....	87
4.6 Acknowledgements	87
4.7 Author Justification.....	88
 CHAPTER FIVE: NEUROMUSCULOSKELETAL MOUSE HINDLIMB MODEL TO STUDY THE EFFECT OF NEURAL CHANGES IN INDIVIDUALS WITH NEURODEVELOPMENTAL DISORDERS.....	 89
5.1 Background.....	90
5.2 Finite Element Model Development	92
5.3 Neural Model Development	95
5.3.1 Neuron Morphology Changes	98
5.4 Current Status.....	99
5.5 Ongoing Work	100
5.6 Discussion.....	102
5.7 Acknowledgements	105
5.8 Author Justification.....	105
 CHAPTER SIX: CONCLUSION	 106
REFERENCES.....	111

LIST OF TABLES

Table 2.1	Electrode Placement Accuracy Values (mean \pm SD).....	36
Table 3.1	Screw Placement Accuracy Values Based on Spinal Region (mean \pm SD). Statistical significance ($p < 0.05$) indicated by *.....	57
Table 3.2	Manual Measurement Screw Placement Accuracy Values (mean \pm SD). Statistical significance ($p < 0.05$) indicated by * (between manual 1 and manual 2), ^x (between manual 1 and automated), and ^{II} (between manual 2 and automated).....	60

LIST OF FIGURES

Figure 1.1	Implanted components during DBS procedure. Reproduced from Levine. ¹³3	3
Figure 1.2	Axial T1 MRI slice showing segmented STN (green), GPi (orange), and Vim (pink). Reproduced from Kruger et al. ¹⁴3	3
Figure 1.3	Radial error between implanted electrode (red) compared to the target location (blue) within the clinically acceptable metric of less than 2 to 3 mm of deviation. Shown is an axial MRI slice zooming in on the electrode from left to right.4	4
Figure 1.4	EMG data-driven model using a rigid-body musculoskeletal simulation. Reproduced from Sartori et al. ²¹7	7
Figure 1.5	Finite element musculoskeletal model of the lower limb from the lumbar spine to the toes shown in the coronal (left) and sagittal (right) views. Soft tissue inclusions can be seen at the knee and lumbar spine.....8	8
Figure 1.6	Fully predictive NMS model of a pool of motor neurons (one shown here for simplicity) innervating the soleus muscle of a three-dimensional FE model of the ankle.10	10
Figure 1.7	Axon initial segment of golgi impregnated pyramidal neurons to show increased tortuosity in mice with <i>Mecp2</i> mutations representative of RS (left) compared to wildtype littermate controls (right). ⁴⁵12	12
Figure 1.8	Components included in the integrated NMS mouse hindlimb model. NEURON simulations include pyramidal cells and motor neurons. Abaqus FE model geometry is of a mouse hindlimb from the pelvis to foot.....12	12
Figure 1.9	Lumbar spinal fusion performed using pedicle screws to hold an interbody graft in place. Reproduced from Chen et al. ⁵¹14	14
Figure 1.10	CT scans detailing the Gertzbein and Robbins classification used to grade pedicle screw accuracy. Reproduced from Schlato et al. ⁵³15	15
Figure 1.11	O-Arm scan showing implanted pedicle screws (left). Left (yellow) and right (blue) screw preoperative plans overlain on O-Arm scan (right). Shown in all three anatomical views: axial (a), sagittal (b), and coronal (c).	

	Accuracy is measured between the implanted screw and the target location for each implant.	18
Figure 2.1	(a) Preoperative T2 MRI acquired with a 1.5 Tesla machine under general anesthesia (top), with preoperative cannula trajectory plan for the right STN shown in blue (bottom). (b) Intraoperative CT (including fiducial frame for orientation of the renaissance system). (c) Fusion of MR and CT scans; transparent overlay of T2 MRI and intraoperative CT (top), intraoperative CT with T2 MRI shown within window (bottom). (d) Intraoperative CT with preoperative plan mapped from the fused MRI shown in blue. Sagittal and axial images that pass through the right STN are shown in each instance.	28
Figure 2.2	(a) Fiducial frame attached to the robotic base that allows the software to orient the Renaissance system. (b) Robot positioned on the base with arm attached. The arm is oriented over the target insertion point so that the precise location can be marked on the scalp.	29
Figure 2.3	A secondary intraoperative CT is obtained after placement of the cannula; the right cannula is shown here in sagittal (top, left), axial (top, right), and coronal (bottom, left) views.	30
Figure 2.4	Series of intraoperative CT scans performed during bilateral surgery. (a) Fiducial CT for registration of the Renaissance robotic system with the preoperative MRI. (b) Verification CT after placement of the left cannula. (c) Verification CT after placement of the right cannula.	31
Figure 2.5	Verification CT viewed along the length of (left) and perpendicular to (right) the planned trajectory of the right cannula. Placement accuracy measurements are made from the view along the length of the planned trajectory.....	32
Figure 2.6	Overlay of the preoperative MRI with target trajectory (blue) and verification CT cannula placement (red). Close-up with 5.0 mm reference scale bar shown on the right – this image was used to measure the difference between center of the target site and the center of the implanted cannula. Images are shown looking along the target cannula trajectory...	33
Figure 2.7	(a) Measurement of MRI-CT fusion error. Preoperative MRI with target cannula trajectory (blue dashed line). (b) Close-up showing apparent location of the center of the cannula from verification CT fused with fiducial CT (red) and apparent location of the center of the cannula from verification CT fused directly with MRI (green). Fusion error is defined as the distance between these locations.....	34

Figure 2.8	Implication of MRI-CT fusion error. To ensure accurate placement, the target (blue) must be wholly within the cannula region (red). When the average MRI-CT fusion deviation (blue dashed) is accounted for, the probability that the placement is not fully within the target region can be calculated (green striped region).40
Figure 3.1	(a) Registration of the robotic platform in the operating room. AP and Oblique intraoperative x-ray images are taken of the patient's bony anatomy and the amber-colored frame attached to the robot arm positioned over the patient's body. These images establish the patient's anatomy and relate it back to the preoperative scan used to plan the screw placements. (b) Placement of percutaneous screws through the robotic end effector with real-time navigation on the guidance system screen.51
Figure 3.2	Metrics used to determine pedicle screw placement accuracy. All measures are determined as the deviation between the planned target screw location (red lines and dots) and implanted screw location (blue lines and dots). (a) Superior-inferior (SI) and medial-lateral (ML) deviation in the pedicle region measured in the coronal plane. Perpendicular deviation in the (b) axial and (d) sagittal planes from the base of the screw tulip to the implanted screw trajectory. Angular deviation in the (c) axial and (e) sagittal planes measured as the angle between the trajectories of the planned and implanted screw locations....52
Figure 3.3	Fusion of intra- or postoperative images to preoperative CT scans in the (a) axial and (c) sagittal views. The postoperative image showing the implanted screw locations is displayed inside of the red circle. The planned locations for the screws, with the left implant shown in yellow and the right implant shown in blue, are overlain on the postoperative image in the (b) axial and (d) sagittal views.54
Figure 3.4	(a) Target screw location (red) in relation to the implanted screw (outlined in blue) when looking from the coronal plane into the pedicle region with the average ML and SI deviation for the entire cohort shown. (b) Fusion uncertainty (dashed red) associated with the portion of the measurement process that involves fusing the preoperative CT to the intra- or postoperative scan. (c) One standard deviation (green) of the ML and SI measurements of the entire dataset. The area inside of the green dashed oval accounts for all variability in the measurement process.58
Figure 3.5	Measurement differences between accuracy of the implanted screw (blue) in relation to the planned location (red) versus conventional grading scale metrics. The pedicle edge (green dashed line) is shown that was used to judge placement outside of the pedicle region. (a) Categorized as A using grading scale but has a ML deviation of 3.21 mm away from the planned target location. (b) Grading scale category B with a ML deviation of 7.38

	mm from the planned location. (c) Grading scale category C and a ML deviation from the target trajectory of 5.14 mm.....	61
Figure 4.1	(a) 2D and (b) 3D representations of alpha motor neuron.	73
Figure 4.2	Abaqus musculoskeletal model of the ankle joint including geometries of the bones, muscles, and cartilage.....	74
Figure 4.3	Flow of information in the integrated FE NMS model. A NEURON simulation is ran using a call from the Abaqus-specific Fortran user-subroutine every 100 ms. From that simulation, the activation is input into the muscle force calculation. The force is then applied to the soleus muscle in the Abaqus musculoskeletal model.....	75
Figure 4.4	(a, b) Input activation profiles from Kim ¹⁰⁸ implemented in the single neuron NMS model to show software integration. (c, d) Neuromuscular muscle force results from Kim ¹⁰⁸ (Figures 3B and 4B), reproduced here using publicly available data from ModelDB ¹⁰⁵ . (e, f) Muscle force outputs from FE NMS simulations at lengthened, optimal, and shortened muscle lengths.	76
Figure 4.5	(a-c) Discharge times for every 20 th motor unit (dashes) with resulting output muscle force (solid line). Motor unit 1 is the smallest and motor unit 310 is the largest, with an exponential size distribution. The stimulation profile increased linearly for two seconds until reaching the peak amplitude corresponding to that %MVC, after which point it was held constant for two seconds. (d-f) Interspike interval measurements between each subsequent discharge for every motor unit through the length of the simulation. Intervals with less than five occurrences were not included in the figure for visualization.	80
Figure 4.6	(a-c) Discharge times for every 20 th motor unit (dashes) with resulting output muscle force (solid line). The stimulation profile increased linearly for two seconds until reaching the peak amplitude corresponding to that %MVC, after which point it decreased linearly back to baseline over two seconds. (d-f) Interspike interval measurements between each subsequent discharge for every motor unit through the length of the simulation. Intervals with less than five occurrences were not included in the figure for visualization.	81
Figure 4.7	(a) Discharge times for every 20 th motor unit (dashes) with resulting muscle force output (solid line). The stimulation profile increased linearly for one second until reaching the peak amplitude corresponding to 10% MVC, after which point it was held constant for two seconds. (b) Discharge rate, in pulses per second, of motor units 40 and 60 over the	

	course of the simulation, showing the relationship between intensity and discharge rate to demonstrate rate coding.....	82
Figure 4.8	(a) Contour map showing contact pressure on the tibia articular cartilage during ankle plantarflexion. The region of higher contact pressure is located posteriorly. (b) Plantarflexed position of the tibia-talus joint.....	83
Figure 5.1	Three-dimensional bone and cartilage geometries were segmented from a mouse uCT scan.	93
Figure 5.2	Abaqus FE musculoskeletal geometries from the pelvis to the foot. Articular cartilage is included at the knee.	94
Figure 5.3	Contour map showing contact pressure on the femur articular cartilage at the tibiofemoral joint during the propulsion phase of the gait cycle.....	95
Figure 5.4	Three-dimensional representations of the pyramidal cell and motor neuron geometries included in the neural portion of the integrated NMS model..	97
Figure 5.5	(a) Healthy wildtype AIS compared to (b) AIS with increased tortuosity, a morphological change associated with RS.	98
Figure 5.6	(a) Point cloud of vertices (blue) from STL segmentation of AIS fit with a line-of-best-fit (red). (b) Normalization of point cloud to 30 centroids (blue) along length of AIS. The arc-to-chord ratio is the Euclidian distance between the centroids (blue line) divided by the length of the line-of-best-fit (red).....	99
Figure 5.7	Flow of information in integrated NMS model. A NEURON simulation runs for a set amount of time, which is 100 ms in this example. The activation from NEURON is input into the muscle force calculation. The force is then applied to the quadriceps muscles in the Abaqus musculoskeletal mouse model.....	101

LIST OF ABBREVIATIONS

PD	Parkinson's Disease
DBS	deep brain stimulation
STN	subthalamic nucleus
GPI	globus pallidus interna
Vim	ventralis intermedius
NMS	neuromusculoskeletal
EMG	electromyography
FE	finite element
RS	Rett syndrome
Mecp2	methyl-CpG-binding protein 2
AIS	axon initial segment
LSF	lumbar spinal fusion
CT	computed tomography
MRI	magnetic resonance image
MER	microelectrode recordings
UPDRS	Unified Parkinson's Disease Rating Scale
ML	medial-lateral
SI	superior-inferior
EEG	electroencephalography
RMSE	root mean square error

NetPyNE	Networks in Python and NEURON
MVC	maximum voluntary contraction
uCT	micro computed tomography
ID	intellectual disability

CHAPTER ONE: INTRODUCTION

1.1 Background

Neurodegenerative and neurodevelopmental disorders are a group of conditions that stem from irregularities in the nervous system that lead to complications in function and movement. Neurodegenerative conditions are associated with aging, and become progressively worse as the person ages. Approximately 50 million people in the United States are living with a neurological condition according to the National Institute of Neurological Disorders and Stroke, and as the median age demographic rises, this number will continue to increase.¹ Three major neurodegenerative conditions are Alzheimer's disease, Parkinson's disease, and amyotrophic lateral sclerosis.² These previous conditions currently have no cure, but there are treatment options that can help alleviate some symptoms.² Neurodevelopmental disorders occur during early brain development and most are diagnosed during childhood. As of 2008, approximately 1 in 6 children in the United States has a developmental disability with prevalence increasing from 12.84% to 15.04% over a 12-year period.³ Examples of these conditions include autism spectrum disorders, attention deficit/hyperactivity disorder, intellectual disability, and Rett syndrome.^{4,5} Neurodegenerative and neurodevelopmental disorders are caused by both genetic and environmental factors, and significant research is being done to better understand the modalities by which these conditions occur to develop treatment options and find cures.

Parkinson's Disease (PD) is a neurodegenerative condition that affected 1.04 million people in 2017 in the United States alone.⁶ This number is projected to be over 1.2 million people by 2030.⁷ The cause of PD is not entirely known but both genetic and environmental factors are thought to contribute to PD etiology.² Patients with PD experience a progress loss of movement due to impairments in the basal ganglia region of their brain. The primary motor symptoms are tremor, dystonia, rigidity, and postural instability.⁸⁻¹¹ Tremor is shakiness that commonly occurs in the hands, and sometimes the legs or lower part of the face.¹⁰ Akinesia, or bradykinesia, is when movement becomes slow and is especially pronounced during activities of daily living when fine motor skills are needed.¹⁰ Rigidity involves stiffening of the limbs and can sometimes be painful for the patient.¹⁰ Postural instability presents itself in a variety of abnormal deformities of posture, with a common one involving a more forward angled trunk and bent legs.¹⁰

There is no known cure for PD, but there are treatment options that can help to alleviate symptoms. Medications have been developed that target dopamine receptors in the brain. There is also a surgical procedure called deep brain stimulation (DBS) that has been shown to alleviate the primary motor symptoms of PD (Figure 1.1). DBS involves implantation of electrodes into central brain structures to send pulsed, high frequency electrical currents to that region to normalize atypical neuron firing patterns. There are three different regions in the brain that are targeted as part of DBS: subthalamic nucleus (STN), globus pallidus interna (GPi) and ventralis intermedius (Vim) (Figure 1.2). While the STN treats most symptoms of PD, the GPi and Vim are targeted to reduce the effects of dystonia and essential tremor, respectively.¹²

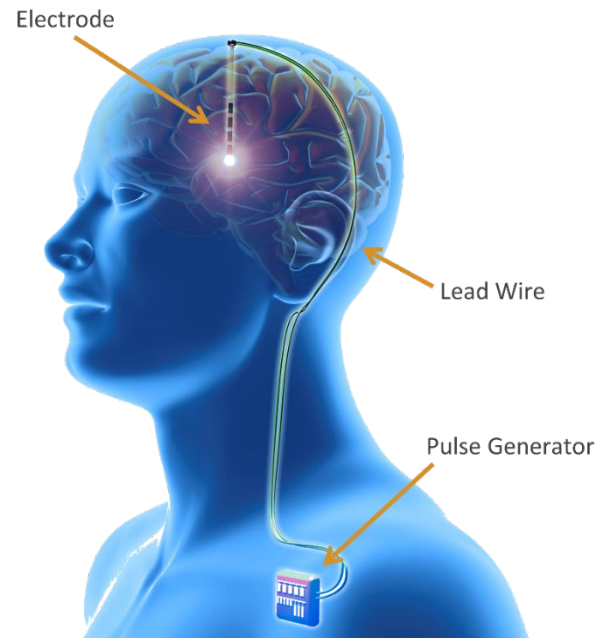


Figure 1.1 Implanted components during DBS procedure. Reproduced from Levine.¹³

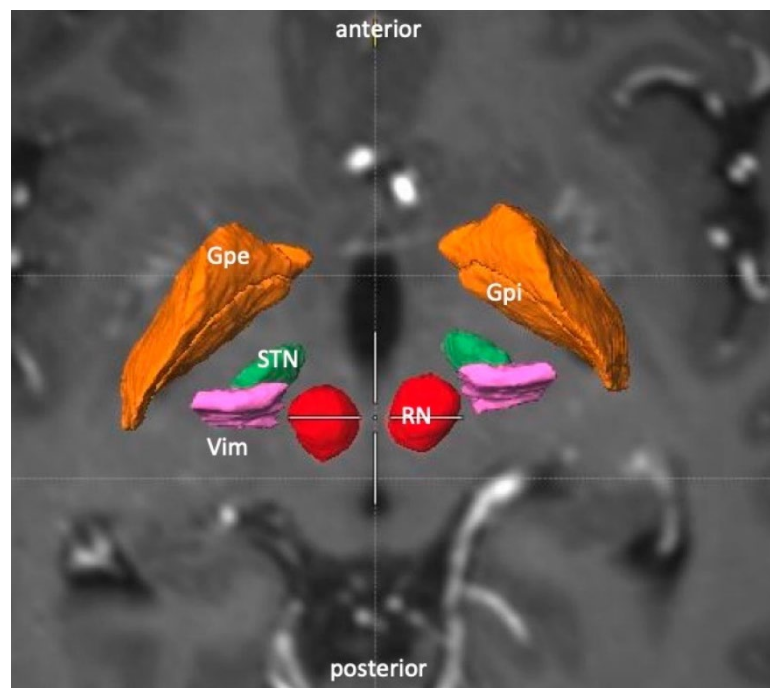


Figure 1.2 Axial T1 MRI slice showing segmented STN (green), GPi (orange), and Vim (pink). Reproduced from Kruger et al.¹⁴

Precise electrode placement is a key factor in the effectiveness of DBS in treating the symptoms of PD. Electrode placement accuracy is measured in the operating room before clinical outcomes can be measured postoperatively. There is debate as to what constitutes sufficient electrode placement accuracy, with some studies re-implanting an electrode if it is farther than 2 to 3 mm away from the target¹⁵, while others state 3 mm as the standard for re-implantation.¹⁶ This deviation is measured as a radial error, or the distance from the center of the implanted electrode to the center of the target electrode trajectory (Figure 1.3).

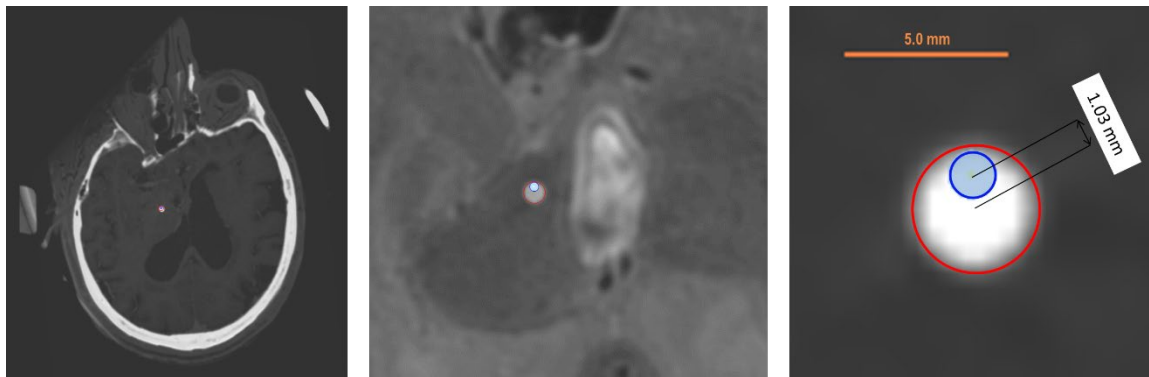


Figure 1.3 Radial error between implanted electrode (red) compared to the target location (blue) within the clinically acceptable metric of less than 2 to 3 mm of deviation. Shown is an axial MRI slice zooming in on the electrode from left to right.

An automated measurement algorithm was developed in MATLAB to accurately measure electrode placement accuracy in DBS (Chapter 2). The automated measurement system allows for the removal of human bias in measurements and enables large cohorts of patients to be studied in less time. An asleep, robot-assisted DBS procedure was verified using this measurement system compared to traditional DBS surgical techniques. The confirmation of precise electrode placement accuracy ensures that DBS will have proper treatment for the motor symptoms of PD. This measurement system was later modified to measure screw placement accuracy in spinal fusion procedures for the

treatment of degenerative musculoskeletal conditions (Introduction Section 1.2, Chapter 3).

DBS is an effective treatment for the motor symptoms of PD by regulating the atypical neuron firing patterns in the basal ganglia region of the brain, but it is not a cure for the cause of the disease itself. To develop treatments to alleviate symptoms or inhibit development of neurodegenerative and neurodevelopmental diseases, the underlying disease mechanisms must be better understood. This first begins with needing to understand the entire process of motion generation in the body from the electrical signal being generated in the brain, the neural drive to muscles, how muscles react to the given stimuli to generate joint movement, and the response back to the brain from the muscles. When healthy neural pathways to muscle are better understood, that knowledge can be applied to musculoskeletal changes occurring due to neurodegenerative and neurodevelopmental conditions. Conversely, musculoskeletal function and movement may be early indicators of neurological changes that could cause neurodegenerative and neurodevelopmental conditions. Therefore, understanding changes in the musculoskeletal components may be used as a prodromal marker for early diagnosis of degenerative neural conditions.

A major limitation in studying neuromusculoskeletal conditions is the challenge of performing in vivo experiments. It is not possible to experimentally measure all important factors, such as tissue stresses and single neuron firing patterns, and experimental studies are not always feasible in humans due to ethical considerations. One way to overcome this limitation is through the development and utilization of neuromusculoskeletal (NMS) models. Due to the complexity of the involved systems,

there are varying levels of neuromuscular and musculoskeletal models within the encompassing NMS modeling frameworks.

Complex NMS models fit into one of two categories: neural data-driven or fully predictive. Neural data-driven models are almost wholly driven using electromyography (EMG) signals as the input into the musculoskeletal model (Figure 1.4).¹⁷⁻²² EMG is collected within the laboratory setting during the movements that will be simulated in the NMS model. The signal is then filtered and processed to extract EMG-linear envelopes, muscle synergies, motor neuron spike trains, or a combination of the above.²³ Neural data-driven models are beneficial for in-depth studies to quantify musculoskeletal function and control²¹ via neural drive, or common synaptic input, to the spinal cord and muscles.¹⁷ However, these EMG driven models inform force production based only on decomposition of discharge times and no other neural anatomy. Also, they only operate in a feed-forward method that does not have feedback from the musculoskeletal system to the nervous system required for the nervous system to adapt during movement.

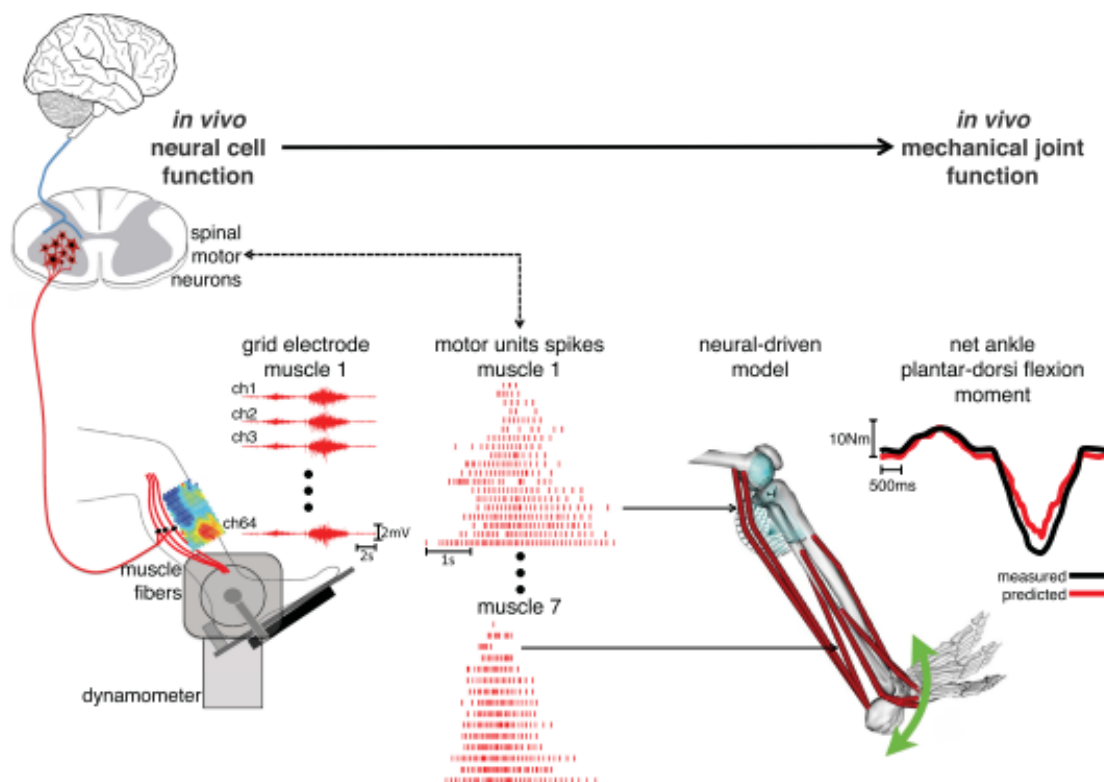


Figure 1.4 EMG data-driven model using a rigid-body musculoskeletal simulation. Reproduced from Sartori et al.²¹

Alternatively, fully predictive NMS models, the second category of complex NMS model types, utilize a pool of motor neurons²⁴⁻²⁶ or neural networks with motor neurons, Renshaw cells, and interneurons²⁷⁻³¹ to simulate a neural command that generates a simulated muscle force used in a musculoskeletal model. This means that the signal being converted into muscle force is based upon a variety of neural factors such as anatomy, types of ion channels, and connectivity between different neurons, which can all be modified to study their effects. Neural factors can be varied throughout the simulation that make the overall outputs representative of the adaptation that occurs in the body. This is a key benefit of fully predictive models, rather than studying musculoskeletal function from a specific neural drive.²³

The two key types of musculoskeletal models that are incorporated within NMS models are rigid body and finite element (FE) models. Rigid body simulations are useful for simulating musculoskeletal dynamics and calculating joint kinematics from experimental data (Figure 1.4).³² For more complex problems such as detailed representations of the joints that include soft tissue geometries and material properties, FE analyses are more useful (Figure 1.5). FE is advantageous over other numerical analyses due to its versatility and flexibility regarding geometry, boundary and loading conditions, and material properties.³³ FE simulation environments (e.g. FEBio, febio.org; Abaqus, Simulia) can be used for both rigid body simulations and more complex FE simulations.

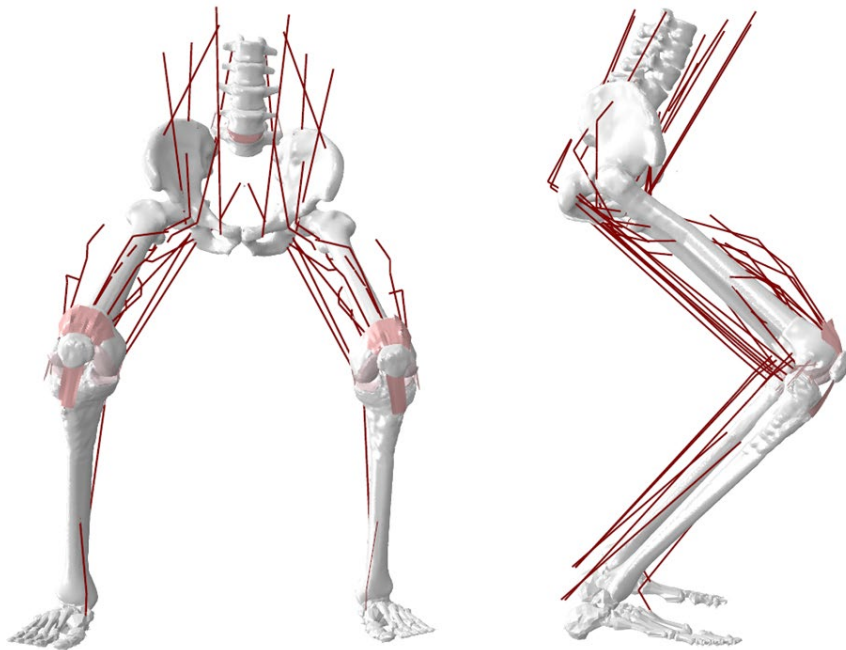


Figure 1.5 Finite element musculoskeletal model of the lower limb from the lumbar spine to the toes shown in the coronal (left) and sagittal (right) views. Soft tissue inclusions can be seen at the knee and lumbar spine.

A primary concern for NMS models, and computational models in general, is the validation process. Both neural and musculoskeletal components can be validated independently against experimental data, but then also must be validated in a fully combined model. Commonly, for neural output validation, the membrane potential (voltage differential) is compared to EMG data, either intramuscular or intrafascicular in animal studies, or surface-mounted EMG in human studies.^{17, 21, 30, 34-36} When surface EMG is recorded, it must be filtered and processed to extract the necessary information for comparing to membrane potentials from the simulation. Musculoskeletal models can be validated against motion capture data,^{17, 21, 30, 35} and ground reaction force data.^{21, 30, 35, 36}

No existing models have incorporated a fully predictive NMS model within a FE framework. A model with varying levels of complexity in both the neuromuscular and musculoskeletal components is necessary to better understand motion generation in the body and to study the mechanisms of neurodegenerative conditions such as PD. This was accomplished in the work presented here through the development of a fully predictive NMS within the Abaqus FE environment (Chapter 4) (Figure 1.6). The neuromuscular component of the model was developed in NEURON, an open-sourced, python-based simulation environment used for the creation of models ranging from single neurons to networks of neurons.³⁷ The Abaqus FE model was a three-dimensional human ankle joint with soleus and tibialis anterior muscles.

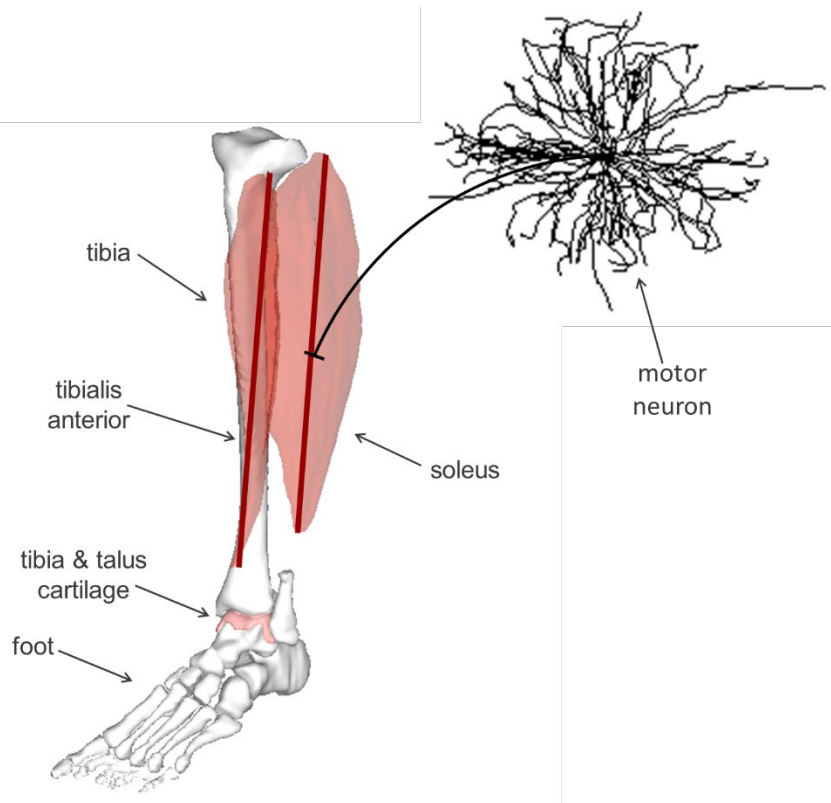


Figure 1.6 Fully predictive NMS model of a pool of motor neurons (one shown here for simplicity) innervating the soleus muscle of a three-dimensional FE model of the ankle.

The integration of the two software platforms was validated against previously published work³⁸ and verified for in vivo muscle generation via the principles of motor unit recruitment and rate coding.³⁹ Motor unit recruitment is the concept that not all motor units (a motor neuron and all the muscle fibers it innervates) are active at a given time, but instead are recruited in an orderly manner.³⁹ Motor units are recruited in size order from smallest to largest, following Henneman's size principle,⁴⁰ where units that generate smaller forces are recruited first followed by larger force producing motor units. Rate coding involves a proportional relationship between stimulation intensity and discharge rate, such that as the intensity of a stimulus increases, so does the rate of discharging action potentials.³⁹ All motor neurons have a recruitment threshold, below

which no action potential will be generated. For stimuli that are above the recruitment threshold, there exists a linear relationship between the level of injected current and the resulting discharge rate. The discharge rate will continue to increase with increased current intensity until the peak rate is achieved. After this point, there is little variation in discharge rate, even with a continued increase in excitatory drive. If a neuromuscular model does not exhibit these two functions, then it cannot replicate muscle force or movement generation in an in vivo manner.

After the development of a fully predictive NMS model within a single software framework, the applicability of the model to study neurodevelopmental and neurodegenerative conditions was tested. To accomplish this, a mouse NMS model was developed to study Rett syndrome (RS) (Chapter 5). RS is a neurodevelopmental disorder caused by a range of genetic mutations on the methyl-CpG-binding protein 2 (*Mecp2*).⁴¹ RS affects 1 out of every 10,000 female births⁴² with the disorder primarily affecting females due to *Mecp2* being located on the X chromosome.⁴³ The primary motor symptoms of RS include a loss of purposeful hand movement, progressive changes in muscle tone, loss of speech, and, in severe cases, difficulty breathing and gait abnormalities.⁴⁴ Recent experimental analysis has found that the axon initial segment (AIS) in mice that model RS has torsional morphology compared to wildtype littermate controls (Figure 1.7).⁴⁵ This change in shape affects the signal travelling from the brain to spinal cord and results in the movement symptoms associated with RS. The NMS model developed within the Abaqus FE environment (Chapter 4) was modified to include three-dimensional geometry of a full mouse hindlimb (Figure 1.8). The neural pathway was expanded to include pyramidal cells representative of the signal generated in the brain

sent to the motor neuron pool in the spinal cord (Figure 1.8). A healthy baseline NMS mouse model was developed for the application of anatomical AIS changes with the intent to study the mechanism and potential treatments of RS.

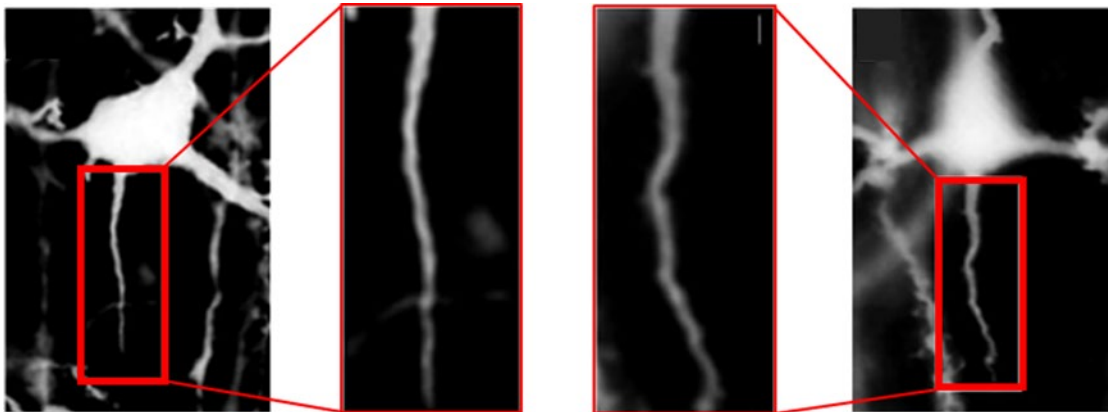


Figure 1.7 Axon initial segment of golgi impregnated pyramidal neurons to show increased tortuosity in mice with *Mecp2* mutations representative of RS (left) compared to wildtype littermate controls (right).⁴⁵

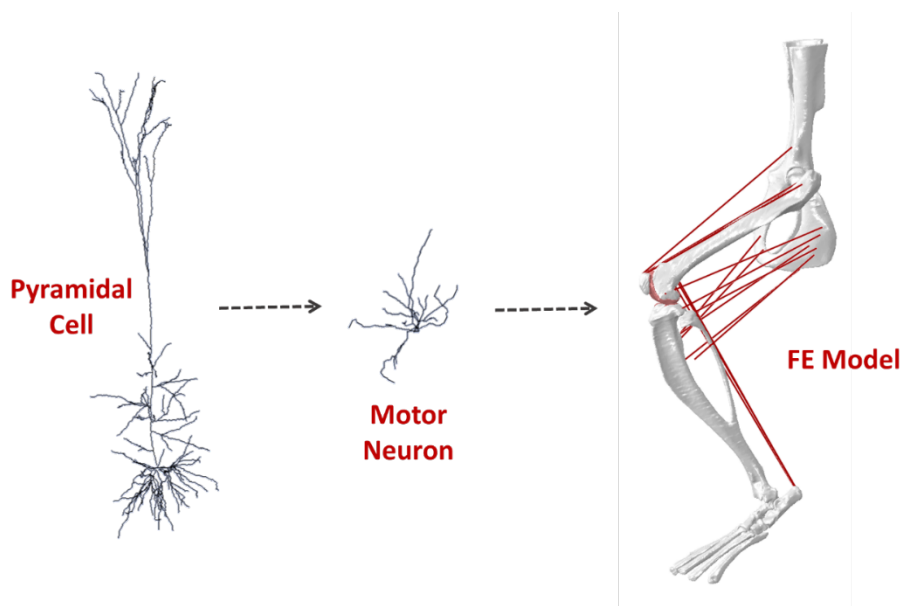


Figure 1.8 Components included in the integrated NMS mouse hindlimb model. NEURON simulations include pyramidal cells and motor neurons. Abaqus FE model geometry is of a mouse hindlimb from the pelvis to foot.

This work encompasses a range of research that uses computational models and algorithms to study the underlying mechanisms and design better treatment options for

neurodegenerative and neurodevelopmental disorders. The analysis of electrode placement accuracy in deep brain stimulation for the treatment of Parkinson's Disease using an automated measurement system (Chapter 2) can help improve patient outcomes with increased electrode placement accuracy based upon the findings. Improved neuromusculoskeletal modeling through the development of a fully predictive neuromusculoskeletal model within a single finite element framework (Chapter 4) can help to better understand healthy muscle control pathways and study disease mechanisms, such as in the neurodevelopmental disorder Rett syndrome (Chapter 5).

1.2 Application of Automated Measurement System

Spinal fusion procedures are used to treat a variety of degenerative musculoskeletal conditions including spondylolisthesis, lumbar stenosis, degenerative disc disease, and scoliosis.⁴⁶⁻⁴⁸ A spinal fusion procedure involves the implantation of pedicle screws into vertebral pedicles to act as anchor points for rods to restrict movement between those vertebrae (Figure 1.9).^{49,50} Degeneration often occurs in the lumbar region of the spine, but fusions can occur at any spinal level depending on the condition. The prevalence of lumbar spinal fusions (LSF) was estimated to be 79.8 per 100,000 individuals with over two million people having undergone a LSF between 2004 and 2015.⁴⁸



Figure 1.9 Lumbar spinal fusion performed using pedicle screws to hold an interbody graft in place. Reproduced from Chen et al.⁵¹

Similar to DBS procedures used for the treatment of PD, screw placement accuracy can be measured in the operating room to determine proper implementation before clinical outcomes can be measured postoperatively. Screw placement accuracy is conventionally measured using grading scales. This involves assigning a letter grade to the placement based on how much deviation occurs outside of the pedicle region. Clinically acceptable placements have 2 mm or less deviation outside the pedicle, which on most grading scales constitutes a grade A or B (Figure 1.10).^{52, 53} Deviations outside of the pedicle in the medial direction lead to breaches into the spinal canal which can cause potential damage to the spinal cord. There are numerous grading scales including Gertzbein and Robbins,⁵² Youkilis,⁵⁴ and Rampersaud.⁵⁵

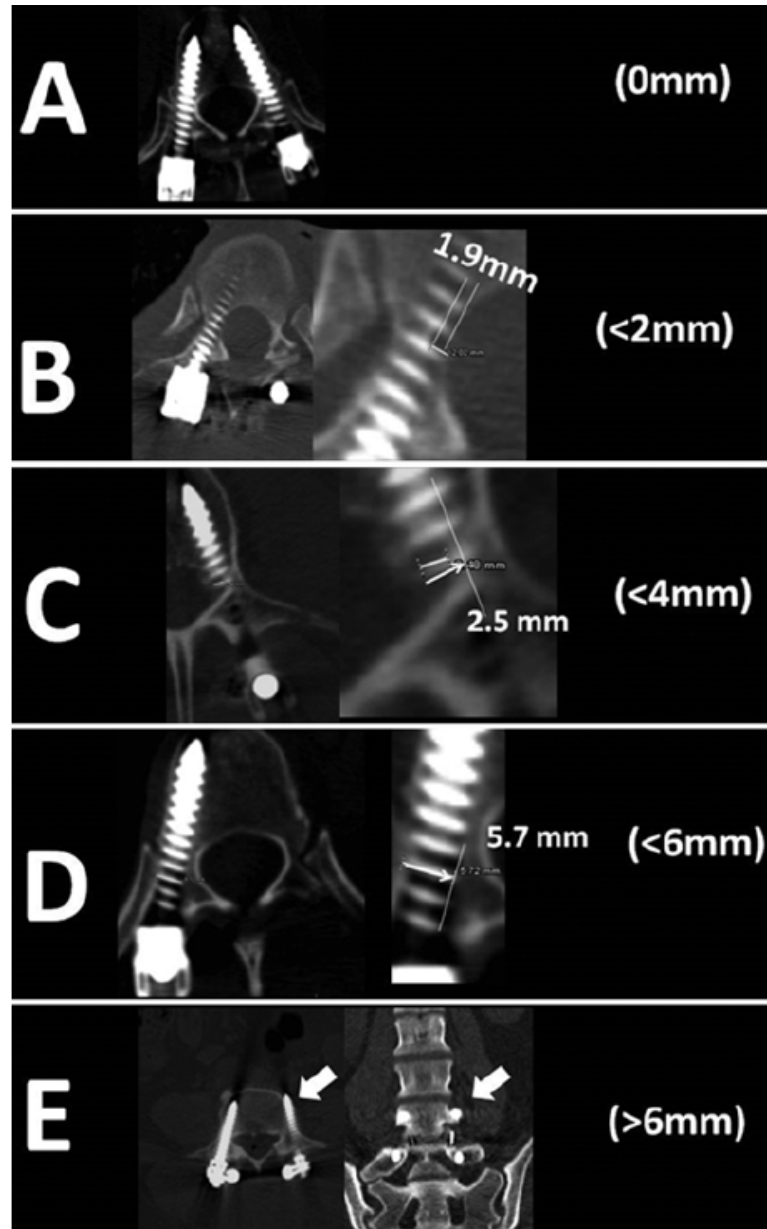


Figure 1.10 CT scans detailing the Gertzbein and Robbins classification used to grade pedicle screw accuracy. Reproduced from Schlato et al.⁵³

Traditional spinal fusion procedures can be performed open or as a percutaneous, minimally invasive procedure. The conventional method for pedicle screw insertion is the freehand method, oftentimes with intraoperative fluoroscopy guidance.⁵⁶ In an effort to improve placement accuracy and clinical outcomes, including operating room time, radiation exposure, and longevity of hospital stay, surgical robots were created to assist in

spinal fusion surgery. There are a variety of robots currently on the market including Renaissance,^{57, 58} Mazor X,^{57, 58} ROSA,^{57, 59}, TINAVI,⁶⁰ and ExcelsiusGPS.⁵⁶ There is a compilation of literature comparing robot-assisted screw placement to the freehand method, with debate as to whether robotic assistance actually leads to an increased accuracy.^{47, 60-63} A review by Ghasem et al. included 12 studies that compared robot-guided surgery to the freehand method and showed that 10 studies did have an increase in placement accuracy when robot-assistance was used.⁵⁷ In one case, there was found to be no difference and one case showed worse accuracy with robotic guidance.⁵⁷ However, it has been shown that procedures utilizing robot-assistance, compared to those without, have a decrease in length of hospital stay^{64, 65} and radiation exposure.^{60, 65-67} These factors are beneficial to patients undergoing a procedure and hospital staff, as well as an associated cost reduction.

The Mazor X Stealth Edition robotic guidance system (Medtronic, Dublin, Ireland) is an FDA approved system for use in spinal surgery. It utilizes a six degree of freedom robotic arm and has an overall accuracy of 1.5 mm.⁶⁸ When using the Mazor X Stealth system, a standard workflow begins with planning screw insertion in the navigation software using a preoperative computed tomography (CT) scan. After having general anesthesia administered, an O-Arm scan is taken that captures the patient's current position and the location of the robotic arm with the attached registration device. This scan is compared with the preoperative scan to align the patient's current location in space to the preoperative plan. The procedure can either be percutaneous or open, but the next step involves the surgeon implanting the pedicle screws through the robotic arm end

effector as a guide. Upon placement of screws, another O-Arm is taken to verify accurate screw placement.

To better evaluate screw placement accuracy, the automated measurement algorithm that was developed to measure the electrode placement accuracy during DBS procedures (Chapter 2) was modified for its use with pedicle screws (Chapter 3). The algorithm was developed in MATLAB and measures pedicle screw accuracy in all three anatomical planes (Figure 1.11). This is done using six metrics: medial-lateral and superior-inferior deviation within the pedicle region, perpendicular deviation and angular deviation in the axial plane, and perpendicular deviation and angular deviation in the sagittal plane. These metrics are all measured as the values between the planned screw location from the preoperative plan to the implanted screw location. This measurement system is an objective measure that directly relates the screw to where it should have been placed in vivo compared to traditional grading scales that only analyze deviation outside the pedicle region. Using an automated system like this can better inform changes to spinal fusion surgical protocols and robotic technologies that can lead to improved patient outcomes for the treatment of degenerative musculoskeletal conditions.

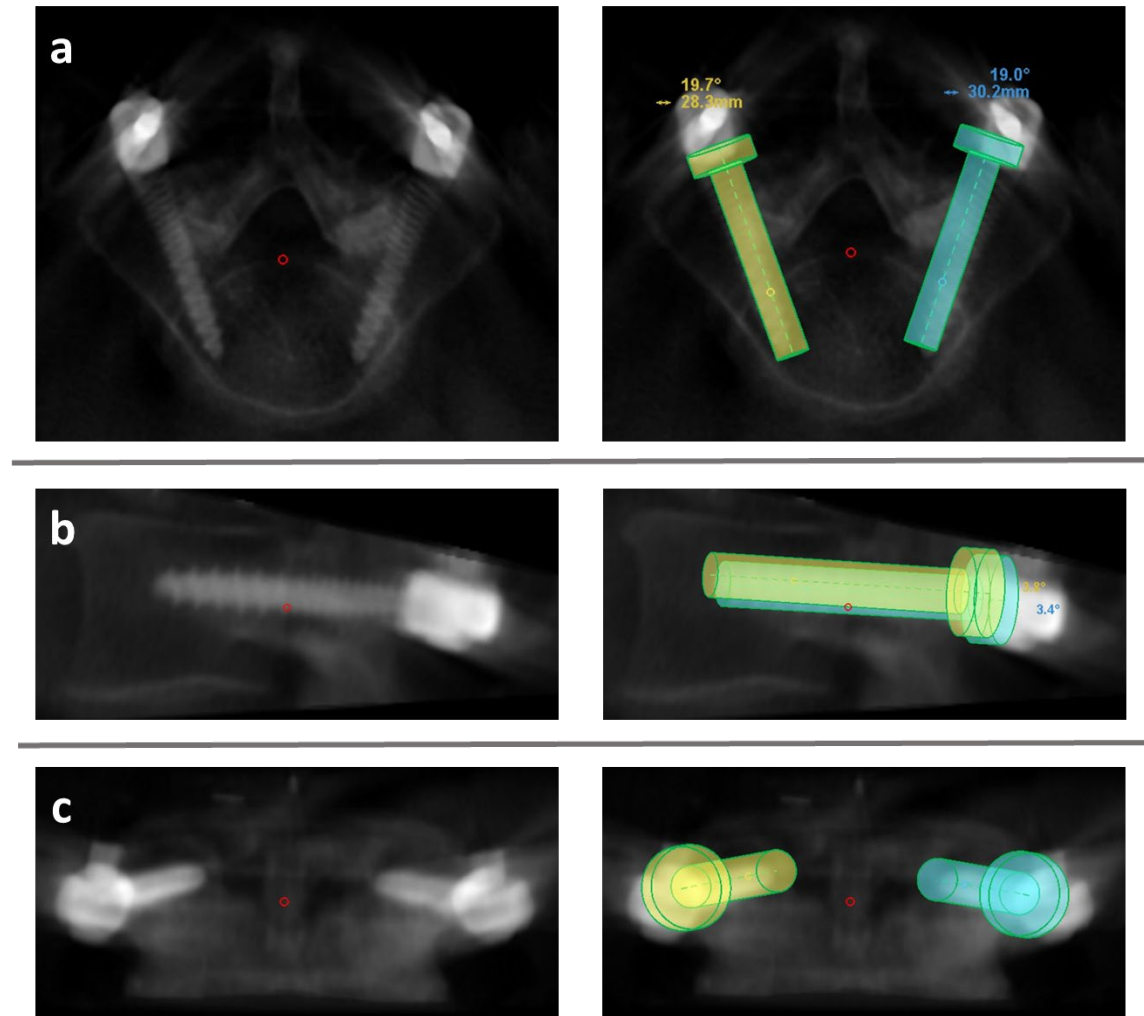


Figure 1.11 O-Arm scan showing implanted pedicle screws (left). Left (yellow) and right (blue) screw preoperative plans overlain on O-Arm scan (right). Shown in all three anatomical views: axial (a), sagittal (b), and coronal (c). Accuracy is measured between the implanted screw and the target location for each implant.

1.3 Summary of Scientific Contributions

This compilation of work includes the following scientific contributions: (1) An automated measurement algorithm for measuring the accuracy of surgically implanted devices during procedures used to treat neurodegenerative and degenerative musculoskeletal conditions. The uncertainty associated with image fusion during said procedures was quantified to better inform improvements in surgical procedures and robotic technological advances. (2) Integrated neuromusculoskeletal modeling framework

built by incorporating NEURON simulations within a FE environment. This simulation framework allows for complexity in both neural and musculoskeletal components, which is needed to study motion generation in the body and underlying disease mechanisms in neurodegenerative and neurodevelopmental diseases. (3) A fully predictive NMS mouse hindlimb model developed in the integrated FE framework. This model will be applied to study the effect changes in neural morphology will have on resulting joint movement due to neurodevelopmental and neurodegenerative diseases, and how movement changes may be used as a marker for early diagnosis.

CHAPTER TWO: ELECTRODE PLACEMENT ACCURACY IN ROBOT-ASSISTED
ASLEEP DEEP BRAIN STIMULATION*

This chapter is published by Springer Nature in the *Annals of Biomedical Engineering* and should be referenced appropriately.

Status:

This manuscript was accepted for publication in February 2019.

Reference:

D. VanSickle, V. Volk, P. Freeman, J. Henry, M. Baldwin, C.K. Fitzpatrick, “Electrode Placement Accuracy in Robot-Assisted Asleep Deep Brain Stimulation.” *Ann. Biomed. Eng.*, **47**, 1212-1222 (2019).

Reproduced/modified by permission of Springer Nature.

*This chapter includes modifications from the originally published version.

ELECTRODE PLACEMENT ACCURACY IN ROBOT-ASSISTED ASLEEP DEEP
BRAIN STIMULATION

David VanSickle^{1,3}

Victoria Volk^{2,3}

Patricia Freeman¹

Jamie Henry¹

Meghan Baldwin¹

Clare K. Fitzpatrick³

Accepted for publication in:

Annals of Biomedical Engineering

February 2019

¹*Littleton Adventist Hospital, Centura Health, Littleton, CO, USA*

²*Micron School of Materials Science and Engineering, Boise State University, Boise, ID,
USA*

³*Mechanical and Biomedical Engineering, Boise State University, Boise, ID, USA*

Abstract

Deep brain stimulation (DBS) involves the implantation of electrodes into specific central brain structures for the treatment of Parkinson's disease. Image guidance and robot-assisted techniques have been developed to assist in the accuracy of electrode placement. Traditional DBS is performed with the patient awake and utilizes microelectrode recording for feedback, which yields lengthy operating room times. Asleep DBS procedures use imaging techniques to verify electrode placement. The objective of this study is to demonstrate the validity of an asleep robot-assisted DBS procedure that utilizes intraoperative imaging techniques for precise electrode placement in a large, inclusive cohort. Preoperative magnetic resonance imaging (MRI) was used to plan the surgical procedure for the 128 patients that underwent asleep DBS. During the surgery, robot assistance was used during the implantation of the electrodes. To verify electrode placement, intraoperative CT scans were fused with the preoperative MRIs. The mean radial error of all final electrode placements is 0.85 ± 0.38 mm. MRI-CT fusion error is 0.64 ± 0.40 mm. The average operating room time for bilateral and unilateral implantations are 139.3 ± 34.7 and 115.4 ± 42.1 min, respectively. This study shows the validity of the presented asleep DBS procedure using robot assistance and intraoperative CT verification for accurate electrode placement with shorter operating room times.

2.1 Introduction

Deep brain stimulation (DBS) is a common treatment option for symptoms associated with Parkinson's Disease (PD) including essential tremor, rigidity, and dystonia.⁸⁻¹¹ DBS involves the implantation of electrodes into specific central brain structures. The electrodes deliver pulsed, high frequency electrical currents that help

regulate pathological local synchronous firing patterns of local stimulatory activity. The primary target structures in the treatment of PD are the subthalamic nucleus (STN), globus pallidus interna (GPi), and ventralis intermedius (Vim). While the STN treats most symptoms of PD, the GPi and Vim are targeted to reduce the effects of dystonia and essential tremor, respectively.¹²

A DBS procedure begins with preoperative planning to determine the target location within the brain and trajectory required to reach that location. Magnetic resonance images (MRI) of the patient are acquired and used to identify the target location. Traditional DBS procedures can be referred to as awake DBS because they involve the patient being under local anesthesia, aware of what is happening in the operating room. DBS was performed awake so that feedback could be obtained in the operating room on the effects of the implanted electrodes from the patients themselves, from microelectrode recordings (MER), or sometimes a combination of both. MER involves incrementally inserting electrodes smaller than the permanent one along the planned trajectory to measure the electrical signals coming from neurons. The electrode is advanced until reaching the target structure, and based upon both individual and local area neuronal firings, the sensorimotor regions along the trajectory can be mapped, which are used to verify that the target location is the optimal placement within the target structure. The use of MER can be associated with longer operating room times that may lead to additional surgical complications and infections,^{8, 16, 69} including an increased risk for hemorrhage.⁷⁰ The average operating room time for an awake DBS procedure ranges from 4 to 6 h.^{71, 72} There are a number of limitations associated with awake DBS. Lengthy procedures are taxing for the patient and operating room staff. The patient can undergo

fatigue, and although they can provide feedback, it cannot include full motor function assessment such as standing or walking. There is a proportionally higher economic burden associated with the surgeon, OR staff, and facilities time required for these lengthy procedures.⁷³ Typically, the longer the operating room time, the longer the recovery time, which is challenging for the patient and can create additional costs.

To address some of the concerns surrounding awake DBS, a procedure utilizing general anesthesia, known as asleep DBS has been developed.¹⁶ Asleep DBS still involves the preoperative MRI planning, but relies on high-resolution imaging, image guidance, and sometimes robotic-assistance to validate the placement of the electrode within the target location. Imaging and robotic assistance provides the accuracy and precision required to remove the dependency on physiological feedback relied on during awake DBS to determine electrode placement. MER can still be used in asleep DBS procedures to provide electrical-signal feedback, but due to the additional risk and the controversy regarding the efficacy of MER,^{8, 16, 70, 74} intra-operative imaging techniques are used instead. These techniques involve computed tomography (CT) or MR images being taken during the procedure to verify electrode placement within the anatomical target. If CT is used intraoperatively, it is fused to preoperative MRI because only the MRI can accurately show the grey matter within the brain to view the target structure. The merged MRI-CT scans can then be used to assess the placement of the electrode (captured from the CT) compared to the target location (identified on the MRI). This does introduce a source of error to the procedure, as MRI and CT both have individual errors, along with error involved when merging the two types of scans. MRI has a nonuniform magnetic field generated from the main magnet in the equipment that leads to non-

linearities in the gradients generated, which makes straight lines appear curved or distorted at the edge of MRI scans.⁷⁵ CT scans have a low soft tissue contrast which makes it hard to visualize target structures and any metal in the image can lead to streaking distortion.⁷⁶ By combining the two imaging modalities, the electrode placement can be properly planned and verified after insertion. The operating room time is drastically shorter for asleep procedures, and is reported to range from 2 to 3.17 h.^{16, 77, 78}

The primary measure of success for a DBS procedure within the operating room before clinical outcomes can be determined is electrode placement accuracy. This is measured as the radial error between the center of the target location determined preoperatively and the center of the implanted electrode. If the surgeon is concerned about the accuracy of initial placement, the electrode may be re-implanted; however, there is debate as to what constitutes sufficient accuracy. Some studies use the standard of re-implanting the electrode if it is farther than 2 to 3 mm away from the target¹⁵ while others state simply 3 mm as the standard for re-implantation.¹⁶ Asleep DBS procedures have reported placement accuracies comparable to those of awake DBS,^{16, 79} with the lowest report radial error for asleep DBS being 0.6 ± 0.3 mm.⁸⁰

To improve the precision of asleep DBS, robots, such as SurgiScope, NeuroMate, Renaissance, and ROSA, are being utilized within the operating room.⁸¹ The safety and effectiveness of using a robot for stereotactic neurosurgery has been shown previously.⁸¹⁻
⁸⁶ A study of a frame-based DBS procedure using the NeuroMate robot for the implantation of 30 leads reported a Euclidean error of 0.86 ± 0.32 mm measured using orthogonal radiographs in Stereoplan.⁸⁷ Neudorfer and colleagues found that there were statistically significant improvements for a cohort of 80 patients (40 implanted using each

method) in lateral deviation and operating room time when performing robot-assisted DBS compared to conventional frame-based implantation methods.⁸⁸ The addition of robot-assistance within a DBS asleep procedure has been shown to have the same clinical improvement as awake surgeries when Unified Parkinson's Disease Rating Scale (UPDRS) motor scores were compared.⁶⁹ The Mazor Renaissance robot is used in this study, which is an FDA approved system for electrode/implant placement and brain biopsies. It is a small, frameless platform with 360° working volume for highly accurate access to planned trajectories.

The objective of this study is to demonstrate the validity of an asleep robot-assisted DBS procedure that utilizes intraoperative imaging techniques for precise electrode placement in a large, inclusive cohort. Electrode placement accuracy, fusion error associated with intraoperative CT to preoperative MRI, operating room times, and adverse effects are quantified for a cohort of 128 patients with 241 lead placements.

2.2 Materials and Methods

2.2.1 Patient Inclusion and Demographics

A total of 128 consecutive patients were included in this study, of which 113 underwent bilateral implantation and 15 unilateral implantation (total 241 lead placements). The target location was the STN in 162 cases, Vim in 42 cases, and GPi in 37 cases. Of the 128 patients, 68 were female, 48 were male, and 12 did not have information recorded. The mean age of the patients was 64.6 ± 13.2 years. All surgeries were performed by the same surgeon (DVS) at Littleton Adventist Hospital in Littleton, CO between August 2014 and October 2017. This study was approved by the Porter Adventist Hospital Institutional Review Board.

2.2.2 Surgical Procedure

All patients received a preoperative T1 MRI with gadolinium and a T2 MRI using a GE LX, 60-cm bore, 1.5 Tesla MRI under general anesthesia (Figure 2.1a) (1 mm slice, matrix 512 9 512, 0.487 9 0.487 mm in-plane resolution). The MRI was calibrated using the American College of Radiology standard phantom tests.⁸⁹ For the first twelve patients, the MRI and the electrode placement procedure were performed on the same day and under the same anesthetic; however, following a practice change, the MRI and trajectory planning were performed under general anesthesia the day prior to surgery for the remaining patients. On the day of surgery, the patient is positioned using a head clamp (Doro 4002-20, Pro Med Instruments, Freiburg, Germany) customized for use with intraoperative CT, which would not be necessary for an awake DBS procedure. The surgical plan is verified and measurements are taken for the placement of the Renaissance robot (Mazor Robotics, Caesarea, Israel) attachment base. High precision of the robot base is not required as long as the robot is attached on the skull in a location where the robot can reach the target trajectories. The robotic software calculates a series of possible mounting locations. Calipers are used to triangulate from known anatomic landmarks or fiducial markers to the selected base location. A sterile field is then created and a fiducial frame, known as the Star Marker, is attached to the base that allows the planning software to orient the Renaissance system to the patient and intraoperative CT scan (Figure 2.2a). The intraoperative CT (2 s. rotation, 120kV, 7 mA, 1.25 mm slice thickness, 0.494 9 0.494 mm in-plane resolution; CereTom™, Neurologica Corp., Danvers, MA.) is obtained in a sterile fashion (Figure 2.1b) and then fused with the preoperative MRI (Figure 2.1). When the CT is fused to the MRI, the robot base location is known relative

to the target trajectories. This intraoperative CT is referred to in this study as the fiducial CT. The MRI-CT fusion process is completed in the Mazor Renaissance software. It involves an initial manual alignment performed by the surgeon, followed by the software registration algorithm completing the six-degree-of-freedom fusion. Once completed, the fusion is visually inspected by the surgeon for success.

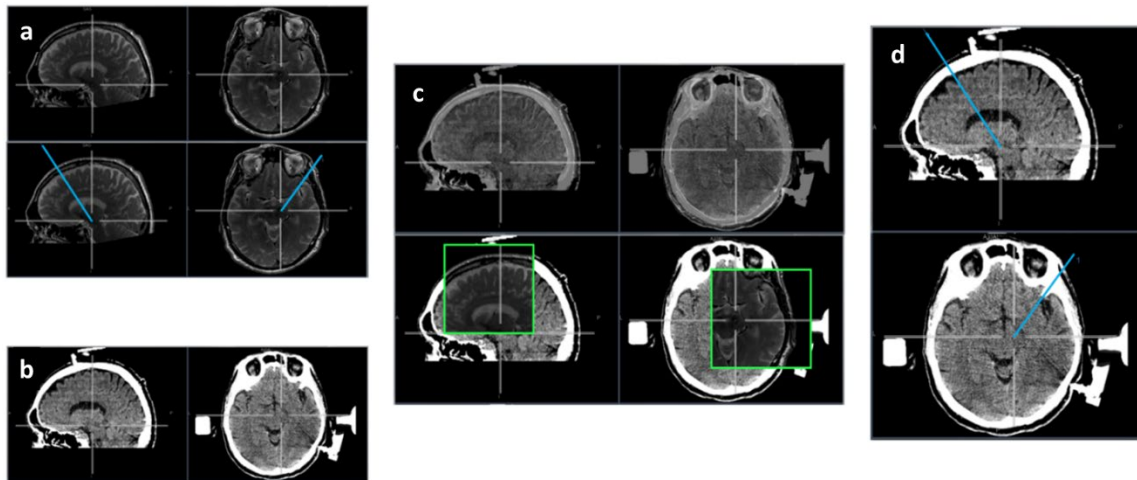


Figure 2.1 (a) Preoperative T2 MRI acquired with a 1.5 Tesla machine under general anesthesia (top), with preoperative cannula trajectory plan for the right STN shown in blue (bottom). (b) Intraoperative CT (including fiducial frame for orientation of the renaissance system). (c) Fusion of MR and CT scans; transparent overlay of T2 MRI and intraoperative CT (top), intraoperative CT with T2 MRI shown within window (bottom). (d) Intraoperative CT with preoperative plan mapped from the fused MRI shown in blue. Sagittal and axial images that pass through the right STN are shown in each instance.

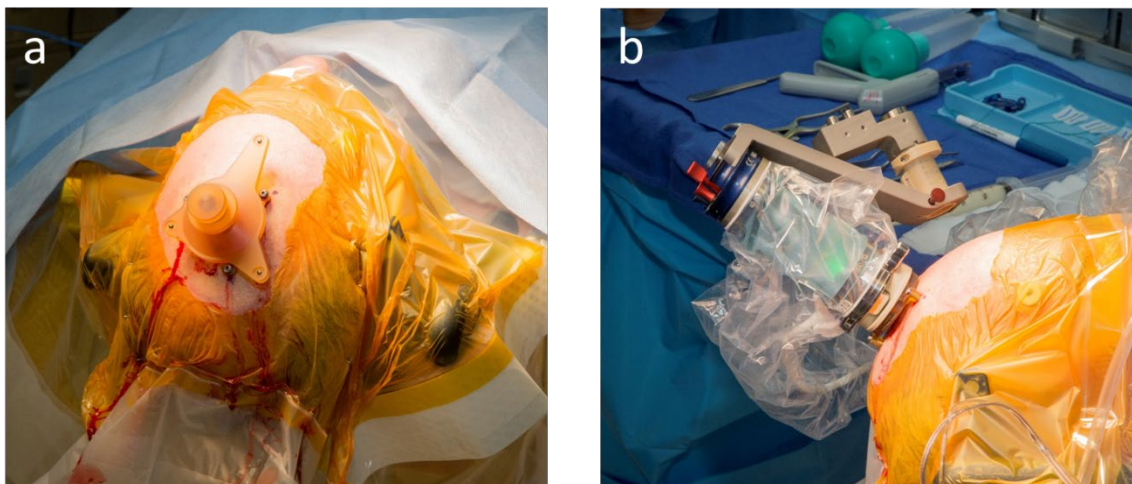


Figure 2.2 (a) Fiducial frame attached to the robotic base that allows the software to orient the Renaissance system. (b) Robot positioned on the base with arm attached. The arm is oriented over the target insertion point so that the precise location can be marked on the scalp.

The robotic arm is attached to the base and the arm of the robot commanded to move to the target insertion point (Figure 2.2b), where the location is marked and the robot is removed in order to create a sterile incision. After the incision is made, the robot is reattached to locate the site of the planned burr-hole. The robot is removed once again for the actual burring procedure and attached a third time for placement of the to-target cannula. The dura is not opened at this stage of the procedure. An FHC (Bowdoin, ME) ST-DS-MA drive system is attached to the robotic arm for to-target cannula depth measurement. The dura is perforated using monopolar electrocautery. The size of the penetration matches the size of the cannula to prevent cerebral spinal fluid loss and subsequent brain shift. A secondary intraoperative CT is performed with the robot attached and cannula in place; this intraoperative CT is referred to in this study as the verification CT (Figure 2.3). In order to verify accurate placement of the cannula, the verification CT is fused with the fiducial CT and the deviation between cannula placement and the preoperative trajectory plan is assessed. Acceptance of the cannula

position is based upon the accuracy of the placement, a radial error of less than 2 mm, and a verification that the 1.8 mm diameter cannula is wholly within the target structure, so unwanted stimulation to surrounding structures does not occur, both of which are at the surgeon's discretion. Any adjustment is made by use of an X–Y stage (Alpha Omega, Nazareth, Israel). For any surgery that requires adjustment of the cannula position, an additional verification CT is performed with the cannula in its final position. If an adjustment needed to be made only to the depth of the cannula for the final electrode placement, it was adjusted accordingly and no additional verification CT was taken. For bilateral surgeries, this process is repeated (Figure 2.4).

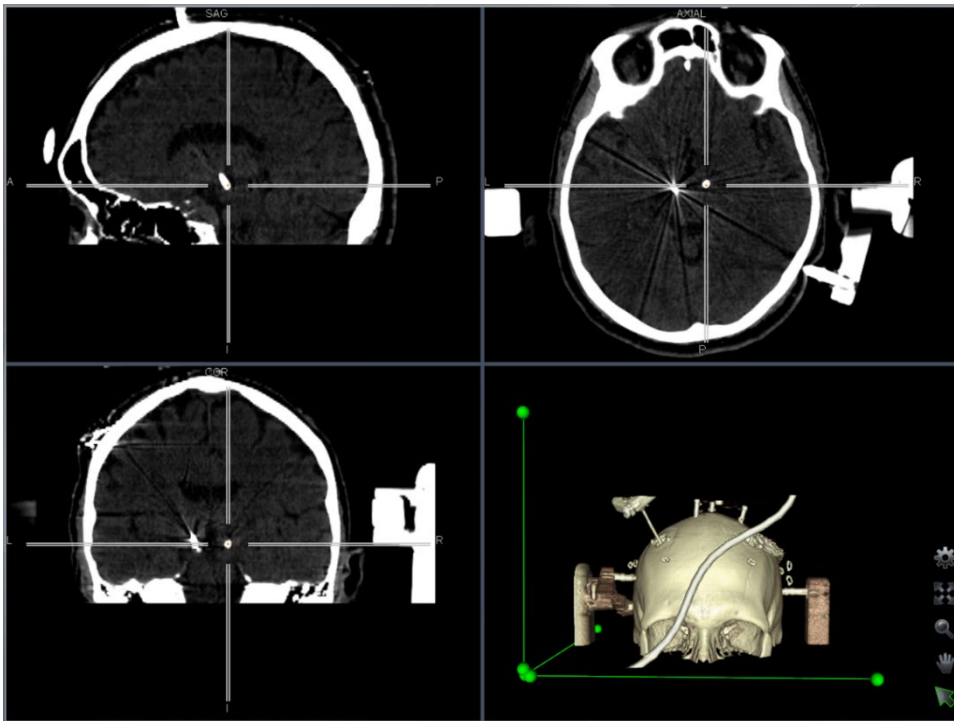


Figure 2.3 A secondary intraoperative CT is obtained after placement of the cannula; the right cannula is shown here in sagittal (top, left), axial (top, right), and coronal (bottom, left) views.

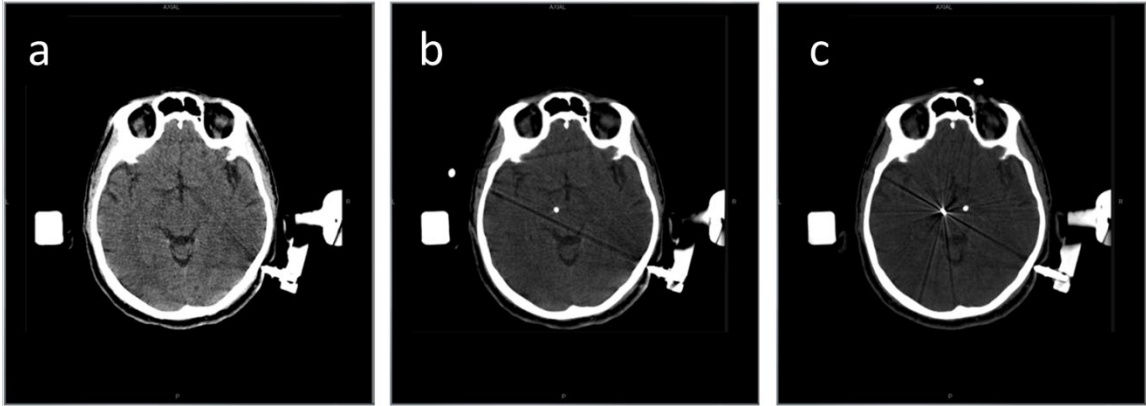


Figure 2.4 Series of intraoperative CT scans performed during bilateral surgery. (a) Fiducial CT for registration of the Renaissance robotic system with the preoperative MRI. (b) Verification CT after placement of the left cannula. (c) Verification CT after placement of the right cannula.

2.2.3 Electrode Accuracy

Deviation from the intended target is measured when looking down the view of the planned trajectory on the verification CT for a given side (Figure 2.5). The electrode placement accuracy is the radial distance between the center of the implanted electrode and the center of the target location (Figure 2.6). Errors in depth of the cannula after implantation were also calculated and reported, however, this study focuses primarily on radial errors as errors related to the depth of the cannula measured by the verification CT were subsequently corrected by using the micro-drive system to adjust the depth placement to eliminate this depth error. Unless otherwise stated, the errors reported in this study refer to radial errors. An algorithm was developed in MATLAB 2017b (The Mathworks, Inc., Natick, MA) to automate the electrode placement accuracy measurement process. It utilizes image processing tools to locate the center of the electrode and target. It then quantifies and converts the accuracy to standard units of mm. The development of the automated measurement process eliminates human variance in measurement and bias. A comparison of 27 patients with 53 electrodes implanted

measured both manually and using the algorithm shows a statistically significant difference ($p = 0.008$) between the final placement accuracies of 0.79 ± 0.36 and 0.85 ± 0.35 mm for the manual and automatic measurement systems, respectively. The automated process also saves computational time, which is beneficial when analyzing large cohorts.

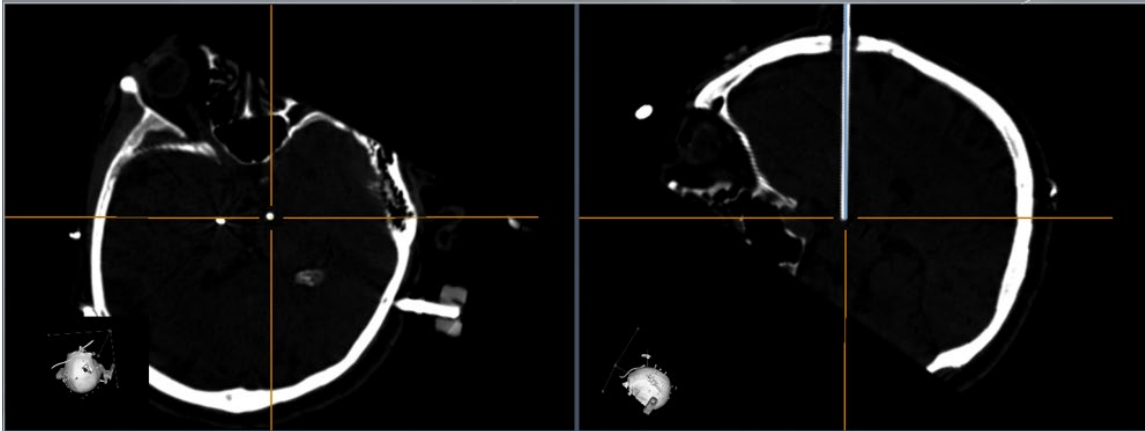


Figure 2.5 Verification CT viewed along the length of (left) and perpendicular to (right) the planned trajectory of the right cannula. Placement accuracy measurements are made from the view along the length of the planned trajectory.

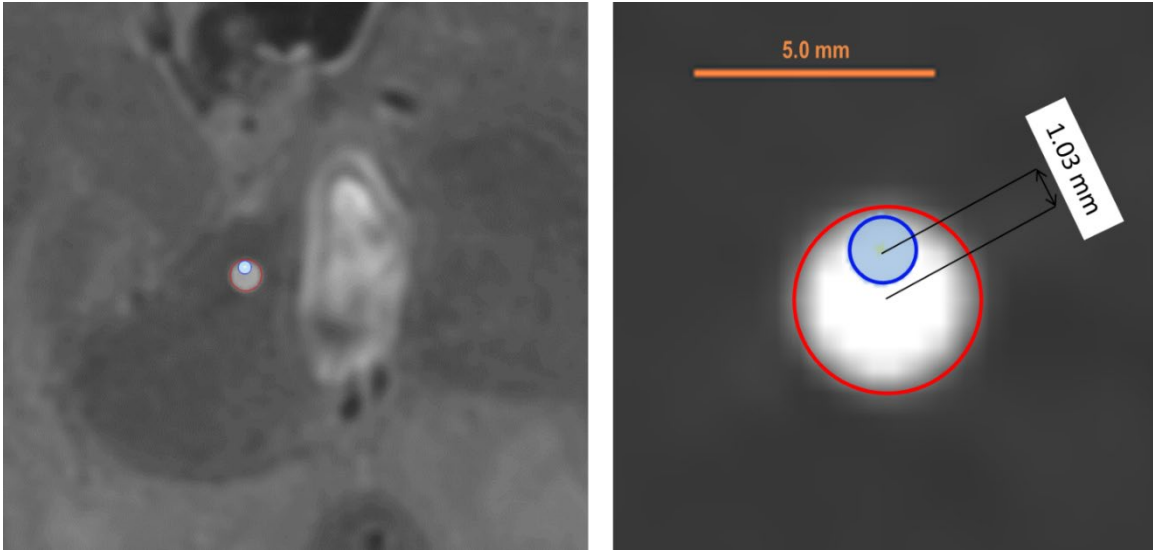


Figure 2.6 Overlay of the preoperative MRI with target trajectory (blue) and verification CT cannula placement (red). Close-up with 5.0 mm reference scale bar shown on the right – this image was used to measure the difference between center of the target site and the center of the implanted cannula. Images are shown looking along the target cannula trajectory.

A source of potential error that adds uncertainty to the accuracy of the electrode placement is the MRI-CT fusion process. To our knowledge, the error involved in fusing the two scans has not previously been quantified. In the operating room, the verification CT scans are fused with the original fiducial CT; the fiducial CT is the only CT which is fused directly with the preoperative MRI. In order to quantify the error associated with the MRI-CT fusion process, in post-operative analysis each verification CT was independently fused with the preoperative T1 MRI. The target location from the MRI was mapped to each CT scan (fiducial plus verification CTs). When the CT scans are compared, the target location appear in slightly different locations in each scan. While it is not possible to determine the exact location of the target with respect to the CT images, the difference between the electrode centers in each CT is the deviation that results from fusing the CT and MRI scans (Figure 2.7). The deviation analysis includes all first,

second, and third passes for unilateral and bilateral implantations since fusion order does not play a role in calculating the fusion error.

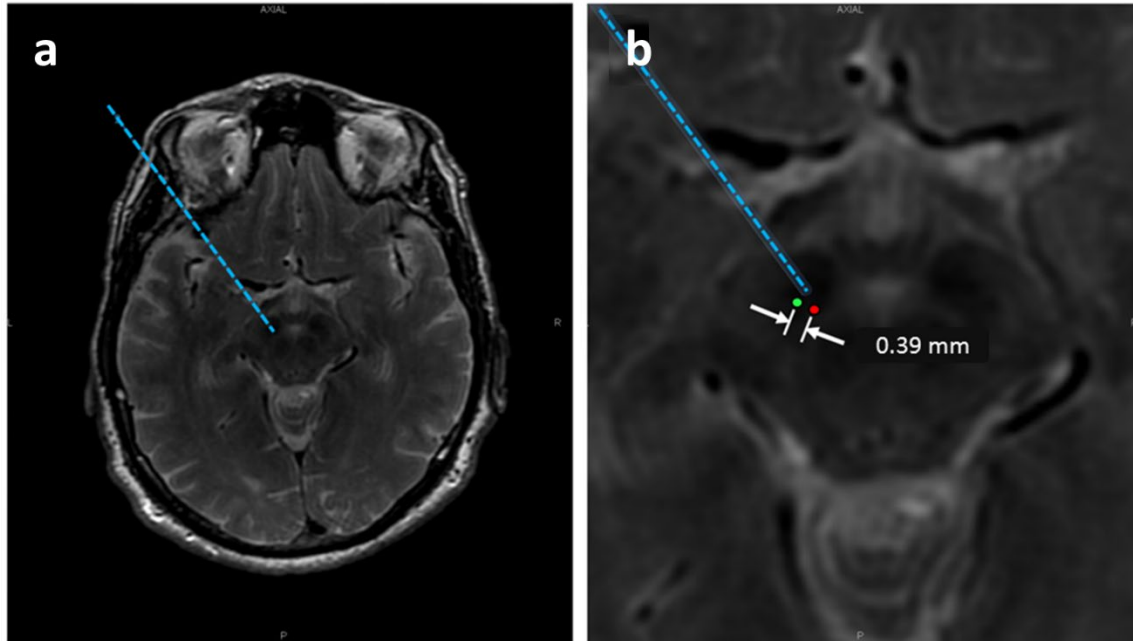


Figure 2.7 (a) Measurement of MRI-CT fusion error. Preoperative MRI with target cannula trajectory (blue dashed line). (b) Close-up showing apparent location of the center of the cannula from verification CT fused with fiducial CT (red) and apparent location of the center of the cannula from verification CT fused directly with MRI (green). Fusion error is defined as the distance between these locations.

Statistical comparisons between the first and second side implanted and initial and final placement accuracies were quantified using a student's paired t test. The effect of target location (STN, GPi, Vim) was evaluated using a one-way ANOVA. A p-value below 0.05 was considered statistically significant.

2.3 Results

A total of 241 electrodes were implanted, of which 226 were for bilateral implantations, 7 for unilateral right, and 8 for unilateral left. The placement accuracy for all initial passes of the 241 implants is 1.06 ± 0.60 mm. The mean initial pass placement

accuracies of the first and second sides implanted are 0.91 ± 0.46 and 1.20 ± 0.65 mm, respectively. There is a significant difference ($p < 0.001$) between the initial pass placement accuracy of side one and side two. Of the 241 electrodes implanted, 51 were re-implanted a second time (21%) and 3 were re-implanted a third time (1%). Re-implantation was determined based on a variety of factors including a radial error greater than 2 mm, the electrode not being positioned optimally in the target structure either because the cannula is not wholly within the structure or there is a better location possible that could only be observed once the electrode was implanted, or a combination of the aforementioned reasons. A total of 14 electrodes (6%) were re-implanted a second time based upon a radial error greater than 2 mm.

The placement accuracy for all final placements for the 241 implants is 0.85 ± 0.38 mm. There is a statistical significance ($p < 0.001$) between the total initial and final placement accuracy values. The final placement accuracy for the first and second implanted sides are 0.82 ± 0.36 and 0.87 ± 0.38 mm, respectively, which have no statistical difference. The initial and final placement accuracies based on target location are shown in Table 2.1. There is no statistical difference between the placement accuracies of the three locations. There is a statistical difference between the initial and final placement accuracies in each location independently: STN ($p < 0.001$), VIM ($p = 0.027$), and GPi ($p = 0.020$).

Table 2.1 Electrode Placement Accuracy Values (mean \pm SD).

	STN	Vim	GPi	Total
Number of Implants	162	42	37	241
First Pass Accuracy [mm]	1.08 \pm 0.62	0.92 \pm 0.44	1.15 \pm 0.63	1.06 \pm 0.60
Final Pass Accuracy [mm]	0.84 \pm 0.38	0.81 \pm 0.36	0.88 \pm 0.38	0.85 \pm 0.38

When the errors in cannula depth along the planned trajectory were calculated, the initial and final placement absolute depth errors were 0.57 ± 0.62 and 0.64 ± 0.62 mm, respectively. In the initial placement, 41% of implants were located at the target depth, 38% were located shallower than the target by 0.98 ± 0.50 mm, and 21% were located deeper than the target by 0.92 ± 0.54 mm. Similar results in depth error were measured from the verification CT after final placement; 34% of implants were located at the target depth, 39% were located shallower than the target by 0.99 ± 0.48 mm, and 27% were located deeper than the target by 0.95 ± 0.54 mm. However, the micro-drive system was subsequently used to adjust the depth placement to eliminate this depth error.

By using all of the implanted electrode fusions, including re-implants, the MRI-CT fusion error was calculated for 292 fusions. The mean deviation is 0.64 ± 0.40 mm. There was no statistical difference in fusion deviation between first and second side implants.

The operating room time, defined as skin-to-skin contact time, for 97 bilateral implantation procedures is 139.3 ± 34.7 min. For 11 unilateral implantations, the

operating room time is 115.4 ± 42.1 min. Operating time was not available for the remaining 20 procedures.

Adverse events that were complications of robotic surgery occurred in four (3.1%) patients. One patient had a lead repositioning due to movement in contact position while another had an erosion of a DBS lead extension on a single side. In the operating room, one patient experienced an intraparenchymal hemorrhage that led to symptoms of a stroke which resolved, and a deep vein thrombosis in the left arm. Two weeks postoperatively, one patient had a pulmonary embolism. In all cases, a diagnostic post-operative CT was performed. No significant intraparenchymal hemorrhage was present. Complications unrelated to the robotic surgery occurred in two patients who had a DBS pulse generator repositioned within the pocket due to migration, which was causing discomfort. There were no battery infections outside the 2 week period.

2.4 Discussion

The application of intraoperative imaging techniques to DBS have been revolutionary in modifying the procedure to where it is today with near real-time electrode placement verification within the operating room. For a traditional awake procedure, the reported average placement accuracy of McClelland and colleagues for a cohort of 26 patients (52 leads) is 1.4 mm in the lateral/medial direction and 1.2 mm in the anterior/posterior direction.¹⁵ A recent study utilized the Renaissance Mazor robot and MER for electrode implantation in 20 patients (40 leads), which included both awake and asleep DBS procedures, and measured a radial error of 1.40 ± 0.11 mm.⁸⁶ The final electrode placement accuracy of the current study is comparable to other reports of asleep DBS procedures; radial errors reported in the literature include 1.24 ± 0.87 mm on a

cohort of 60 patients (119 leads),¹⁶ 0.9 ± 0.5 mm on 48 patients (94 leads) using the NexFrame and intraoperative CT verification,⁷⁹ and 0.6 ± 0.3 mm on twenty patients (40 leads).⁸⁰ In the procedure described by Ostrem et al.,⁸⁰ the surgery is performed entirely within a MRI suite which can be costly and not feasible at all hospitals. The presented surgical procedure has the advantage of using the CereTom portable CT scanner which is available in a standard operating room with lower costs.⁷³

The accuracy of the system being reported is a culmination of numerous factors including the to-target cannula that prevents deviation of the electrode, immobilization of the head during surgery, and the robot being affixed to the skull. It should be also noted that there are numerous other factors that may contribute to the accuracy of electrode placement, apart from the use of a robot-assisted technique. These factors include, amongst others, the experience of the surgeon and surgical team, learning curve associated with the surgical procedure, or different surgical priorities in awake as compared to asleep DBS procedures. The patient being under general anesthesia for the preoperative MRI is also critical to the placement accuracy as even a 1–2 mm shift during image acquisition would become the dominant source of error for the procedure.

The automated measurement algorithm eliminates human bias when determining the electrode primary contact center that may subsequently affect radial error values. Previous studies have measured placement error on the Stealth Station^{15, 16} or using FrameLink software.^{79, 80} One study using the Stealth Station analyzed the interobserver reliability of determining the coordinates of the principal contact on post-operative MRI images and found that there were statistically significant differences in three of eight measured coordinates.¹⁵ Alternatively, Mirzadeh et al. found no significant difference in

measurements following independent principal contact coordinate selections from two surgeons on post-operative MRIs.⁷⁹ Although both of these studies analyzed manual coordinate determination on MRIs, CT images also have artifact around the implanted cannula that can make determining the precise center of the cannula difficult. The automated measurement process accounts for the electrode not being perfectly circle and removes human variability that may impact the determination of the circle center for more precise radial error measurements.

The significant difference between the initial placement accuracies of the first and second sides implanted could be caused by CT artifact distortion from the electrode previously implanted on the verification CT check for the second side. This indicates the need to further understand and quantify CT artifact caused by the electrodes.

Previous studies have looked at MRI-CT fusion as it applies to DBS surgery. Mirzadeh et al. fused intraoperative CT with preoperative MRI and target location from the MRI was mapped to the CT.⁷⁹ Then, postoperative MRI was used to independently identify the target location. The error differences between the target location identified on intraoperative CT and postoperative MRI were quantified, thereby calculating a combination of plan-to-CT fusion error plus MRI measurement variance. Geevarghese et al. measured stereotactic fusion error in a different way.⁹⁰ They identified the stereotactic coordinate system through fiducial markers on the MRI, and then fused the intraoperative CT with the MRI. Using an unfused version of the same CT scan, they identified the stereotactic coordinate system through fiducial markers on the CT. The error measured in their study is the difference in location of the electrode tip between these two coordinate systems. In the study presented here, two, or more in the case of reimplantation, CT scans

were independently fused with preoperative MRI and the target location superimposed on each CT. CT scans were subsequently merged and difference in target location of the target between CT scans was used to quantify a MRI-CT error.

The key aspect of asleep DBS is the use of intraoperative imaging to verify electrode placement location without MER or patient feedback. This can be accomplished using either intraoperative MRI or CT, but regardless of which is used, the fusing of two images together has inherent error. This error is an additional source of variability to the placement accuracy values stated above. The precise location is unknown due to the MRI-CT fusion error, but the deviation analysis allows quantification of this uncertainty across the patient population. This uncertainty metric can be utilized in the operating room to help surgeons determine how close the electrode must be to the target location to be confident that it is actually within the boundary of the target structure (Figure 2.8).

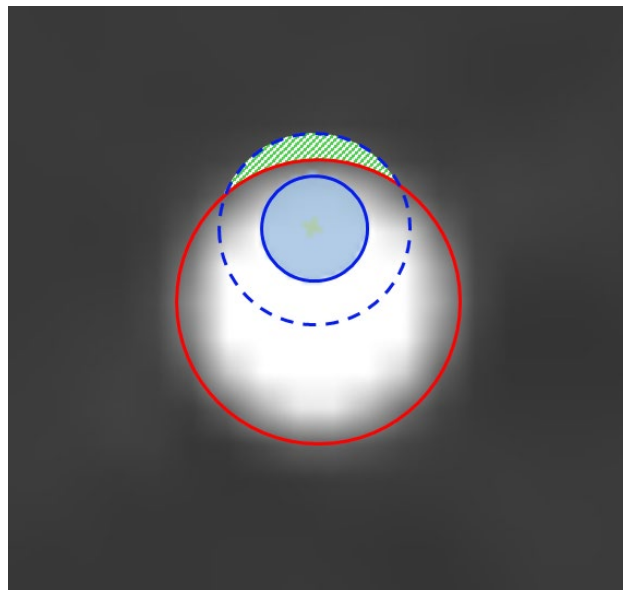


Figure 2.8 Implication of MRI-CT fusion error. To ensure accurate placement, the target (blue) must be wholly within the cannula region (red). When the average MRI-CT fusion deviation (blue dashed) is accounted for, the probability that the placement is not fully with the target region can be calculated (green striped region).

The mean operating room time of this study (2.3 h) is on the lower side of the range of previous asleep DBS studies, which is significantly lower than that of awake DBS procedures. The shorter surgery time is more comfortable for the patient, surgeon, and operating room staff. There is no significant change in OR time from the first cases to the last, which seems to indicate a shorter learning curve for this technique. The low rate of infection of 3.1% compares favorably to 5.6% reported in prior studies,⁹¹ and adverse effects postoperatively can in part be attributed to the shorter amount of time spent within the operating room. With the shorter operating room time, a surgeon can more easily fit multiple surgeries in a day. While the necessity of robotic-assistance in asleep DBS requires capital investment in equipment and maintenance costs that add to the overall economic impact of the procedure, these costs are offset by the reduced OR time per surgery—reduced OR time may facilitate increased volume of procedures which reduced the “per surgery” capital costs, which are typically in the range of \$60–\$100 per minute of OR time. Additionally, a corresponding reduction in infection and adverse effects rates may reduce the hospital stay length for these patients further reducing the overall cost of the procedure.

An advantage to using the Mazor robotic system over other commercially available options is the autoregistration that the system utilizes. Most other frameless systems require the manual registration of fiducial markers, whereby a probe attached to the robot or followed by a 3D camera system is sequentially placed by hand into bone mounted fiducials. The Mazor system embeds the fiducials directly into the Star Marker at fixed positions relative to the robotic attachment base, making the manual registration step unnecessary. This saves OR time and leads to more accuracy in electrode placement.

Although the placement accuracy with this procedure using the Renaissance robot with intraoperative CT verification is comparable to that of awake procedures and other asleep procedures, the relationship between placement accuracy and patient functional outcomes is beyond the scope of the current study. Error in placement accuracy may be compensated for during calibration of electrode voltage and the introduction of directional electrodes; however, optimizing placement accuracy may facilitate minimizing voltage magnitude and localizing the effects of electrical stimulation. An analysis must be performed to evaluate the effect placement accuracy has on the clinical outcomes of the patient, such as UPDRS scores and mobility tests. Additionally, future work should involve determining if there is a correlation between placement accuracy and the stimulation parameters set up postoperatively for the patient.

This study analyzing a cohort of such a large magnitude shows the validity of this asleep DBS procedure that uses the Renaissance robot for precise electrode implantation with the convenience of intraoperative verification CTs using the portable CereTom CT scanner. The workflow of this procedure allows a shorter operating room time that benefits the patient while obtaining the necessary electrode accuracy within the target structure, which can be pinpointed more accurately within the operating room using the now quantified MRI-CT fusion error. Future work will provide the link between electrode placement and clinical efficacy.

2.5 Author Justification

D.V.: study concept, lead surgeon for implantation of electrodes, design of the study, interpretation of results, prepared figures. V.V.: developed automated measurement algorithm, performed all analyses, prepared figures, primary writer. P.F.:

assisted in surgical implantation of electrodes. J.H.: assisted in surgical implantation of electrodes. M.B.: assisted in surgical implantation of electrodes. C.K.F.: design of the study, interpretation of results. All authors contributed to editing and revision of the manuscript for intellectual content.

CHAPTER THREE: PEDICLE SCREW PLACEMENT ACCURACY IN ROBOT-
ASSISTED SPINAL FUSION IN A MULTICENTER STUDY*

This chapter was submitted to the *Journal of Neurosurgery: Spine*.

Status:

This manuscript was submitted for publication in April 2022.

Reference:

V.L. Volk, K.A. Steele, M. Cinello-Smith, R.V. Chua, J. Pollina, G. Poulter, E. Shafa, P. Busselberg, C.K. Fitzpatrick, “Pedicule Screw Placement Accuracy in Robot-Assisted Spinal Fusion in a Multicenter Study.” *J. Neurosurg. Spine*. under review (April 2022).

*This chapter includes modifications from the originally submitted version.

PEDICLE SCREW PLACEMENT ACCURACY IN ROBOT-ASSISTED SPINAL
FUSION IN A MULTICENTER STUDY

Victoria L. Volk^{1,2}

Keegan A. Steele²

Mia Cinello-Smith²

Richard V. Chua³

John Pollina⁴

Gregory Poulter⁵

Eiman Shafa⁶

Peter Busselberg⁷

Clare K. Fitzpatrick²

Submitted for publication in:

Journal of Neurosurgery: Spine

April 2022

¹*Micron School of Materials Science and Engineering, Boise State University, Boise, ID,
USA*

²*Mechanical and Biomedical Engineering, Boise State University, Boise, ID, USA*

³*Northwest NeuroSpecialists, Tucson, AZ, USA*

⁴*Department of Neurosurgery, University of Buffalo, Buffalo, NY, USA*

⁵*OrthoIndy Hospital, Indianapolis, IN, USA*

⁶*Twin Cities Spine Center, Minneapolis, MN, USA*

⁷*RAYUS Radiology, St. Louis Park, MN, USA*

Abstract

Objective: Pedicle screw fixation is a spinal fusion technique that involves the implantation of screws into vertebral pedicles to restrict movement between those vertebrae. Robotic guidance systems have been designed to assist in the implantation of pedicle screws. The accuracy of robotic-assisted implantations has been compared to conventional methods using traditional grading scales. The objective of this research is to measure pedicle screw placement accuracy using a novel automated measurement system that directly compares the implanted screw location to the planned target location in all three anatomical views in robotic guided procedures.

Methods: Preoperative CT scans were used to plan the screw trajectories in 122 patients across four surgical centers. Postoperative scans were fused to the preoperative plan to quantify placement accuracy using an automated measurement algorithm.

Results: The placement accuracy of 500 screws was measured. The mean medial-lateral and superior-inferior deviations in the pedicle region are 1.75 ± 1.36 mm and 1.52 ± 1.26 mm, respectively. In the axial plane, the mean perpendicular deviation is 2.00 ± 1.54 mm and the angular deviation is $2.40^\circ \pm 2.07^\circ$. In the sagittal plane, the mean perpendicular deviation is 2.16 ± 1.74 mm and the angular deviation is $4.21^\circ \pm 8.31^\circ$. Using a traditional grading scale, 97.2% of the screw placements were classified with a grade of A or B, indicating less than 2 mm of deviation outside of the pedicle.

Conclusions: This study uses a novel measurement system to quantify screw placement accuracy to show the validity of using of a robotic guidance system for accurate pedicle screw placement. This system measures screw placement accuracy as it

relates directly to the planned target location instead of analyzing the placement for breaches of the pedicle.

3.1 Introduction

Pedicle screw fixation is a spinal fusion technique that involves the implantation of screws into vertebral pedicles to act as anchor points for rods to restrict movement between those vertebrae.^{49, 50} Fusions are a common treatment for a variety of spinal conditions including lumbar stenosis, spondylolisthesis, degenerative disc disease, and disc herniation.⁴⁶⁻⁴⁸ Although fusion can occur at any spinal level, the majority of cases in this study are in the lumbar region. The number of lumbar spinal fusion (LSF) cases is increasing annually, with over two million people having undergone a LSF between 2004 and 2015.⁴⁸ The prevalence of LSF was estimated to be 79.8 per 100,000 individuals.⁴⁸

The conventional method for pedicle screw insertion is the freehand method, oftentimes with intraoperative fluoroscopy guidance.⁵⁶ The primary outcome measure for pedicle screw insertion is placement accuracy. A grading scale is used to rate the implantations based on the amount of screw deviation outside of the pedicle. There are numerous grading scales, including Gertzbein and Robbins,⁵² Rampersaud,⁵⁵ and Youkilis.⁵⁴ A standard metric for acceptance of screw placement is less than 2 mm outside of the pedicle, as measured in the medial-lateral direction.^{52, 53}

In efforts to improve placement accuracy and clinical outcomes, including operating room time, radiation exposure, and longevity of hospital stay, surgical robots were created to assist in spinal fusion surgery. There are a variety of surgical robots currently on the market including Renaissance,^{57, 58} Mazor X,^{57, 58} ROSA,^{57, 59} TINAVI,⁶⁰ and ExcelsiusGPS.⁵⁶ There is a compilation of literature comparing robot-assisted screw

placement to the freehand method, with debate as to whether or not robotic assistance actually leads to increased accuracy.^{47, 60-63} A review by Ghasem et al. included 12 studies that compared robot-guided surgery to the freehand method and showed that 10 studies demonstrated an increase in placement accuracy when robot-assistance was used, compared to one study that showed no difference between the methods and another study that showed worse accuracy with robotic guidance.⁵⁷ However, it has been shown that procedures that utilize robot-assistance compared to those without have decreases in length of hospital stay^{64, 65} and radiation exposure.^{60, 65-67} These factors are beneficial to both patients undergoing the procedure and hospital staff, as well as an associated cost reduction.

Previous studies have compared robot-assisted procedures to conventional methods by analyzing screw placement accuracy using the aforementioned classifications.^{53, 92-97} The largest of these studies evaluated robotic guidance of 3,131 pedicle screws in 593 patients over a 4 year period.⁹² Although this was a large multicenter study across 14 locations, there was variability in the criteria used for clinical acceptance of placement across locations and surgeons, so implants could not be directly compared. Three studies have quantified robotic accuracy by comparing implanted screws directly to the target locations, but they only analyzed entry and exit point deviation or angular deviation in axial and sagittal views, and not the deviation in the pedicle region where clinical grading scales measure accuracy.^{92, 93, 97} To the authors knowledge, no studies at this time have used automated measurements to remove human input and bias from the measurement process. The process of fusing preoperative with intra- or postoperative images, which is a necessary step to compare implanted screws to

the planned locations, involves manual alignment which has not been previously quantified.

The objective of this research is to measure pedicle screw placement accuracy using a novel automated measurement system that directly compares the final implanted screw location to the planned target location in all three anatomical views. A second objective is to quantify the uncertainty associated with the fusion process of aligning preoperative and intra- or postoperative scans. This system was used to quantify accuracy of a robot-assisted pedicle screw insertion procedure using the Mazor X Stealth Edition robotic guidance system in a large cohort of 122 patients with a total of 500 screws implanted across four surgical centers.

3.2 Materials and Methods

3.2.1 Patient Inclusion and Demographics

A total of 122 patients were included in this study with 529 pedicle screws implanted. Of the 529 total screws implanted, 500 screw placements were included in the analysis with 29 excluded due to visibility of the implanted screws in the postoperative scans. Of the total screws analyzed, 420 were in the lumbar spine region, 70 in the sacral, and 10 in the thoracic. 115 of the patients had 3 or less vertebrae fused together and the remaining 7 patients had 4 or more vertebrae included in their fusions. Of the 122 patients, 72 were female and 50 were male. The mean age of the patients was 62 ± 12 years. The mean body mass index (BMI) of the patients is 30.0 ± 5.6 and 13 patients were current smokers. Patient clinical diagnoses included 44 patients with spondylolisthesis, 37 with spinal stenosis, 7 with flat back deformity, 7 with lumbar instability, 5 with spondylolysis, 2 with retrolisthesis, 1 with each of the following - scoliosis, recurrent disc

herniation, recurrent synovial facet cyst, pseudoarthritis, and 16 with a combination of the above conditions. These patients underwent surgery at four surgical centers, with a single surgeon operating at each center. The minimum number of screws implanted at any given center was 84. Of the total cases, 108 were minimally invasive and the other 14 were open procedures. As this was a retrospective study where all data were collected as part of standard patient care and these data were anonymized at their respective centers before inclusion in this work, this study was granted exempt status by the Boise State University Institutional Review Board.

3.2.2 Surgical Procedure

All patients received a preoperative computed tomography (CT) scan. This scan is used by the surgeon to plan pedicle screw placement in the navigation software (Mazor, version 4.0 and 4.2; Medtronic, Dublin, Ireland). On the day of surgery, the patient is held in a prone position. An O-Arm is used to take a fluoroscopy scan of the patient to register their position and the position of the robotic arm in relation to their anatomy (Figure 3.1a). This scan is used to register the patient's current position with the scan used for the preoperative plan. The robotic arm is then moved to the necessary position for the pre-planned screw trajectory. The robotic end effector is used as a guide while the surgeon inserts the screw (Figure 3.1b). The screw placements are verified either intraoperatively using an O-Arm scan or postoperatively using a CT scan. The scans included in this study to measure placement accuracy include 90 patients (375 screws) that had intraoperative O-Arm images and 32 patients (125 screws) that had postoperative CT images taken between 10 and 17 months after surgery.

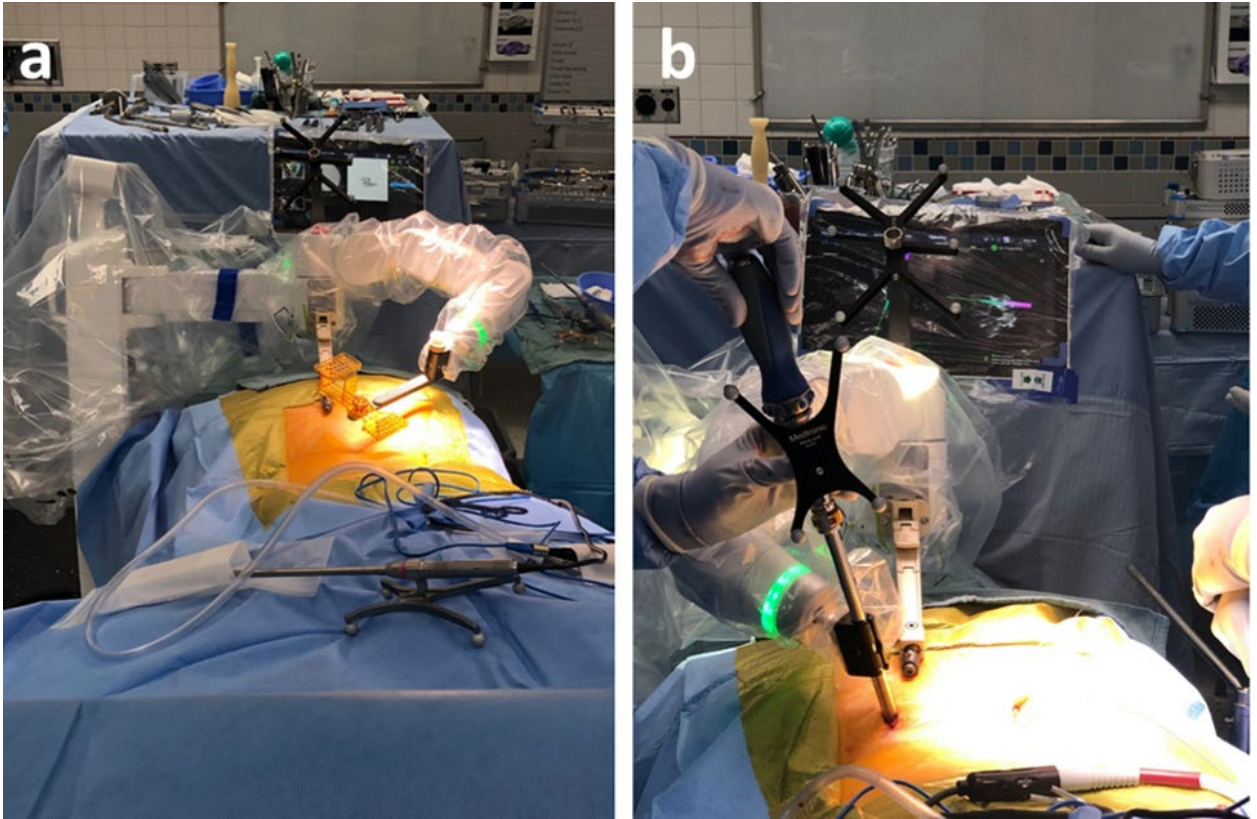


Figure 3.1 (a) Registration of the robotic platform in the operating room. AP and Oblique intraoperative x-ray images are taken of the patient's bony anatomy and the amber-colored frame attached to the robot arm positioned over the patient's body. These images establish the patient's anatomy and relate it back to the preoperative scan used to plan the screw placements. (b) Placement of percutaneous screws through the robotic end effector with real-time navigation on the guidance system screen.

3.2.3 Screw Placement Accuracy

Deviation from the intended screw location was determined in all three anatomical planes. The metrics measured to determine placement accuracy are medial-lateral (ML) and superior-inferior (SI) deviation in the pedicle region, perpendicular deviation and angular deviation in the axial plane, and perpendicular deviation and angular deviation in the sagittal plane (Figure 3.2). These metrics are measured between the target screw location from the preoperative plan and the actual location of the implanted screw as seen on post-implantation scans.

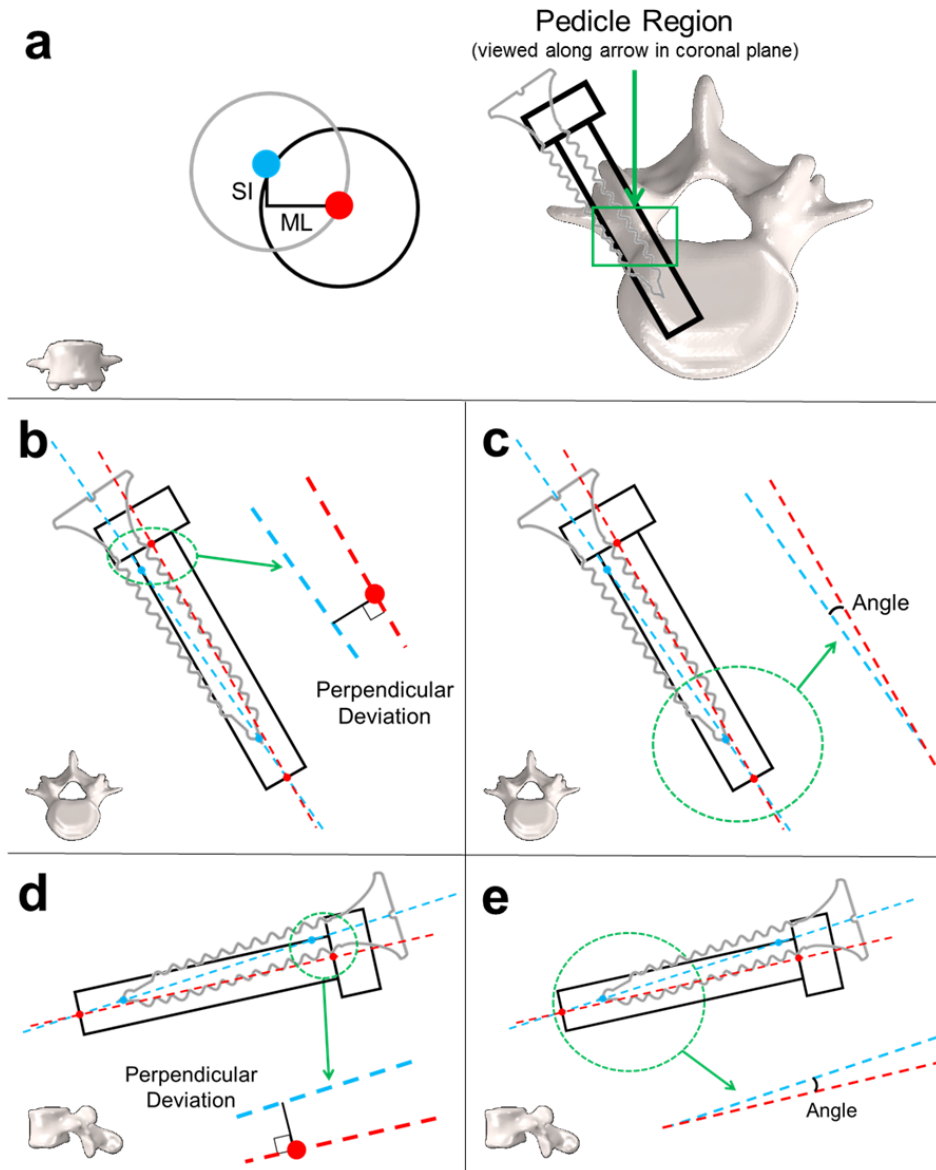


Figure 3.2 Metrics used to determine pedicle screw placement accuracy. All measures are determined as the deviation between the planned target screw location (red lines and dots) and implanted screw location (blue lines and dots). (a) Superior-inferior (SI) and medial-lateral (ML) deviation in the pedicle region measured in the coronal plane. Perpendicular deviation in the (b) axial and (d) sagittal planes from the base of the screw tulip to the implanted screw trajectory. Angular deviation in the (c) axial and (e) sagittal planes measured as the angle between the trajectories of the planned and implanted screw locations.

An algorithm was developed in MATLAB 2020b (The Mathworks, Inc., Natick, MA) to automate the measurement of screw placement accuracy. This algorithm was adapted from a previously published approach to automatically quantify electrode

placement accuracy after deep brain stimulation surgery in patients with Parkinson's Disease.⁹⁸ It utilizes image processing tools to locate the target screw location and the implanted screw, and then quantifies placement accuracy. Color filtering is used to locate the planned screw locations in the images. The implanted screws are found using a contour map based upon the grayscale values of the intra- or postoperative image. Due to all measurements being taken in the pixel space of the image, all distance measurements must be converted from pixels to a standard unit of mm. The ML and SI deviations in the pedicle region are measured as the horizontal and vertical distances, respectively, between the center of the target screw location and the center of the implanted screw (Figure 3.2a). The center locations are determined when looking at the screws from the coronal plane at the smallest diameter of the pedicle. The perpendicular deviations in the axial and sagittal planes are measured as the perpendicular distance from the posterior of the planned screw shank at the base of the tulip to the trajectory along the shank of the implanted screw (Figure 3.2b,d). The angular deviations in the axial and sagittal planes are the angle between the trajectory of the target screw location and the trajectory along the shank of the implanted screw (Figure 3.2c,e).

3.2.4 Measurement Uncertainty

To compare the location of the implanted screws to the target screw locations, the post- or intraoperative scan, showing the implanted screws, must be fused to the preoperative CT scan containing the target location. This involves aligning pre- and intra- or postoperative scans in all three anatomical planes (Figure 3.3). The fusion process is completed in the Mazor robotic software (RND version 4.2) and begins with an initial alignment by the software registration algorithm. Then manual adjustment, specifically

rotation and translation in six degrees of freedom, occurred until the spinous processes, transverse processes, base of vertebral body, and spinal canal were properly aligned. Fusions were performed by two evaluators with each evaluator completing all fusions within a single center.

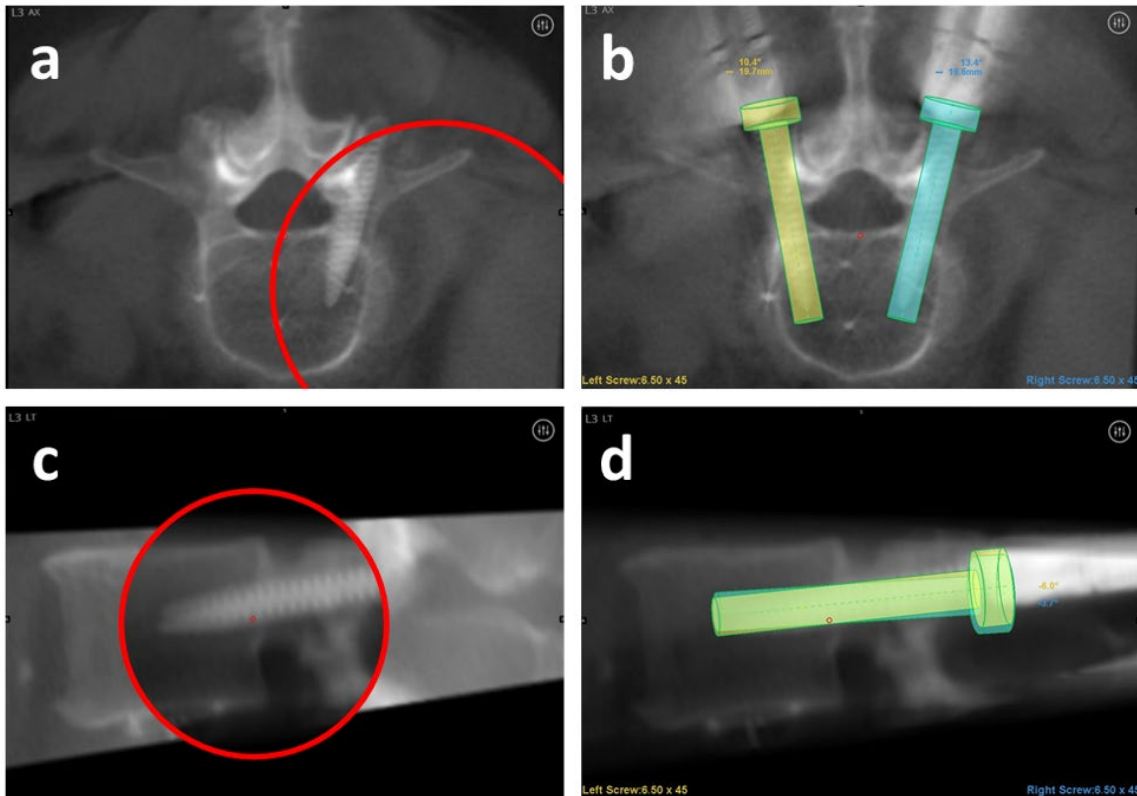


Figure 3.3 Fusion of intra- or postoperative images to preoperative CT scans in the (a) axial and (c) sagittal views. The postoperative image showing the implanted screw locations is displayed inside of the red circle. The planned locations for the screws, with the left implant shown in yellow and the right implant shown in blue, are overlain on the postoperative image in the (b) axial and (d) sagittal views.

The fusion of the preoperative and intra- or postoperative scans is the only part of the measurement process that requires human input that could cause potential variance to the calculated screw placement accuracies. To quantify this uncertainty associated with the fusion process, a subset of 40 implants (10 from each center) were fused by both evaluators. The fusion process maps the planned screw location from the preoperative

image onto the scans showing the implanted screws. When this is performed independently by both evaluators, the target location shows up in a slightly different location on the intra- or postoperative scan. The difference between the two mapped targets is the uncertainty associated with the fusion process. This uncertainty was calculated for the ML and SI deviations in the pedicle region and angular deviations in the axial and sagittal planes.

To measure the effect this fusion uncertainty had on the overall screw placement accuracy values, the interobserver variability of the final placement accuracy values was calculated. The same subset of 40 implants as those used to calculate the uncertainty in the measurement system were utilized. Each implant was evaluated using the automated measurement system for all six screw placement accuracy metrics. The resulting placement values for each evaluator were compared to see if there were statistical differences.

3.2.5 Grading Scale Placement Accuracy

The Gertzbein and Robbins criteria was used to grade screw placement accuracy using conventional methods.⁵² All measurements and classifications were performed by an independent radiologist. Placements were given a grade of A through E with the following criteria: (A) screw is fully within the pedicle, (B) 2 mm or less deviation outside of the pedicle, (C) greater than 2 and up to 4 mm deviation outside of the pedicle, (D) greater than 4 and up to 6 mm deviation outside of the pedicle, and (E) greater than 6 mm deviation outside of the pedicle.

3.2.6 Manual Measurement Comparison

The development of the automated measurement process eliminates human variance in measurement and bias. To assess the benefit of an automated approach, the same six screw placement accuracy measures described previously were manually and independently measured by two evaluators. The manual measurements were performed on a subset of 40 implants (10 from each center). Each evaluator followed the same set of step-by-step instructions for each metric. The measurements were taken after the evaluators completed tutorials on the software and were confident using the necessary tools. The manual measurements were compared to each other as well as the automated placement values.

3.2.7 Statistical Metrics

Statistical comparisons between manual measurements, interobserver reliability, and left and right sides were quantified using a paired t-test. The effects of center and spinal region were evaluated using a one-way ANOVA. A p-value below 0.05 was considered statistically significant. All accuracy values given are mean \pm one standard deviation.

3.3 Results

A total of 500 pedicle screws were analyzed, of which 420 were in the lumbar spine region, 10 in the thoracic, and 70 in the sacral. The screw placement accuracies based on spinal region are shown in Table 3.1. The mean ML deviation in the pedicle region is 1.75 ± 1.36 mm and 333 screws (66.6%) had a deviation less than or equal to 2 mm. Of the total screws, 123 and 377 were implanted with a deviation in the medial and lateral directions, respectively. The mean SI deviation in the pedicle region is 1.52 ± 1.26

mm and 370 screws (74.0%) had a deviation less than or equal to 2 mm. The deviation occurred in the superior direction in 141 screws and in the inferior direction in 359 screws. In the axial plane, the mean perpendicular deviation is 2.00 ± 1.54 mm and the angular deviation is $2.40^\circ \pm 2.07^\circ$. In the sagittal plane, the mean perpendicular deviation is 2.16 ± 1.74 mm and the angular deviation is $3.88^\circ \pm 3.43^\circ$.

Table 3.1 Screw Placement Accuracy Values Based on Spinal Region (mean \pm SD). Statistical significance ($p < 0.05$) indicated by *.

	Lumbar	Sacral	Thoracic
Number of Implants	420	70	10
ML Deviation in Pedicle [mm]	1.79 ± 1.38	1.63 ± 1.25	1.25 ± 1.43
SI Deviation in Pedicle [mm]*	1.42 ± 1.16	2.21 ± 1.63	1.16 ± 0.83
Perpendicular Deviation in Axial Plane [mm]	2.05 ± 1.56	1.78 ± 1.39	1.64 ± 1.49
Angular Deviation in Axial Plane [$^\circ$]	2.45 ± 2.12	2.18 ± 1.87	1.81 ± 1.03
Perpendicular Deviation in Sagittal Plane [mm]*	2.05 ± 1.68	2.83 ± 1.96	2.15 ± 1.79
Angular Deviation in Sagittal Plane [$^\circ$]	3.81 ± 3.32	4.33 ± 4.12	3.49 ± 2.81

The uncertainty of the measurement process associated with the fusion step was calculated on a subset of screws that included 10 from each of the four centers. The resulting uncertainty in the ML and SI deviations in the pedicle region are 0.67 ± 0.81

mm and 1.45 ± 2.00 mm, respectively. The uncertainty associated with angular deviation in the axial plane is $1.69^\circ \pm 1.22^\circ$ and sagittal plane is $1.85^\circ \pm 1.66^\circ$. The potential effects of the uncertainty in the measurement process can be seen in Figure 3.4.

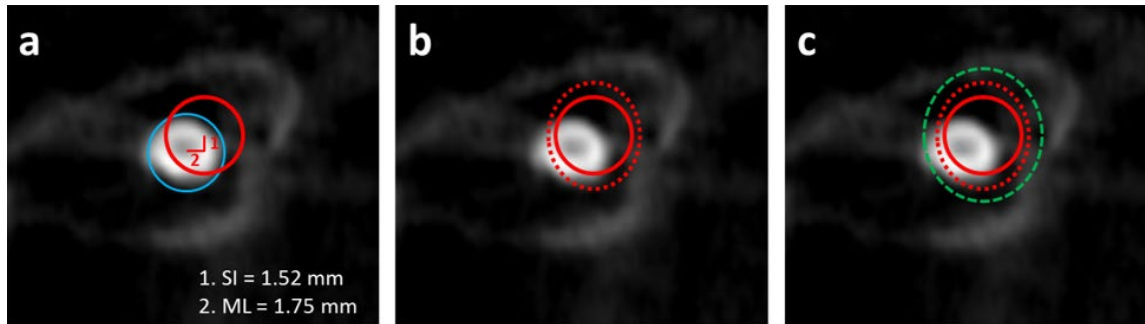


Figure 3.4 (a) Target screw location (red) in relation to the implanted screw (outlined in blue) when looking from the coronal plane into the pedicle region with the average ML and SI deviation for the entire cohort shown. (b) Fusion uncertainty (dashed red) associated with the portion of the measurement process that involves fusing the preoperative CT to the intra- or postoperative scan. (c) One standard deviation (green) of the ML and SI measurements of the entire dataset. The area inside of the green dashed oval accounts for all variability in the measurement process.

From this same subset of patients, the screw placement accuracies were calculated for each evaluator using the automated measurement system to quantify any interobserver variability occurring during the fusion process. The results show no statistical differences between any of the six metrics. The angular deviation in the sagittal plane was trending towards significance ($p = 0.053$). This shows that different evaluators performing the fusions does not significantly change the overall screw placement accuracy results but the additional uncertainty the fusion process adds to the measurements should be considered.

The screw placement accuracies were compared for differences between left and right-side implants, center, and spinal region. There was a significant difference between left and right screw implants in the SI deviation in the pedicle region and perpendicular deviation in the sagittal plane. There was a significant difference between the four centers

in all metrics except the perpendicular deviation in the axial plane. The SI deviation in the pedicle region and perpendicular deviation in the sagittal plane are the two metrics that had significant differences between the spinal regions implanted.

The grading classifications for the 500 implanted screws are 356 A, 130 B, 8 C, 3 D, and 3 E. 486 screws (97.2%) were within the clinically acceptable range with a deviation less than or equal to 2 mm outside of the pedicle region. The primary direction a breach occurred in, reported for the 144 screws not graded as an A, was medial in 22.2% of cases, 37.5% lateral, 22.2% superior, and 18.1% inferior.

The accuracy values for the manual measurements and their comparison automated values for the subset of 40 implants are in Table 3.2. There was a statistical difference between evaluator 1 and both evaluator 2 and the automated measurements in the ML deviation in the pedicle region. There was a statistical difference between evaluator 2 and the automated measurements in the SI deviation in the pedicle region.

Table 3.2 Manual Measurement Screw Placement Accuracy Values (mean \pm SD). Statistical significance ($p < 0.05$) indicated by * (between manual 1 and manual 2), ^x (between manual 1 and automated), and ^{II} (between manual 2 and automated).

	Manual Set 1	Manual Set 2	Automated Measurement
ML Deviation in Pedicle [mm] * ^x	2.00 \pm 1.38	1.70 \pm 1.48	1.72 \pm 1.42
SI Deviation in Pedicle [mm] ^{II}	1.35 \pm 1.06	1.32 \pm 1.25	1.46 \pm 1.28
Perpendicular Deviation in Axial Plane [mm]	2.02 \pm 1.37	2.09 \pm 1.63	1.79 \pm 1.36
Angular Deviation in Axial Plane [°]	2.04 \pm 1.49	2.32 \pm 2.00	2.12 \pm 1.81
Perpendicular Deviation in Sagittal Plane [mm]	2.08 \pm 1.46	2.12 \pm 2.16	2.09 \pm 1.77
Angular Deviation in Sagittal Plane [°]	3.41 \pm 2.69	3.04 \pm 2.27	3.16 \pm 2.21

3.4 Discussion

The screw placement accuracies detailed in this study were calculated using an automated measurement system that can analyze screw accuracy as it relates to planned target location for multiple metrics in all anatomical views. The average accuracy values reported here in both the ML and SI directions within the pedicle region are below the traditional clinically accepted metric of 2 mm. The majority of those deviations occurred in the lateral and inferior directions. Of the total implants, 66.6% had an accuracy to plan value less than or equal to 2 mm. This is a much smaller percentage than the 97.2% of acceptable placements according to the Gertzbein and Robbins classification.⁵² The key difference between the new measurement system presented here and conventional

grading scales is that grading scales measure the amount of screw outside of the pedicle, but presented here is the amount the screw deviated from the planned location. The two measures are not directly comparable, and a deviation over 2 mm using the automated measurement system does not directly equate to a C or worse rating according to the grading scale (Figure 3.5).

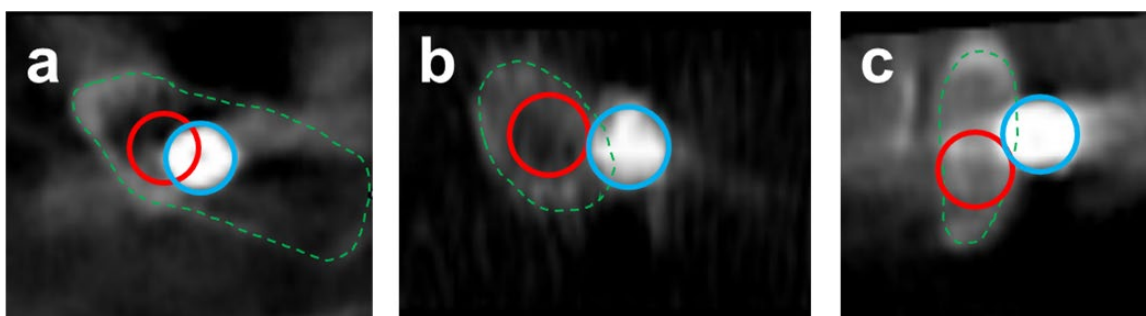


Figure 3.5 Measurement differences between accuracy of the implanted screw (blue) in relation to the planned location (red) versus conventional grading scale metrics. The pedicle edge (green dashed line) is shown that was used to judge placement outside of the pedicle region. (a) Categorized as A using grading scale but has a ML deviation of 3.21 mm away from the planned target location. (b) Grading scale category B with a ML deviation of 7.38 mm from the planned location. (c) Grading scale category C and a ML deviation from the target trajectory of 5.14 mm.

The accuracy values in the ML and SI directions within the pedicle region are greater than the robotic system trajectory accuracy of 1.5 mm.⁶⁸ The navigation camera used with the guidance system has a spatial accuracy of 2 mm,⁶⁸ which adds variance to the accuracy quantified in this study because the camera was assumed to be in the correct orientation. Another source of variance to the measurements is deviation that can occur during the fusion process of the preoperative plan to the intra- or postoperative scan. Fusion is the only manual part of the measurement process but the uncertainty and its significance were quantified to better verify screw placement accuracies (Figure 3.4).

Previous studies have compared the accuracy of implanted screws to the robotic preoperative plan.^{92, 93, 97} One study measured entry point deviation and axial and lateral

angular deviation on 178 screws in 63 patients.⁹³ The average angles measured in this study for the angular deviations in the axial and sagittal planes were higher than those reported previously⁹³ (2.40° compared to 2.2° and 4.21° compared to 2.9°). A second study performed the analysis on 646 screws in 139 patients but only measured deviation in the axial and sagittal planes based upon entry and exit point deviation.⁹² The study presented here also includes the ML and SI deviation in the pedicle region, which is a key clinical metric.

Previous studies looking at screw accuracy, both using a grading scale or comparing directly to the planned screw location, have utilized manual measurements, whereas this study used an automated measurement algorithm. The automated measurement algorithm removes human variance after the fusion step, which is a required step for all comparisons of implanted locations to robotic preoperative plans. The benefit to eliminating human input was illustrated by the significant difference between the ML and SI deviation values in the pedicle region between the manual measurements and the automated measurement values, (Table 3.2) particularly since those are the most clinically relevant metrics. The automated measurement system can also more easily and consistently quantify large cohorts.

There were statistical differences in multiple metrics between the left and right side implants on a single vertebrae, spine region, and center. The difference in accuracy between implants on the same vertebrae could be caused by artifact from the first screw when looking at intraoperative images. Differences between spinal regions could be due to the ease of access to specific vertebrae and the angles necessary to accurately implant the screws. Previously there was no significant difference found between deviations in

the thoracic, lumbar, and sacral regions,⁹³ which is not the case in this study, but there were significantly more implants in the lumbar region than the other two spine regions.

Accuracy differences between centers can be attributed to a variety of factors including length of time using the robot because a long training curve has been established for robot-guided procedures^{99, 100} and variability in the cases performed between centers including spinal region implanted. The difference between centers can also be attributed to the difference in imaging used for the accuracy measurements. One of the four centers used postoperative CT imaging that was taken approximately one year after surgery while the other three used intraoperative O-Arm images from the day of surgery. It has been shown that screw loosening is a common complication after spinal surgery that can occur in anywhere from 1 to 60% of cases depending on the bone density of the patient.¹⁰¹ Loosening was quantified for the 32 patients (125 screws) with postoperative CT images based upon the presence of a radiolucent zone around the implanted screws.¹⁰² It was found that 4.8% had a radiolucent zone of less than 1 mm, 1.6% had a radiolucent zone of greater than 1 mm, and 93.6% had no sign of loosening. The average placement accuracy of the 375 implants with intraoperative image, excluding the postoperative CT scans, was 1.63 ± 1.19 mm in the ML direction and 1.39 ± 1.18 mm in the SI direction. An additional difference between the centers is that one used both divergent (medial-to-lateral) and convergent (lateral-to-medial) approaches while the other three used only convergent approaches. Regardless of the approach used though, both divergent and convergent approaches had the same percentage of implants that breached the pedicle.

This study was limited by minor manual input during the fusion process of overlaying the preoperative plan onto the intra- or postoperative scan, which trended toward having interobserver variability in the sagittal plane. This could be due in part to the variability of the intra- or postoperative images since some centers took intraoperative O-Arm images and others used postoperative CT scans. Additionally, the sample sizes in the thoracic and sacral spinal regions were limited and future work should include larger cohorts to verify the differences observed here between regions. The accuracy values were also not related to any complications in the operating room or clinical outcomes of the patient postoperatively, as this data was not available, but could be included in future analyses of screw-to-plan accuracy.

3.5 Conclusions

This study used a novel measurement system to analyze the robotic accuracy of the Mazor X Stealth Edition robotic guidance system using six metrics that analyze the screw placements from all three anatomical views. Implementing an automated measurement algorithm ensured measurement consistency across centers and regions. This was demonstrated across four surgical centers in 500 implanted screws.

3.6 Acknowledgements

This work supported in part by Medtronic. This material is based upon work supported by the National Science Foundation Graduate Research Fellowship Program under Grant No. 1946726 and the Center of Excellence in Biomedical Research through the Institutional Development Award (IDeA) from the National Institute of General Medical Sciences of the National Institutes of Health under Grant Nos. P20GM109095 and P20GM103408 and the National Science Foundation S-STEM Gateway Scholarships

in Biological Sciences under Grant Award No. DUE-1644233. Any opinions, findings, and conclusions or recommendations expressed in this material are those of the author(s) and do not necessarily reflect the views of the National Science Foundation.

3.7 Author Justifications

V.L.V: design of the study, developed automated measurement algorithm, performed all analyses, prepared figures, primary writer. K.A.S.: postoperative scan registration and fusion of preoperative to postoperative scans. M.C.: postoperative scan registration and fusion of preoperative to postoperative scans. R.V.C.: surgical implantation of screws and interpretation of results. J.P.: surgical implantation of screws and interpretation of results. G.P.: surgical implantation of screws and interpretation of results. E.S.: surgical implantation of screws and interpretation of results. P.B.: clinical grading of screw placements and interpretation of results. C.K.F.: study concept, design of the study, interpretation of results. All authors contributed to editing and revision of the manuscript for intellectual content.

CHAPTER FOUR: INTEGRATION OF NEURAL ARCHITECTURE WITHIN A
FINITE ELEMENT FRAMEWORK FOR IMPROVED
NEUROMUSCULOSKELETAL MODELING*

This chapter is published by Springer Nature in *Scientific Reports* and should be referenced appropriately.

Status:

This manuscript was accepted for publication in November 2021.

Reference:

V.L. Volk, L.D. Hamilton, D.R. Hume, K.B. Shelburne, C.K. Fitzpatrick, “Integration of Neural Architecture within a Finite Element Framework for Improved Neuromusculoskeletal Modeling.” *Scientific Reports*, **11**, Article Number: 22983 (2021).

Reproduce by permission of Springer Nature.

*This chapter includes modifications from the originally published version.

INTEGRATION OF NEURAL ARCHITECTURE WITHIN A FINITE ELEMENT
FRAMEWORK FOR IMPROVED NEUROMUSCULOSKELETAL MODELING

Victoria L. Volk^{1,2}

Landon D. Hamilton³

Donald R. Hume³

Kevin B. Shelburne³

Clare K. Fitzpatrick²

Accepted for publication in:

Scientific Reports

November 2021

¹*Micron School of Materials Science and Engineering, Boise State University, Boise, ID,*

USA

²*Mechanical and Biomedical Engineering, Boise State University, Boise, ID, USA*

³*Center for Orthopaedic Biomechanics, University of Denver, CO, USA*

Abstract

Neuromusculoskeletal (NMS) models can aid in studying the impacts of the nervous and musculoskeletal systems on one another. These computational models facilitate studies investigating mechanisms and treatment of musculoskeletal and neurodegenerative conditions. In this study, we present a predictive NMS model that uses an embedded neural architecture within a finite element (FE) framework to simulate muscle activation. A previously developed neuromuscular model of a motor neuron was embedded into a simple FE musculoskeletal model. Input stimulation profiles from literature were simulated in the FE NMS model to verify effective integration of the software platforms. Motor unit recruitment and rate coding capabilities of the model were evaluated. The integrated model reproduced previously published output muscle forces with an average error of 0.0435 N. The integrated model effectively demonstrated motor unit recruitment and rate coding in the physiological range based upon motor unit discharge rates and muscle force output. The combined capability of a predictive NMS model within a FE framework can aid in improving our understanding of how the nervous and musculoskeletal systems work together. While this study focused on a simple FE application, the framework presented here easily accommodates increased complexity in the neuromuscular model, the FE simulation, or both.

4.1 Introduction

Human movement requires complex interactions between the nervous system and musculoskeletal system. The nervous system generates electrical signals in the brain that are transmitted through the spinal cord to the neuromuscular junction. At the junction, the electrical signal is converted to a muscle activation that generates a muscle force causing

motion at the joints. A major limitation in studying human systems, particularly the nervous system and the neuromuscular junction, is the challenge of performing *in vivo* experiments. In humans, studies investigating the neuromuscular junction are oftentimes difficult or infeasible to perform, particularly due to ethical concerns.²³ Recording electrical activity at the cellular level can be dangerous to perform in humans and although there are types of external recordings, such as electroencephalography (EEG) and electromyography (EMG), these recordings occur at the brain and muscle level and do not provide cellular level data about what is occurring at the neuromuscular junction. This is where computational models, specifically fully predictive neuromusculoskeletal (NMS) models, can play a significant role. NMS models include components of both the nervous and musculoskeletal systems necessary to fully study the neuromuscular junction and resulting movement in a manner that is not possible *in vivo*.

In the field of biomechanics, musculoskeletal simulations are used to perform analyses capable of assessing geometry, loading and boundary conditions, and material properties in situations that cannot be measured within a living organism.¹⁰³ Two key types of musculoskeletal models are rigid body and finite element (FE) models. Rigid body simulations are useful for simulating musculoskeletal dynamics and calculating joint kinematics from experimental data.³² For more complex problems, such as detailed representation of the joints that include soft tissue geometries and material properties, FE analyses are often more useful. FE simulation environments (e.g. FEBio, febio.org; Abaqus, Simulia) can be used for both rigid-body simulations and more complex FE simulations. However, neither of these approaches involve neural control to drive the musculoskeletal models.

Neural data-driven models that use EMG as the input are an exception to this lack of neural control in driving musculoskeletal models.¹⁷⁻²² They are beneficial for in-depth studies to quantify musculoskeletal function and control²¹ via neural drive, or common synaptic input, to the spinal cord and muscles.¹⁷ However, these EMG driven models inform force production based only on decomposition of discharge times and no other neural anatomy. They also only operate in a feed-forward method that does not have the feedback from the musculoskeletal system to the nervous system required for the nervous system to adapt during movement.

Alternatively, fully predictive NMS models utilize a pool of motor neurons²⁴⁻²⁶ or neural networks with motor neurons, Renshaw cells, and interneurons²⁷⁻³¹ to simulate a neural command that generates a simulated muscle force used in a musculoskeletal model. This means that the signal being converted into muscle force is based upon a variety of neural factors such as anatomy, types of ion channels, and connectivity between different neurons, which can all be modified to study their effects. Neural factors can be varied throughout the simulation that make the overall outputs representative of the adaptation that occurs in the body. This is a key benefit of fully predictive models, rather than studying musculoskeletal function from a specific neural drive.²³

NEURON is an open-source, Python-based simulation environment that is used to create models ranging from individual neurons to networks of neurons.³⁷ Previously developed models in NEURON have been able to accurately simulate the neural drive to muscles,³⁸ but do so in a single motor unit that would not represent in vivo muscle contraction. Motor unit recruitment and rate coding are the two ways in which muscle forces in skeletal muscle are varied and controlled.³⁹ If a neuromuscular model does not

exhibit these two functions, then it cannot replicate muscle force or movement generation in an in vivo manner. Recruitment is the concept that not all motor units (a motor neuron and all the muscle fibers it innervates) are active at a given time, but instead are recruited in an orderly manner.³⁹ Motor units are recruited in size order from smallest to largest, following Henneman's size principle,⁴⁰ where ones that generate smaller forces are recruited first followed by larger force producing motor units. Rate coding involves a proportional relationship between stimulation intensity and discharge rate, such that as the intensity of a stimulus increases, so does the rate of discharging action potentials.³⁹ All motor neurons have a recruitment threshold, below which no action potential will be generated. For stimuli that are above the recruitment threshold there exists a linear relationship between the level of injected current and the resulting discharge rate. The discharge rate will continue to increase with increased current intensity until the peak rate is achieved. After this point, there is little variation in discharge rate, even with a continued increase in excitatory drive. NEURON by itself simulates the electrical impulses representative of movement, but does not simulate the actual movement. By integrating NEURON with a FE environment, we can create a comprehensive multiscale simulation framework with the ability to model movement from initial neural command generated in the brain at the cellular level through to the resulting muscle contraction necessary for joint movement at the human systems level.

In this study, we develop a fully predictive NMS model that uses an embedded neural architecture within a FE environment to simulate muscle activation and force. We demonstrate the ability of this integrated framework to implement motor unit recruitment and rate coding capabilities in the human physiological range. This is accomplished by

integrating finite element (Abaqus, Simulia, Providence, RI) and NEURON simulation environments and is demonstrated here using a motor neuron pool innervating a soleus muscle in a simple musculoskeletal model. A combination of complex neuronal networks with musculoskeletal modeling is needed for multifaceted analyses and simulation of the interaction between the nervous and musculoskeletal systems. The novel framework developed in this study has been implemented here in a simple FE model. However, this framework can accommodate increased complexity in the neuromuscular model, the FE simulation, or both, facilitating the development of multi-system models that may be used in future work for investigation of neurodegenerative or neurodevelopmental conditions.

4.2 Methods

The design approach for the NMS model was to develop an accurate representation of nerve-muscle interaction that would mimic *in vivo* muscle activation. To do this, the slow motor unit model developed by Kim³⁸ in the NEURON simulation environment (version 7.7.2) was modified to generate a motor neuron pool consisting of 310 motor units and incorporated into a FE musculoskeletal model based upon a previously developed model.¹⁰⁴

The neuromuscular model developed by Kim consists of a single motor neuron innervating a cat soleus muscle³⁸ and is publicly available on ModelDB.¹⁰⁵ The alpha motor neuron has 311 dendrites connected to the soma, which is then connected to the axon hillock and initial segment (Figure 4.1). The three-dimensional neuron geometry was reconstructed from scans of a cat spinal motor neuron.³⁸ All cellular components exhibit passive properties, and the soma, dendrites, axon hillock, and initial segment also include various ion channels for active property definitions. The potassium (delayed

rectifier, calcium-activated) and sodium (fast, persistent) channels elicit spiking in all active cells, and the calcium channels (N-type, L-type) play a vital role in bursting activity that elicits force generation in muscles required for movement. The model of the neuromuscular junction includes components for calcium dynamics, activation dynamics, and force production. The force production is based on a Hill-type muscle model with active and passive force generating elements.³⁸

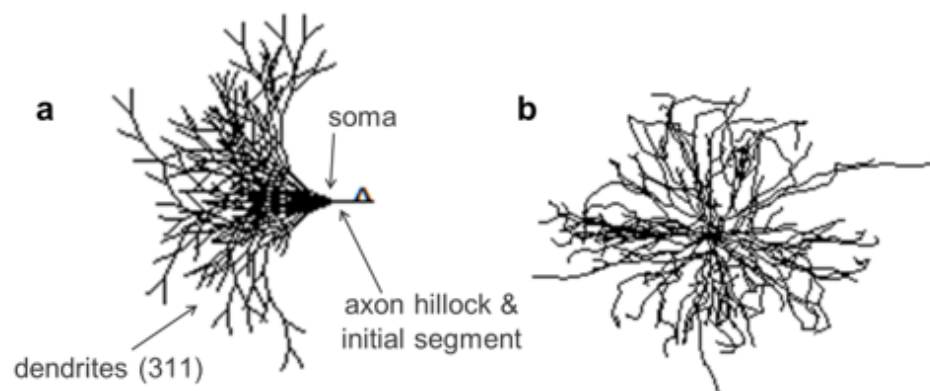


Figure 4.1 (a) 2D and (b) 3D representations of alpha motor neuron.

The musculoskeletal model is a simplified representation of a human ankle joint (Figure 4.2). All geometry in the model was segmented from the Visible Human Male dataset.¹⁰⁶ The model includes the soleus and tibialis anterior muscles represented as axial connectors positioned to run through the centroid of the muscle cross-sectional geometry. The model also includes the foot bones, tibia, and three-dimensional articular cartilage¹⁰⁴ at the tibia-talus joint. Muscle contraction is controlled by applying the forces from the NEURON simulation calculations to the soleus axial connector. Neural parameters determined for felines have been shown to share many of the same features as those seen in humans,¹⁰⁷ therefore many NMS models of humans utilize feline neural parameters,^{27, 28, 30} as was done in this study.

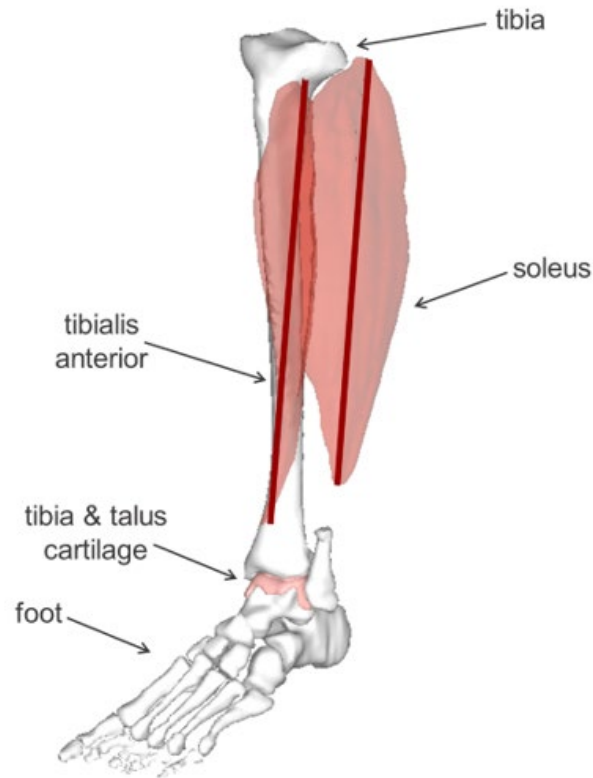


Figure 4.2 Abaqus musculoskeletal model of the ankle joint including geometries of the bones, muscles, and cartilage.

All simulations were performed in Abaqus/Explicit, which included a Fortran user-subroutine (vuamp) as an interface between NEURON and Abaqus (Figure 4.3). NEURON is called every 100 ms of the simulation by running a Python script from inside the Abaqus-specific Fortran subroutine. During the NEURON simulation, the activation calculated in the calcium dynamics and activation dynamics modules is input into the force calculation. The resulting forces are input back into the Fortran user-subroutine to apply to the soleus muscle connector in Abaqus.

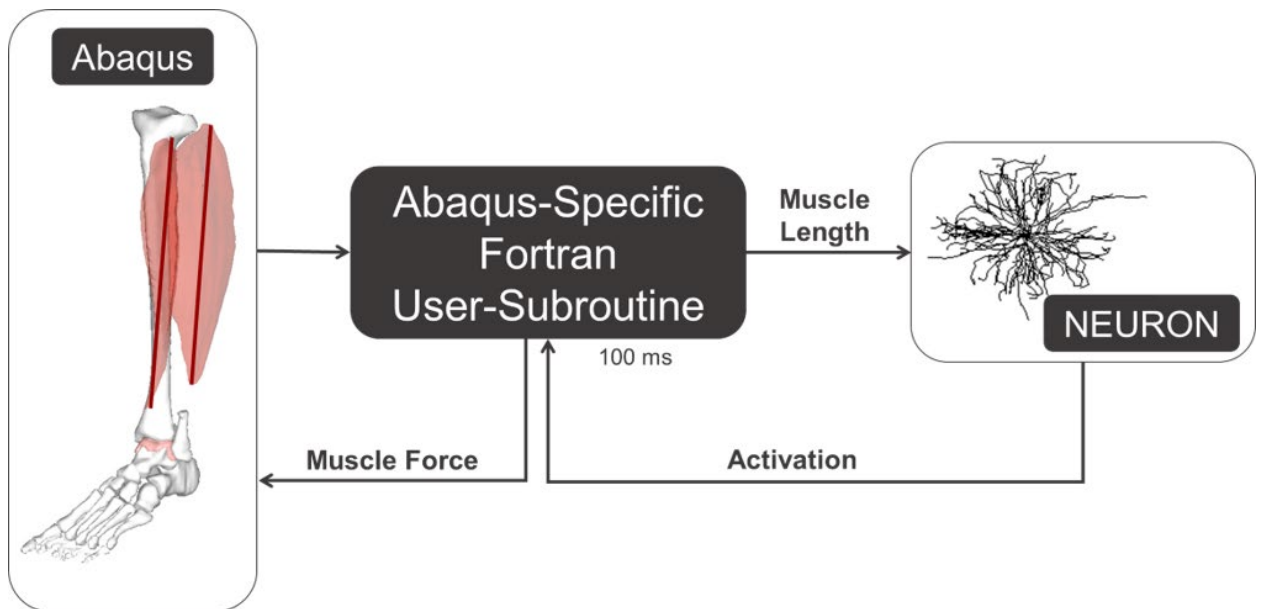


Figure 4.3 Flow of information in the integrated FE NMS model. A NEURON simulation is ran using a call from the Abaqus-specific Fortran user-subroutine every 100 ms. From that simulation, the activation is input into the muscle force calculation. The force is then applied to the soleus muscle in the Abaqus musculoskeletal model.

4.2.1 Verification of Software Integration

An integrated NMS model containing a single motor neuron in the motor neuron pool was used for verification of the two software environments. The same input stimulation profiles as the Kim motor unit model were used as input into the simulation.³⁸ The simulated forces from the single motor neuron FE NMS model were then compared to published results (Figure 4.4) and the RMSE between the output profiles was calculated.

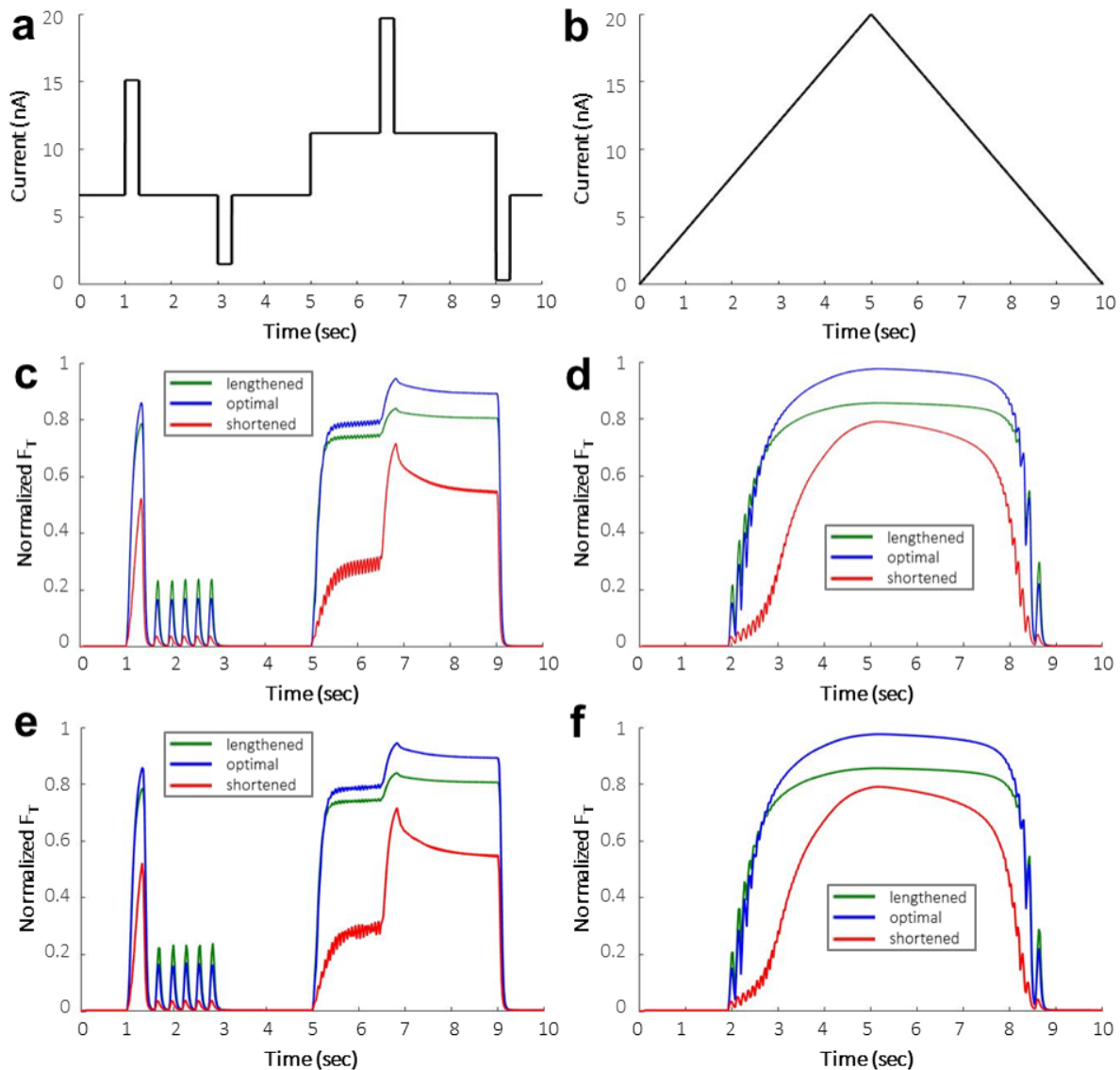


Figure 4.4 (a, b) Input activation profiles from Kim¹⁰⁸ implemented in the single neuron NMS model to show software integration. (c, d) Neuromuscular muscle force results from Kim¹⁰⁸ (Figures 3B and 4B), reproduced here using publicly available data from ModelDB¹⁰⁵. (e, f) Muscle force outputs from FE NMS simulations at lengthened, optimal, and shortened muscle lengths.

4.2.2 Verification of in vivo Neural Behavior

Motor unit recruitment and rate coding capabilities of the model were demonstrated to show the efficacy of the model to produce muscle forces from neural commands generated from a neuronal network. A neuronal network, or motor neuron

pool, was generated using NetPyNE (Networks using Python and NEURON).¹⁰⁹

NetPyNE was chosen to scale a single neuron into a network of 310 motor units because the program was designed specifically to facilitate the development of large-scale, complex neuronal networks written in NEURON. The diameters of the neurons were varied for motor unit recruitment to occur following an exponential distribution³⁹ with a range from 48.8 to 99.7 μm , which is within the diameter range estimated for human motor neurons.³⁰ The peak twitch force for each motor neuron was calculated using an exponential distribution with a 100-fold range.³⁹ In the network model, the total muscle force which was applied to the soleus muscle in the FE environment was calculated as the summation of twitch forces from all motor units.³⁹ A neuronal network of 310 motor units was created to innervate the soleus muscle based on estimates of the total number of motor units per specific muscle in humans and felines.¹¹⁰⁻¹¹³

For motor unit recruitment verification, two activation profiles were applied to all motor units uniformly with randomly distributed noise applied independently for each motor unit. Noise was an offset to the stimulation amplitude at each time point in the simulation and was calculated as a random number from a normal distribution with a mean of 0 nA and standard deviation of 0.2 nA. The modeled motor neuron pool was activated to simulate three amplitudes corresponding to 10%, 40%, and 75% of MVC, or approximately 3 N, 12 N, and 23 N, respectively. These values correspond to feline muscle forces, as the original neuromuscular model parameters³⁸ were tuned to match those experimental values. The first stimulation profile consisted of a 4 s simulated ramp and hold contraction that increased linearly from baseline amplitude to the target force over a 2 s period and was then held constant for an additional 2 s. The second profile

linearly ramped up to the target force and then downward to baseline amplitude, both over a 2 s period. The resulting muscle forces were plotted to ensure they followed accurate muscle behavior.³⁹ The interspike interval, or the time between each subsequent discharge, for each motor unit was calculated at each force level. Additionally, the recruitment threshold, or force at which each motor unit is recruited, was calculated as a %MVC to verify the motor neuron diameter distribution and orderly recruitment.

To demonstrate rate coding in the integrated FE NMS model, a simulation was performed with a ramp and hold force profile which ramped up to 10% MVC over 1 s, followed by 2 s of constant stimulation intensity. The muscle force level of 10% MVC was chosen for comparison to previously published data.¹¹⁴ The discharge rate for each motor unit was calculated as the instantaneous frequency¹¹⁵ and plotted to ensure an accurate relationship between stimulation intensity and discharge rate.

4.2.3 Incorporation of Tissue Mechanics Predictions

The integrated NMS model with a network of 310 motor units was used to verify that the integrated model could be used to study human joint biomechanics. The Hill-type muscle model parameters were modified to match human levels with 300 N of force applied to the soleus muscle for ankle plantarflexion to occur. The contact pressure between articular cartilage at the tibia-talus joint was measured throughout the simulation.

4.3 Results

The muscle force outputs from the single motor neuron FE NMS simulation at three muscle lengths—0 mm, - 8 mm, and - 16 mm—or lengthened, optimal, and shortened muscle states, respectively, reproduced the results reported by Kim³⁸ (Figure

4.4). The root mean square error (RMSE) between the NEURON force predictions of the neural model by itself and the integrated FE NMS model at the optimal muscle length are 0.0513 N and 0.0492 N for the reproduction of Kim Figs. 3b and 4b,³⁸ respectively. The RMSE at the lengthened and shortened muscle states are 0.0467 N and 0.0407 N for Fig. 3b and 0.0424 N and 0.0307 N for Fig. 4b, respectively.³⁸ These RMSE values verify the effective integration of the NEURON and FE software environments.

The total time for a 10.0 s simulation in the FE NMS model framework was approximately 12 min for a single motor neuron. Of that, 8 min was the time taken for the NEURON component of the simulation and 4 min for the Abaqus FE component.

4.3.1 Verification of in vivo Neural Behavior

The integrated FE NMS model scaled to a neuronal network of 310 motor units effectively demonstrated motor unit recruitment for two stimulation profiles at three muscle force levels (Figures 4.5 and 4.6). Motor unit recruitment follows an exponential distribution where smaller motor units are recruited before larger motor units. The resulting muscle forces increased linearly until the last motor unit of that simulation was recruited, which is representative of physiologically accurate muscle behavior at greater force levels.³⁹ The interspike interval plots (Figures 4.5d–f, 4.6d–f) show a decrease in time between successive action potential discharges, or increased discharge rate, with an increase in stimulation intensity and correspond to an increase in percent maximum voluntary contraction (%MVC).

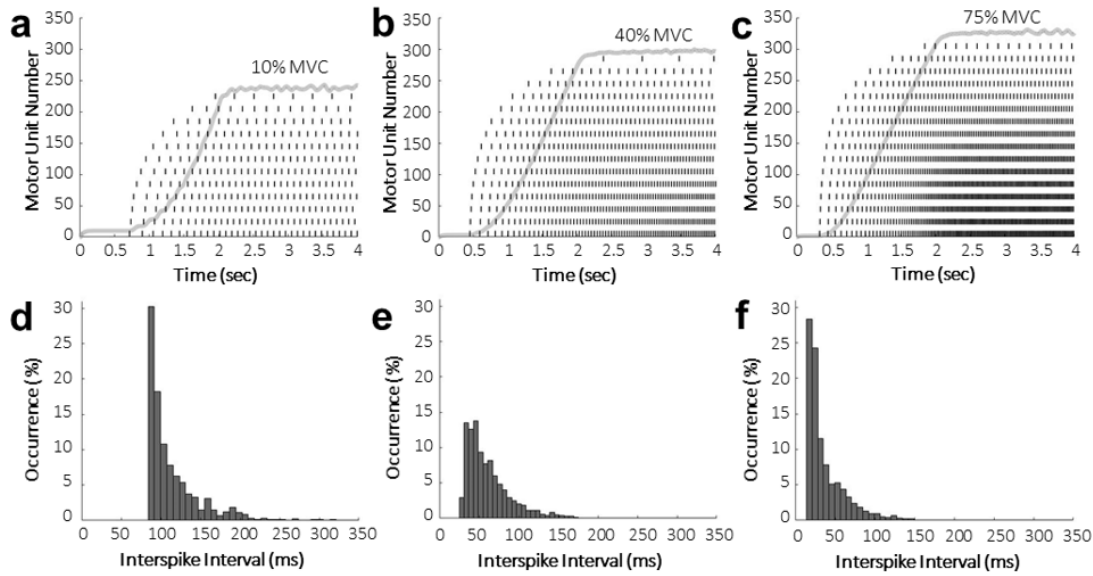


Figure 4.5 (a-c) Discharge times for every 20th motor unit (dashes) with resulting output muscle force (solid line). Motor unit 1 is the smallest and motor unit 310 is the largest, with an exponential size distribution. The stimulation profile increased linearly for two seconds until reaching the peak amplitude corresponding to that %MVC, after which point it was held constant for two seconds. (d-f) Interspike interval measurements between each subsequent discharge for every motor unit through the length of the simulation. Intervals with less than five occurrences were not included in the figure for visualization.

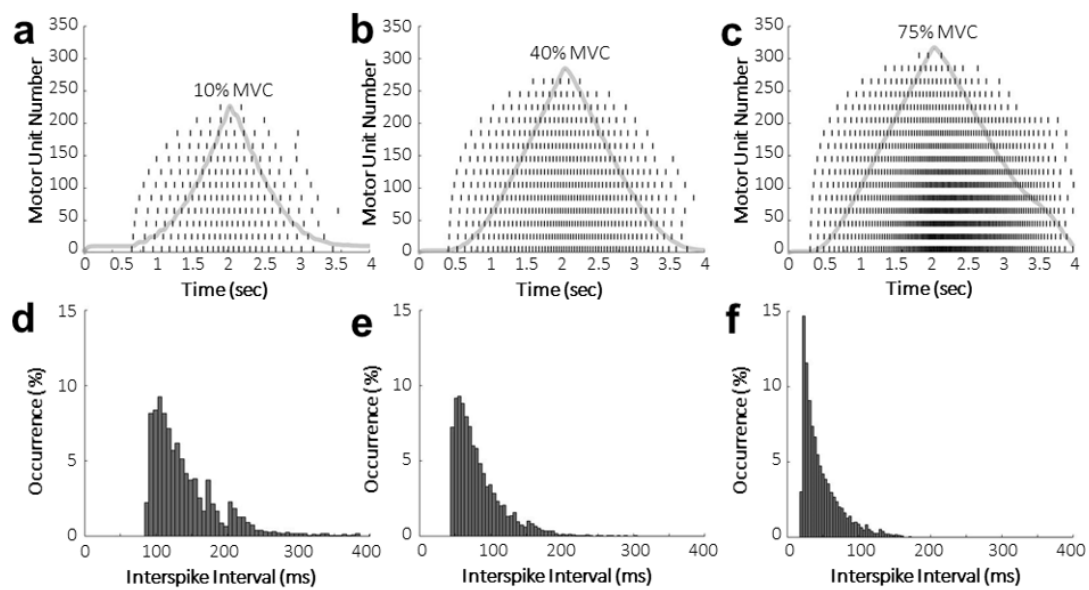


Figure 4.6 (a-c) Discharge times for every 20th motor unit (dashes) with resulting output muscle force (solid line). The stimulation profile increased linearly for two seconds until reaching the peak amplitude corresponding to that %MVC, after which point it decreased linearly back to baseline over two seconds. (d-f) Interspike interval measurements between each subsequent discharge for every motor unit through the length of the simulation. Intervals with less than five occurrences were not included in the figure for visualization.

All motor units had recruitment thresholds between > 0 and 75% MVC and followed an exponential distribution. The average (\pm standard deviation) motor neuron diameter in the neuronal network of 310 motor units was $61.58 \pm 13.08 \mu\text{m}$. The average (\pm standard deviation) motor neuron diameter for motor units recruited between 0 – 30% MVC was $57.77 \pm 8.25 \mu\text{m}$. The average (\pm standard deviation) motor neuron diameter for motor units recruited between 50 and 75% MVC was $94.60 \pm 3.10 \mu\text{m}$.

The neuronal network exhibits rate coding based upon the discharge rates of each motor unit, shown for two representative motor units (Figure 4.7). Below the minimum discharge rate (6.78 nA), no spiking occurs. After the minimum discharge rate, there is a linear relationship between stimulation intensity, represented by an increase in amplitude

of the applied current, and the discharge rate. This relationship continues until the peak discharge rate is reached, after which point the discharge rate has little variation.

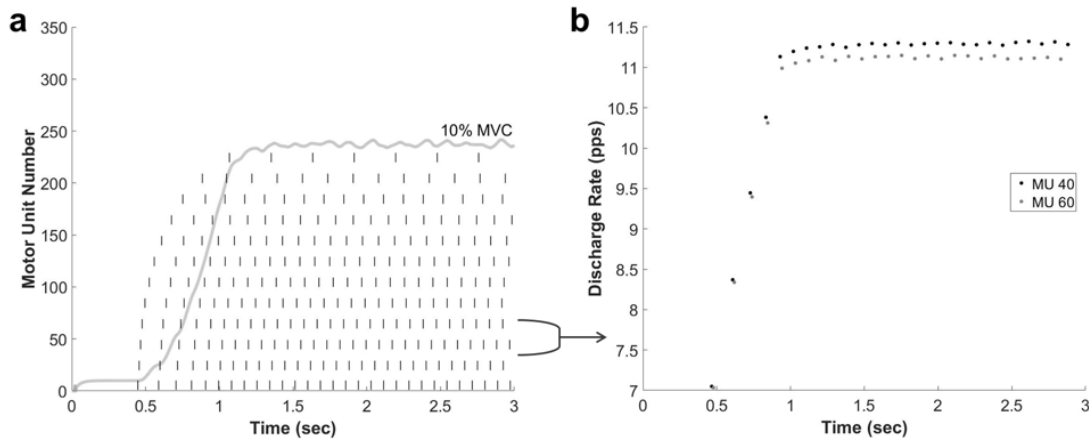


Figure 4.7 (a) Discharge times for every 20th motor unit (dashes) with resulting muscle force output (solid line). The stimulation profile increased linearly for one second until reaching the peak amplitude corresponding to 10% MVC, after which point it was held constant for two seconds. (b) Discharge rate, in pulses per second, of motor units 40 and 60 over the course of the simulation, showing the relationship between intensity and discharge rate to demonstrate rate coding.

4.3.2 Incorporation of Tissue Mechanics Predictions

The contact pressure between tibial and talus articular cartilage during ankle plantar flexion was measured throughout the simulation (Figure 4.8). The peak pressure achieved during the simulation was 14.89 MPa. The inclusion of cartilage and contact interaction in the integrated model demonstrates the ability of the model to perform more complex biomechanical analyses than is possible using rigid body simulations.

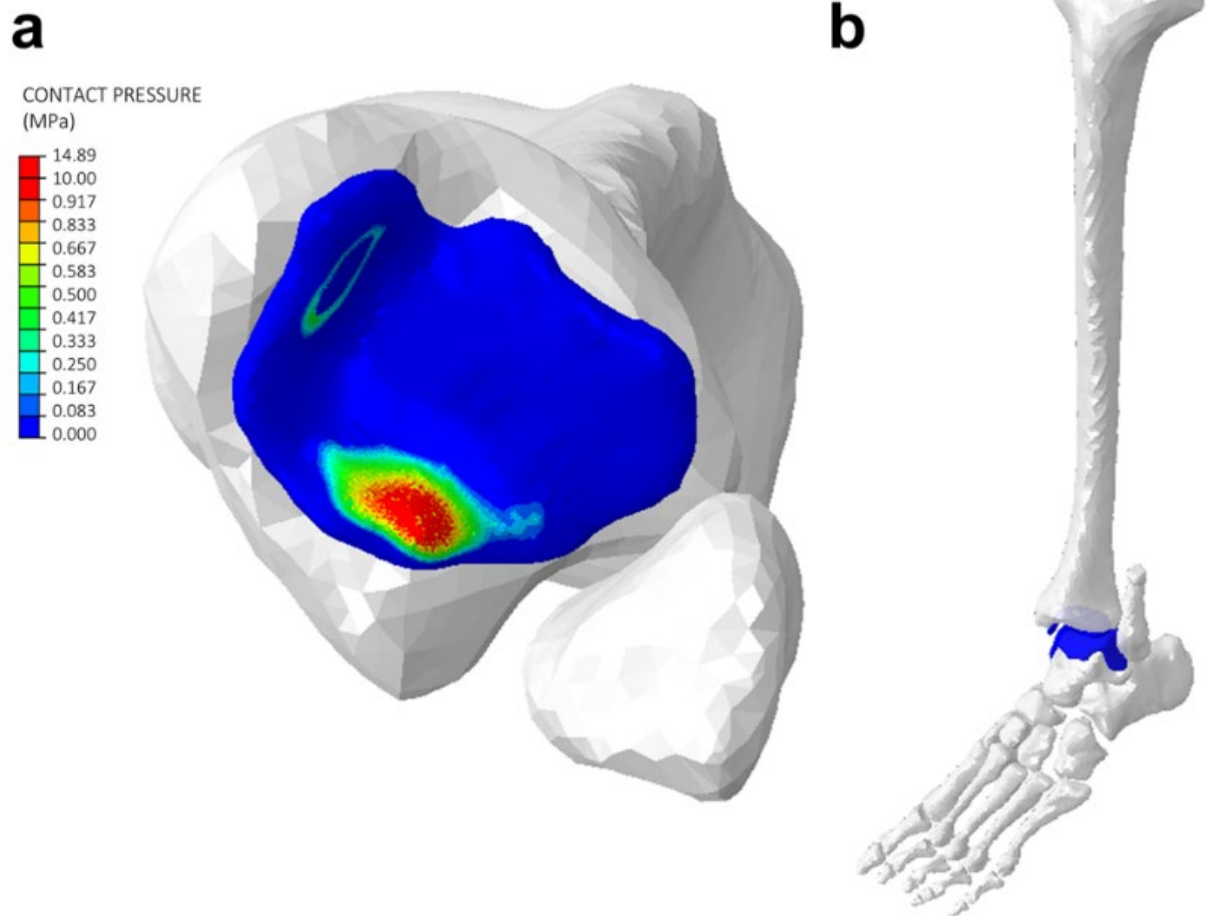


Figure 4.8 (a) Contour map showing contact pressure on the tibia articular cartilage during ankle plantarflexion. The region of higher contact pressure is located posteriorly. (b) Plantarflexed position of the tibia-talus joint.

4.4 Discussion

The direct agreement between the muscle force output from Kim³⁸ and the single motor neuron FE NMS model verifies that the NEURON model has been accurately integrated with the Abaqus FE environment. The capability of the integrated NMS model with neuronal network to exhibit the principles of motor unit recruitment and rate coding show that the model accurately simulates the neural drive to muscles.

The independent computation times for the NEURON and Abaqus components of the FE NMS model highlight the ability to increase complexity in either component without modifying the run time in the other. A benefit of using NetPyNE to scale the neural architecture to be more representative of physiological muscle is that the software has been designed to run parallelized simulations, which in future models will increase efficiency of large-scale neuronal networks.

The efficacy of this model to accurately simulate various neural commands at different muscle force levels was shown through the verification of the principles of motor unit recruitment and rate coding. This illustrated the ability of the NMS model to accurately simulate skeletal muscle forces needed to drive in vivo movement. It was shown that the NMS model is capable of robust neural architecture scaling, and is therefore applicable to muscles of all sizes throughout the body.

The interspike intervals presented at 10% MVC (Figures 4.5d, 4.6d) are slightly lower than those reported by Thompson et al.¹¹⁶ for soleus motor unit spontaneous discharges, but spontaneous discharges would be more variable, and therefore have longer interspike interval times than stimulated motor units. Also, the decrease in interspike interval with an increase in intensity is physiologically accurate across both stimulation profiles (Figures 4.5 and 4.6) because discharge rate increases with intensity resulting in a decrease in time between subsequent discharges. In the ramp-up and ramp-down stimulation profile (Figure 4.6), there was an asymmetry in discharge rates between recruitment and de-recruitment of motor units, as was shown to be the case in soleus motor units during experimental recordings.¹¹⁷

The average motor neuron diameters within recruitment threshold ranges were calculated to verify the motor unit size distribution in the neuronal network. The average diameters were comparable to previously published values,¹¹⁸ showing that the recruitment threshold distribution occurring due to the exponential diameters of the motor units matched in vivo values. The discharge rates at 10% MVC ranged from 7.03 to 11.28 pulses per second (pps) (Figure 4.8). These values are within the range found for motor unit discharge rates at recruitment and peak force.¹¹⁴

The model developed here has a similar neural architecture to previously developed fully predictive NMS models.²⁴⁻³¹ The neuron geometry in this model was reconstructed from a cat spinal motor neuron,³⁸ which is more complex and physiologically accurate than previous models which built two-compartment cell models.^{27,28} The most similar model is the five-component model (motor neuron pool, muscle spindles, half-sarcomere, fiber, and continuum mechanics) of Heidlauf and Röhrle.²⁵ Our model incorporates a program designed specifically for neuronal network simulations, rather than using a general bioengineering software.²⁵ This has potential benefit because it is easier to create larger, complex neural architectures, as exhibited here with a 310 motor neuron pool compared to 10 in prior literature.²⁵ This can be accomplished with NetPyNE, as was done in the motor unit recruitment and rate coding verification, since it was designed to facilitate the development of large neuronal networks using NEURON.

In this study we presented a FE model with a simplified representation of the ankle with two point-to-point muscles to serve as proof-of-concept that a NEURON simulation can be integrated with a FE environment to create a fully predictive NMS

model. Musculoskeletal model complexity in the isometric contraction simulations used for verification of software integration is similar to that of existing NMS models with rigid-body musculoskeletal representation.²⁹⁻³¹ The inclusion of contact interaction at the tibia-talus joint takes the analysis a step further to demonstrate that additional FE model complexity can easily be incorporated within our integrated FE NMS environment.

Abaqus is frequently used for more complex musculoskeletal simulations, including the use of three-dimensional muscle geometries and sophisticated biomaterial models.¹¹⁹⁻¹²³ Future work on this model will focus on incorporating these components so that the FE NMS model may be extended to perform more complex biomechanical analyses that better capture physiological interactions and dependencies between the nervous and musculoskeletal systems. Additionally, the neuronal network developed in this study will facilitate future work with complex three-dimensional muscle architectures because the current network can be minimally modified to include muscle fiber innervation.

The scope of this work was limited to verifying integration between the software platforms and the resulting muscle force generation from the FE NMS model. Limitations of the current model are the simplicity of the musculoskeletal model, lack of validation against kinematic data, and neural signal only including input from motor neurons. The complexity of the FE model should be increased in future work to incorporate three-dimensional representations of musculature and ligaments and validate the resulting human motions against experimental data. Additionally, the NEURON simulation should be expanded to include additional cell types representative of electrical signals generated in the brain necessary to study neurodegenerative disorders.

This is the first time that a predictive neural architecture has been integrated into a musculoskeletal finite element environment. A fully predictive NMS model capable of running within a FE environment, as presented in this work, can aid in improving our understanding of how the neural and musculoskeletal systems work together to generate and control movement in both healthy and pathological individuals. In the future, this model may be applied to study neurodegenerative and neurodevelopmental movement disorders.

4.5 Data Availability

The neuromuscular model used here to validate results from the finite element framework was provided by ModelDB (Kim³⁸) at the publicly available repository: <https://senselab.med.yale.edu/ModelDB/> (Model #235769). The integrated model is also available on ModelDB (Model #267184).

4.6 Acknowledgements

This work was supported in part by the NIH National Institute of Arthritis and Musculoskeletal and Skin Diseases, National Institute of Biomedical Imaging and Bioengineering, and the National Institute of Child Health and Human Development grant U01 AR072989. This material is based upon work supported by the National Science Foundation Graduate Research Fellowship Program under Grant No. 1946726. Any opinions, findings, and conclusions or recommendations expressed in this material are those of the author(s) and do not necessarily reflect the views of the National Science Foundation. The authors would like to thank the NIH BRAIN Initiative and instructors at the University of Missouri for motivating this study.

4.7 Author Justification

V.L.V.: design of the study, developed the integrated model, performed all analyses, prepared figures, primary writer. L.D.H.: contributed to verification of in vivo neural behavior, provided guidance on neural modeling. D.R.H.: contributed to FE model development and interpretation of results. K.B.S.: contributed to FE model development and interpretation of results. C.K.F.: study concept, design of the study, interpretation of results. All authors contributed to editing and revision of the manuscript for intellectual content.

CHAPTER FIVE: NEUROMUSCULOSKELETAL MOUSE HINDLIMB MODEL TO
STUDY THE EFFECT OF NEURAL CHANGES IN INDIVIDUALS WITH
NEURODEVELOPMENTAL DISORDERS

Victoria L. Volk^{1,2}

Rochelle M. Hines³

Dustin J. Hines³

Clare K. Fitzpatrick²

Will be submitted for publication to *Scientific Reports*:

Summer 2022

¹*Micron School of Materials Science and Engineering, Boise State University, Boise, ID,
USA*

²*Mechanical and Biomedical Engineering, Boise State University, Boise, ID, USA*

³*Department of Psychology, University of Nevada Las Vegas, Las Vegas, NV, USA*

5.1 Background

Neurodevelopmental disorders stem from irregularities in the nervous system during early brain development that lead to complications in function, behavior, and movement. Neurodevelopmental disorders are commonly diagnosed during childhood but these disorders can persist to cause lifelong impairments. As of 2008, approximately 1 in 6 children in the United States has a developmental disability with prevalence increasing from 12.84% to 15.04% over a 12-year period.³ Examples of these conditions include autism spectrum disorders, attention deficit/hyperactivity disorder, intellectual disability, and Rett syndrome.^{4,5} Neurodevelopmental disorders can be caused by both genetic and environmental factors, or a combination of both.⁵

Studying neurodevelopmental disorders can be difficult to do especially with the challenge of performing experimental studies *in vivo*. It is not feasible to record all measurements of interest and ethical considerations must be taken when performing experimental studies with humans. Oftentimes animal studies are used to bridge this gap and information from animal experiments can be extrapolated to humans. For parameters that are unable to be measured experimentally, neuromusculoskeletal (NMS) models can provide missing information. NMS models often only include complexity in either the neuromuscular or musculoskeletal components. One type of NMS model that overcomes this is a fully predictive model. Fully predictive NMS models allow for parameterization in both the nervous and musculoskeletal systems which enables them to be used for studies of the entire motion generation feedback loop in the body.

Rett syndrome (RS) is a neurodevelopmental disorder that affects 1 out of every 10,000 female births.⁴² RS is caused by a range of genetic mutations on the methyl-CpG-

binding protein 2 (*Mecp2*).⁴¹ Females are predominantly affected by RS due to *Mecp2* being located on the X chromosome.⁴³ RS causes primary motor symptoms of a loss of purposeful hand movement, progressive changes in muscle tone, loss of speech, and, in severe cases, difficulty breathing and gait abnormalities.⁴⁴ To better treat and care for those living with RS, the underlying disease mechanism must be understood. RS was chosen as the neurodevelopmental disorder to be modeled in this study as there is already a well-developed experimental mouse model with supporting data that can be used for validation.⁴⁵ Other neurodevelopmental conditions can be studied using the work presented here once the feasibility is demonstrated in the RS population.

There are different *Mecp2* mutations that impact numerous cortical areas and have varying RS-related symptoms. It has been shown that restoration of *Mecp2* function could reverse RS.^{124, 125} This means that if the mechanisms by which varying mutations of *Mecp2* cause RS-related impairments were understood, possible treatments could be developed to restore the normal function of *Mecp2*.¹²⁶ There are existing experimental mouse models that study the effect mutations and deficiencies in *Mecp2* have on signaling in pyramidal cells.¹²⁷⁻¹²⁹ These models do not investigate *how* the changes in signaling effect movement, but rather just attribute these changes to the symptoms of RS. Other work has analyzed the effect *Mecp2* mutations have on the behavior abnormalities,^{130, 131} anxiety,¹³² and stress responses¹³³ individuals with RS experience based on *Mecp2* mutations in different brain regions and neuron types. One study tracked eye movement changes in RS to see if the signaling pathway to the oculomotor system was affected by *Mecp2* mutations.¹³⁴ These studies analyze neural signal changes stemming from RS that cause the associated motor symptoms, but fail to take the analysis

a step further to look at how the movement is changed to better understand the disease mechanism.

The goal of this work is to develop a fully predictive NMS model of a mouse hindlimb within a single software framework that can be used to study neurodevelopmental disorders. The neural model was developed to include neural morphology that may be altered to represent healthy or pathological neural morphology, so that a spectrum of neurodevelopmental states may be simulated. This is done using NEURON and Abaqus software programs for the neuromuscular and musculoskeletal components, respectively. NEURON (version 7.7.2) is an open-source, python-based simulation environment for models ranging from single neurons to networks of neurons.³⁷ Abaqus is a finite element (FE) software useful for generating complex biomechanical models that can include soft-tissue geometries and measure parameters unable to be measured experimentally, such as joint contact pressures. The fully predictive NMS mouse model described in this study was based upon a previously developed NMS model that showed the effective integration of NEURON simulations within the Abaqus environment.¹³⁵ This model will be applied to study the effect that changes in neural morphology have on resulting joint kinematics.

5.2 Finite Element Model Development

The musculoskeletal portion of the model was developed in Abaqus/Explicit (Simulia, Providence, RI). Mouse bone and cartilage geometries were extracted from a mouse micro computed tomography (uCT) scan. The scan was taken on a 22-week-old mouse using a Skyscan machine at 70 kV, 142 uA, and a 0.5 mm Al filter. All geometries were segmented in Amira (Thermo Fisher Scientific, 2020, Waltham, MA) (Figure 5.1).

Hypermesh (Altair Hyperworks, Troy, MI) was used to generate FE meshes from the STL surface representations. Bony geometries are modeled as rigid (R3D3) elements. Cartilage of the femur, tibia, and patella were modeled as three-dimensional tetrahedral elements (C3D10M). The cartilage are also modeled as rigid, but cartilage-to-cartilage contact behavior is represented by a linear pressure-overclosure relationship.¹⁰⁴ Muscles were represented as point-to-point connectors based upon a publicly available, previously validated rigid-body mouse hindlimb model.¹³⁶ The knee flexors and extensors were scaled and aligned to the segmented geometry for use in this study (Figure 5.2).

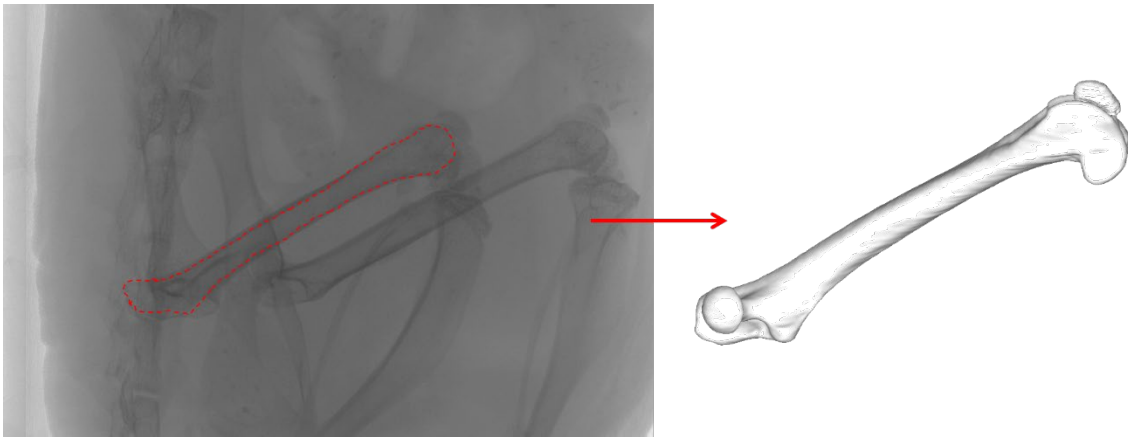


Figure 5.1 Three-dimensional bone and cartilage geometries were segmented from a mouse uCT scan.

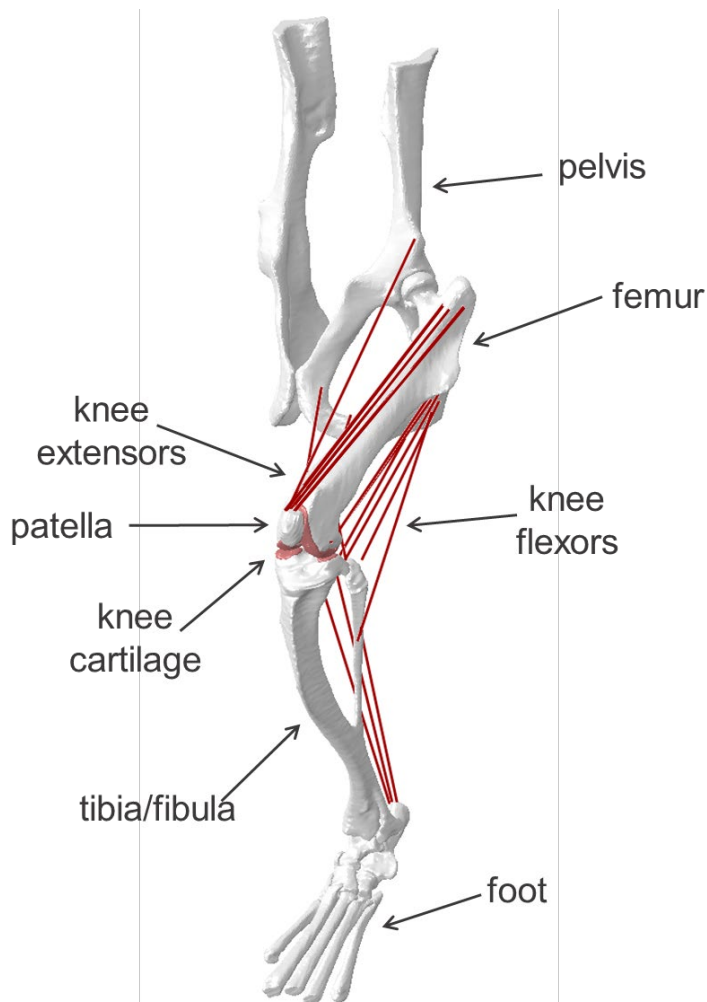


Figure 5.2 Abaqus FE musculoskeletal geometries from the pelvis to the foot. Articular cartilage is included at the knee.

The model simulates the kinematics of a full gait cycle of the mouse hindlimb. The hip joint is kinematically controlled and modeled as a ball and socket joint. The ankle joint is modeled as a one degree of freedom hinge joint and is also kinematically controlled. The tibiofemoral and patellofemoral joints are controlled by the muscle forces of the knee flexors and extensors. The knee is modeled as six degree-of-freedom joint. Contact mechanics, including contact pressure and contact area, are measured throughout the gait cycle at the tibiofemoral and patellofemoral joints (Figure 5.3).

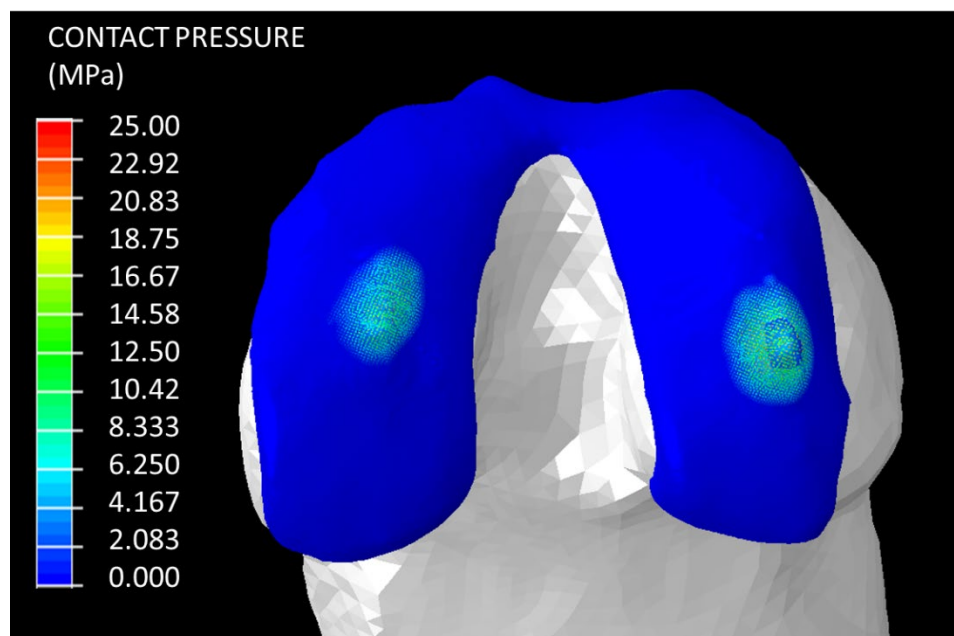


Figure 5.3 Contour map showing contact pressure on the femur articular cartilage at the tibiofemoral joint during the propulsion phase of the gait cycle.

5.3 Neural Model Development

The neural portion of this model simulates the signal traveling from pyramidal cells in the brain to motor neurons in the spinal cord (Figure 5.4). Pyramidal cells were included in the model to incorporate the electrical signal from the brain to motor neuron pool that was lacking in the previous integrated NMS model. Pyramidal cells were specifically chosen as they have been shown to have morphological and ionic channel changes due to neurodevelopmental conditions.^{45, 137} The neural models^{38, 138} were available from the public repository ModelDB.¹⁰⁵ The pyramidal cell is a layer 5 cell that is representative of cells found in the premotor cortex.¹³⁸ The original pyramidal cell geometry included a soma, apical dendrites, basal dendrites, and axon. The geometry was modified to include an axon initial segment (AIS) to allow for morphology changes caused by RS. All pyramidal cell components include passive membrane channels representative of leak currents in the cell used to maintain homeostatic membrane

potential. The soma also includes potassium (voltage-gated, calcium-activated, persistent, transient), sodium (persistent, transient), and calcium (low voltage activated, high voltage activated) property definitions. The apical dendrites have potassium (voltage-gated, calcium-activated), sodium (transient), and calcium (low voltage activated, high voltage activated) channels included as well. The motor neuron geometry includes a soma, axon hillock, AIS, and a reduced dendritic tree to improve signal reception. All components of the motor neuron exhibit passive properties. In the soma, axon hillock, and AIS there are potassium (delayed rectifier, calcium-activated) and sodium (fast, persistent) channels to elicit spiking that occurs in all active cells. Calcium channels (N-type, L-type) are in the dendritic tree and soma to help with bursting necessary for proper muscle force generation.

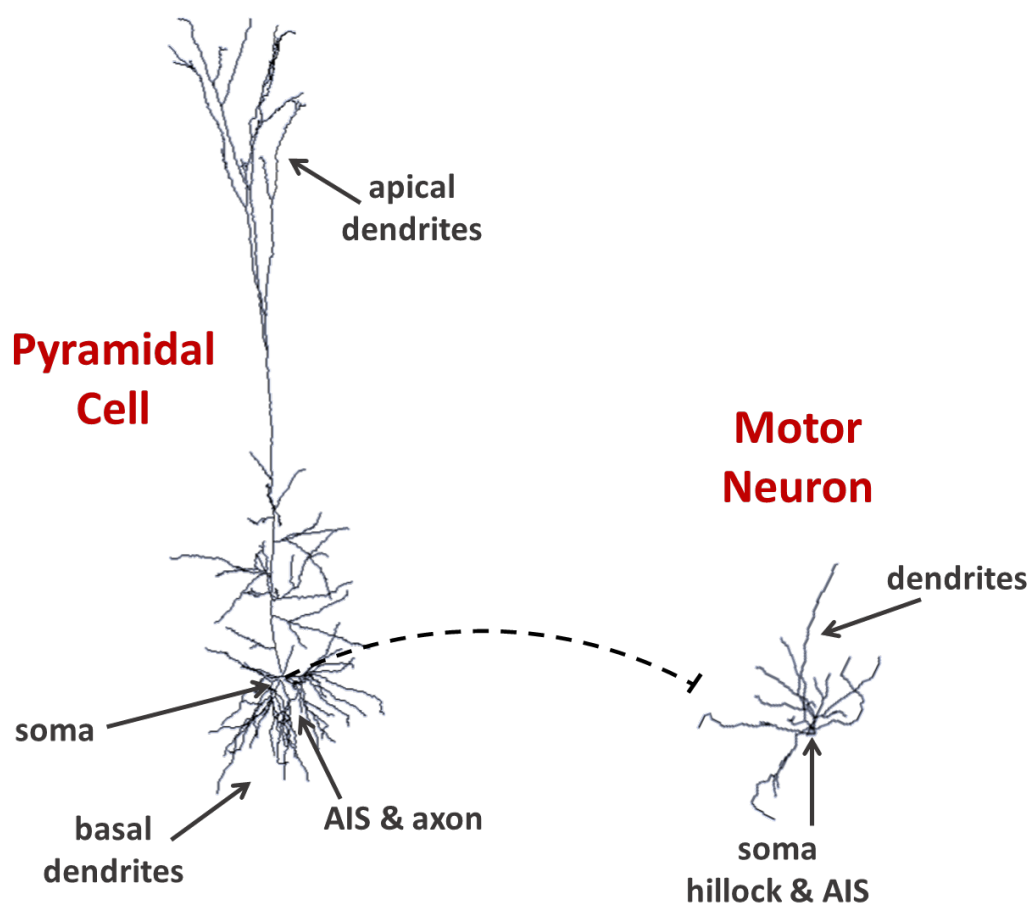


Figure 5.4 Three-dimensional representations of the pyramidal cell and motor neuron geometries included in the neural portion of the integrated NMS model.

The entire neural component of the model includes pyramidal cells sending signals to a motor neuron pool of 180 motor neurons. This network was generated using NetPyNE (Networks in python and NEURON).¹⁰⁹ The motor neuron pool was scaled according to experimental studies of the number of motor neurons that stimulate the quadriceps femoris muscles of a mouse hindlimb.¹³⁹ The neuromuscular junction is comprised of modules for calcium dynamics, activation dynamics, and force production.³⁸ Force production is based on a Hill-type muscle model with active and passive force generating elements. Even though Hill-type muscle models are simplified

representations, they have been shown to accurately reproduce experimentally measured in vivo muscle forces.¹⁴⁰

5.3.1 Neuron Morphology Changes

Previous experimental work has found alterations to axon morphology in mice with deletion of *Mecp2* that replicates the features of human individuals with severe RS.^{124, 141} The AIS in pyramidal cells in the premotor cortex is found to have a higher tortuosity and be shorter in *Mecp2* mice compared to wildtype, healthy controls (Figure 5.5).⁴⁵ These morphology changes lead to disrupted signaling that causes impaired movements and decreases in fine motor coordination. These changes are seen on AIS staining using beta-IV spectrin, ankyrin G, and neurofascin as AIS markers.

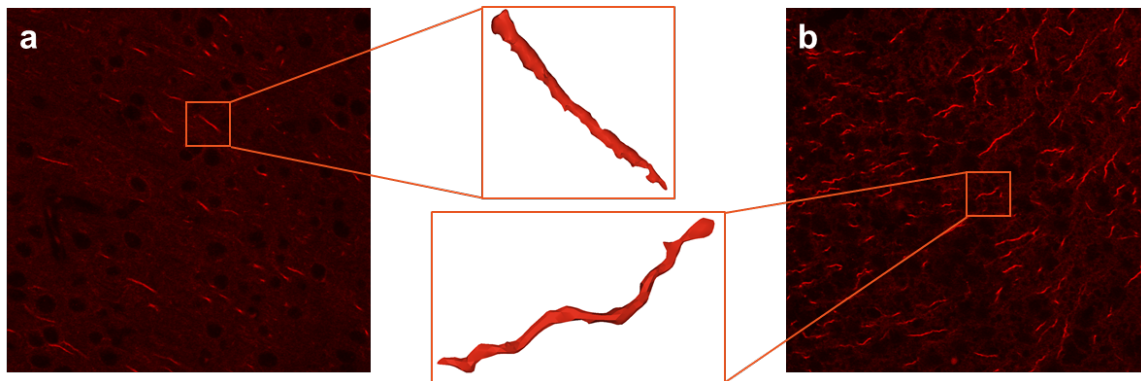


Figure 5.5 (a) Healthy wildtype AIS compared to (b) AIS with increased tortuosity, a morphological change associated with RS.

To better quantify the relationship between AIS tortuosity in wildtype and RS groups, tortuosity was quantified using root mean square error (RMSE), arc-to-chord ratio, and rate of angular change. AIS geometries were segmented using Amira software (Thermo Fisher Scientific, 2020, Waltham, MA) from scans showing AIS staining (Figure 5.5). From each mouse ten axons were segmented. Each axon was turned into a point cloud of vertex locations that was fit with a line-of-best-fit in three-dimensional

space (Figure 5.6a). This line of best fit is representative of what would be the center of a perfectly straight AIS. Each point cloud was then normalized to 30 points along the length of the axon (Figure 5.6b). The RMSE was measured as the average distance between each of the points along the axon to the straight line-of-best-fit in all three dimensions. The arc-to-cord ratio is measured as the Euclidian distance between each of the 30 points divided by the length of the straight line (Figure 5.6b). To quantify the rate of angular change, the angle between each point along the length of the axon was calculated and summed for the total amount the AIS corkscrewed in space.

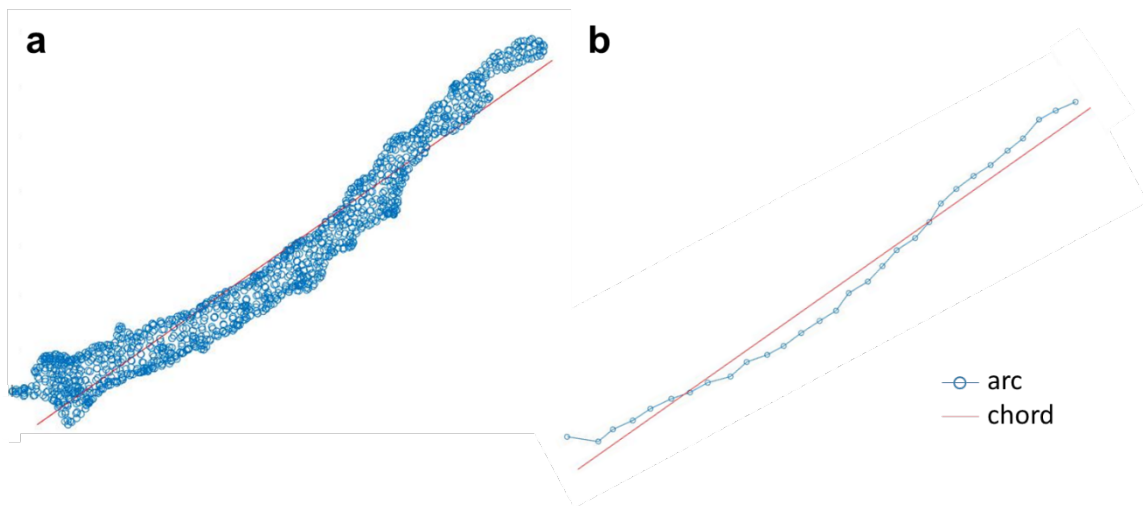


Figure 5.6 (a) Point cloud of vertices (blue) from STL segmentation of AIS fit with a line-of-best-fit (red). (b) Normalization of point cloud to 30 centroids (blue) along length of AIS. The arc-to-chord ratio is the Euclidian distance between the centroids (blue line) divided by the length of the line-of-best-fit (red).

5.4 Current Status

The work completed on this project includes the creation of the Abaqus FE musculoskeletal model and the NEURON neuromuscular model independently. The FE model includes geometry and material properties for mouse hindlimb bones, knee articular cartilage, and knee flexor and extensor point-to-point muscle connectors. The

model simulates a full gait cycle of a mouse hindlimb. The NEURON model includes all cellular geometries with various ion channels embedded to elicit spiking activity. The motor neuron pool has been scaled to an appropriate size for the quadriceps muscles of a mouse hindlimb. AIS tortuosity has been quantified for the wildtype control mice throughout their time course development at 5 weeks, 10 weeks, and adult stages for comparison to diseased populations. The protocol is set up to run the remaining *Mecp2* stained AIS scans as soon as they are available.

5.5 Ongoing Work

The development of the fully predictive NMS mouse hindlimb model is ongoing. Current work includes software integration, model validation, and application of AIS morphology changes. Software integration involves communication between the NEURON and Abaqus portions of the model which occurs through an Abaqus-specific Fortran subroutine (vuamp). A NEURON simulation will be performed for 100 ms, or a smaller time increment if the length of the overall simulation is in a different order of magnitude, and the resulting muscle activation levels from the neuron spiking will be used to calculate the muscle forces input into the Abaqus FE musculoskeletal simulation (Figure 5.7). The quadriceps muscles, rectus femoris, vastus intermedius, vastus medialis, and vastus lateralis, will be controlled by the NEURON simulation. The total quadriceps muscle force will be calculated as the summation of the twitch muscle force of each motor unit innervating the muscles. The hamstrings muscle forces will be controlled to counterbalance the quadriceps movements to perform the necessary joint motions. Ligaments and tendons will also be included at the knee to help with joint control when applying the muscle forces. After the 100 ms from the initial NEURON simulation has

completed in Abaqus, the current muscle parameters will be sent back to NEURON to run the next updated portion of the simulation (Figure 5.7). At this stage, computational run time will be assessed to see if it would be beneficial to parallelize the NEURON simulation to improve run time with the increased complexity of including pyramidal cells and scaling the motor neuron pool.

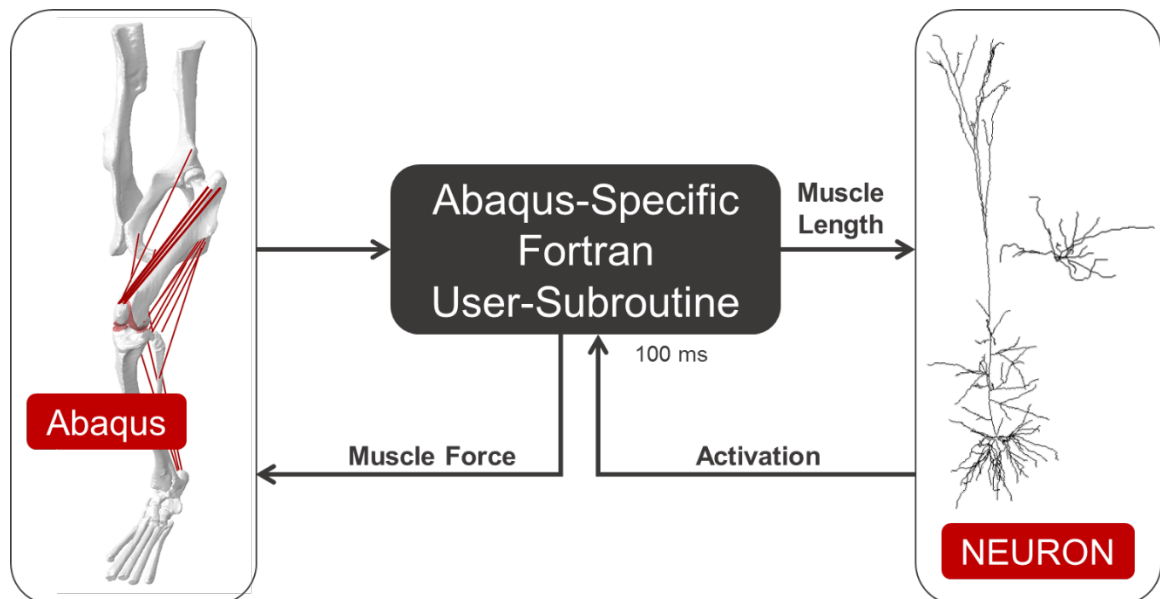


Figure 5.7 Flow of information in integrated NMS model. A NEURON simulation runs for a set amount of time, which is 100 ms in this example. The activation from NEURON is input into the muscle force calculation. The force is then applied to the quadriceps muscles in the Abaqus musculoskeletal mouse model.

Model validation of the healthy baseline model against experimental data must be performed to ensure accurate results and applications of the integrated NMS mouse model. Experimental data is being collected by collaborators at University of Nevada Las Vegas. This includes electroencephalography (EEG) and electromyography (EMG) data collected simultaneously with kinematics during purposeful movement in mice. The EEG will be used to compare to neural spike outputs from NEURON that are used to calculate muscle activation levels. Muscle force outputs from the FE portion of the integrated

model will be verified against EMG. Joint kinematics will be compared to joint location in space determined from video recordings during experimental trials.

The integrated and validated NMS healthy baseline mouse hindlimb model will be applied to study the effect of AIS morphological changes associated with RS on movement. The AIS geometry of the pyramidal cells will be modified to account for the increased tortuosity quantified in *Mecp2* mice. The resulting changes in kinematics and contact mechanics at the knee during gait will be studied. The sensitivity of morphological changes will be studied by varying the degree of tortuosity and the number of pyramidal cells affected by an increase in tortuosity. Modeling the effects neural morphological changes have on movement in RS and other neurodevelopmental disorders, using a fully predictive NMS model, can help to inform about the underlying disease mechanisms and lead to potential treatment options.

5.6 Discussion

The development of a fully predictive NMS mouse hindlimb model in the integrated NEURON-Abaqus framework enables studies of underlying mechanisms of neurodevelopmental diseases. When this work is successfully concluded, there will be a healthy baseline mouse hindlimb model that can be adapted in both the neural and musculoskeletal portions to study the resulting effects. The potential of this baseline model for applicability to neurodevelopmental disorders will be shown through the modification of AIS tortuosity, representative of individuals with RS, to investigate the resulting movement-related effects. This can lead to analyzes on the effects of additional modifications to the model, such as modifying ion channel distributions or ion current parameters, to see if they overcome the movement variations resulting from the AIS

morphology changes. Results of these analyzes could inform treatment options such as medications targeting specific ion channels.

The applicability of this model to study neurodevelopmental disorders will be demonstrated using morphology changes associated with RS, but the model can be modified to study other neurodevelopmental and neurodegenerative conditions.

Intellectual disability (ID) is a neurodevelopmental condition that has been found to impact the $\alpha 2$ subunit of GABA_A receptors which are localized in AIS synapses in chandelier cells that leads to irregular spiking activity.¹³⁷ The baseline mouse NMS model could be adapted in the neural portion to include chandelier cell geometries with inhibiting signals being sent to the pyramidal cells to investigate how this affects the musculoskeletal joint motion. Additionally, the model could be used to study the effects of stimulation from electrodes implanted during deep brain stimulation (DBS) to treat motor symptoms of Parkinson's Disease, a neurodegenerative condition. Different initial activation profiles could be applied to the pyramidal cells that represent various modulation profiles applied using DBS electrodes to see which profile optimally relieves motor symptoms.

A key benefit of fully predictive NMS models is the capability to modify parameters in both the neural and musculoskeletal components. On the neural side, the geometry of any cellular component can be modified to represent varying shapes or include additional features that modify signaling, such as adding myelination to an axon. There is also large variability in the types of ion channels used, as well as varying the properties of a given ionic channel. The FE musculoskeletal model can simulate different motions depending on what would showcase the differences due to a specific

neurodevelopmental or neurodegenerative condition, such as one with more fine motor control like a string pull task. The FE model is currently set-up to primarily study the knee, but different muscles and soft tissues could be included in the additional joints depending on the motion most affected by the neural disorder. Changes in soft tissue outputs, such as tissue stress and strain, might be indicative of changes in fine motor control that represent early onset changes resulting from neurodevelopmental and neurodegenerative conditions. This will be tested using the integrated NEURON and FE model, as soft tissue representations are not possible within simpler musculoskeletal models, such as rigid-body modeling.

Studying neurodevelopmental and neurodegenerative diseases is more feasible to study experimentally in mice compared to humans. Findings related to changes in neural morphology and signaling in mice can be extrapolated to humans. The current integrated fully predictive NMS model is of a mouse hindlimb, but it can be modified to incorporate human musculoskeletal geometry and scaled to represent human neural circuits. Kinematic changes in the human and mouse models could then be compared to see if the changes at the mouse-level are equivalent in humans. Additional future work should include three-dimensional muscle geometries to better represent *in vivo* muscle force generation where each motor unit will directly stimulate a set of embedded active muscle fibers for muscle contraction.

The development of a fully predictive mouse hindlimb model built within a FE framework can aid in improving our understanding of neurodevelopmental and neurodegenerative conditions. A healthy baseline, wildtype model exists that can be modified to analyze the effect changes in neural morphology and signaling have on

musculoskeletal function to study underlying disease mechanisms and develop targeted treatment options.

5.7 Acknowledgements

The authors would like to thank Scott Birks and Dr. Gunes Uzer in the Mechanical Adaptations Lab (Boise State University) for providing the mouse hindlimb uCT used in this study for the FE bone and cartilage geometries. This material is based upon work supported by the National Science Foundation Graduate Research Fellowship Program under Grant No. 1946726. Any opinions, findings, and conclusions or recommendations expressed in this material are those of the author(s) and do not necessarily reflect the views of the National Science Foundation.

5.8 Author Justification

V.L.V.: design of the study, developed the model, performed all analyses, prepared figures, primary writer. R.M.H.: experimental data collection, interpretation of results. D.J.H.: experimental data collection, interpretation of results. C.K.F.: study concept, design of the study, interpretation of results, editing and revision of writing.

CHAPTER SIX: CONCLUSION

Neurodegenerative and neurodevelopmental diseases stem from irregularities in the nervous system during early brain development or due to the aging process that lead to complications in function, behavior, and movement. There are treatment options for many of these diseases, but none that cure the root cause of the condition. The underlying disease mechanisms must be better understood to design targeted treatment options. This body of work showcases the development of computational tools and models that can be applied to study neurodegenerative and neurodevelopmental disorders.

Chapter Two details the development of an automated measurement system used to measure the accuracy of electrodes implanted during robot-assisted asleep deep brain stimulation (DBS). DBS is a surgical treatment option for Parkinson's Disease (PD), a neurodegenerative condition. The electrodes implanted during DBS help to regulate atypical firing patterns in the basal ganglia region of the brain to alleviate the primary motor symptoms of PD, including tremor, dystonia, and rigidity.⁸⁻¹¹ Accurate placement of electrodes is key to successful clinical outcomes, and the developed measurement system removes human bias for increased precision of accuracy measures. It also can analyze large cohorts of patient implants in a reduced amount of time. By quantifying electrode placement accuracy in this manner, informed improvements can be made to the robotic technology and surgical procedure to further improve patient outcomes following surgery. This work was published in the *Annals of Biomedical Engineering* in February 2019.⁹⁸

Chapter Three applies the automated measurement system developed to measure electrode accuracy in DBS to pedicle screw placement during spinal fusion procedures. Spinal fusions are used to treat a variety of degenerative musculoskeletal conditions including spondylolisthesis, lumbar stenosis, and degenerative disc disease.⁴⁶⁻⁴⁸ Screws are placed in the pedicle region of the vertebrae to act as anchor points for rods that restrict movement between the attached vertebrae. Precise screw placement is required for optimal clinical outcomes, similar to electrodes in DBS. A breach outside of the pedicle region can cause impairments to the spinal cord. The automated measurement system was modified to measure pedicle screw placement accuracy in all three anatomical planes. The uncertainty associated with the necessary step of fusing preoperative to intra- or postoperative images was quantified to capture the measurement system variability. This measurement process quantifies additional pedicle screw placement accuracy metrics compared to the conventional grading system scales that group placements by amount of pedicle breach. Information about implanted screw location as it directly relates to the target can inform technological developments and surgical procedure changes. This study was submitted for publication to the *Journal of Neurosurgery: Spine* in April 2022.

Chapter Four summarizes the development of a fully predictive neuromusculoskeletal (NMS) model within a single finite element (FE) framework. This model improves upon existing models by integrating two software programs that allow for complexity in both the neuromuscular and musculoskeletal modeling components. NEURON is an open-source program designed for creating models ranging in size from a single neuron to large scale neuronal networks. Abaqus is a FE solver that has been used

to create complex biomechanics models that incorporate soft tissue definitions and measure properties unable to be determined experimentally, such as contact pressures. The integration of NEURON and Abaqus within a single framework allows for parameterization within either system to study the effects that neural and musculoskeletal components have on one another. This interaction can help to better understand the underlying mechanisms of neurodegenerative and neurodevelopmental conditions. This study was published in *Scientific Reports* in November 2021.¹³⁵

Chapter Five applies the integrated NMS model to study neurodegenerative and neurodevelopmental diseases. A fully predictive NMS mouse hindlimb model was developed in the integrated software platform to study Rett syndrome (RS). RS is a neurodevelopmental disorder caused by a mutation of the *Mecp2* gene with hallmark motor symptoms of a loss of purposeful hand movement, changes in muscle tone, and a loss of speech.⁴⁴ The neural component of the model was expanded to include pyramidal cells representative of the brain sending signals to the spinal cord. The musculoskeletal component of the model is of a three-dimensional mouse hindlimb with soft tissue inclusion at the knee joint. This mouse hindlimb NMS model will be used to study the effect axon initial segment morphology changes associated with RS, including an increased tortuosity, have on joint movement. This will help to expand the knowledge about the underlying mechanisms of RS and provide a platform for understanding how to overcome the effects of neural morphological changes caused by neurodevelopmental diseases. This work is in preparation to be submitted to *Scientific Reports* in Summer 2022.

Collectively, this body of work has made the following contributions to the scientific community: (1) An automated measurement algorithm for determining the accuracy of surgically implanted devices during procedures used to treat neurodegenerative and degenerative musculoskeletal conditions. The uncertainty associated with image fusion during said procedures was quantified to better inform improvements in surgical procedures and robotic technological advances. (2) Integrated neuromusculoskeletal modeling framework built by incorporating NEURON simulations within a FE environment. This simulation framework allows for complexity in both neural and musculoskeletal components, which is needed to study motion generation in the body and underlying disease mechanisms in neurodegenerative and neurodevelopmental diseases. (3) A fully predictive NMS mouse hindlimb model developed in the integrated FE framework. This model will be applied to study the effect changes in neural morphology will have on resulting joint movement due to neurodevelopmental and neurodegenerative diseases, and how movement changes can be used as a marker for early diagnosis.

Future directions for this work include continuing to build on the complexity of the integrated NMS model and using it for additional applications to neural conditions. The neural modeling component of the NMS model should be improved to include additional anatomical geometries, including interneurons, and to enhance connectivity between different neurons to better represent signals travelling from the brain to spinal cord. The FE musculoskeletal portion of the NMS model should be advanced to incorporate three-dimensional musculature with embedded active fibers that are directly activated by the electrical signaling from the motor neuron pool in the NEURON

simulation. The integrated NMS model can be applied to study additional movements related to RS that show early-onset motor changes, such as a string pull task, which requires finer motor control than gait. Other disorders can also be studied, such as the effect the loss of Gabra2-1 receptors plays on movement in individuals with intellectual disabilities.¹³⁷ The automated measurement system ought to be applied to measure accuracy of different surgical procedures as well as measure changes in accuracy due to new instrumentation and robotic devices. The quantified uncertainty in the fusion process should be accounted for when developing new robotic technology, particularly to develop an automated approach that would remove manual intervention in any step of the measurement process. This work encompasses a range of research that uses computational models and algorithms to study the underlying mechanisms and design targeted treatment options for neurodegenerative and neurodevelopmental disorders.

REFERENCES

1. Brown RC, Lockwood AH, Sonawane BR. Neurodegenerative diseases: an overview of environmental risk factors. *Environ Health Perspect*. 2005;113(9):1250-6. Epub 2005/09/06. doi: 10.1289/ehp.7567. PubMed PMID: 16140637; PMCID: PMC1280411.
2. Checkoway H, Lundin JI, Kelada SN. Neurodegenerative diseases. *IARC Sci Publ*. 2011(163):407-19. PubMed PMID: 22997874.
3. Boyle CA, Boulet S, Schieve LA, Cohen RA, Blumberg SJ, Yeargin-Allsopp M, Visser S, Kogan MD. Trends in the prevalence of developmental disabilities in US children, 1997-2008. *Pediatrics*. 2011;127(6):1034-42. Epub 2011/05/25. doi: 10.1542/peds.2010-2989. PubMed PMID: 21606152.
4. Morris-Rosendahl DJ, Crocq MA. Neurodevelopmental disorders-the history and future of a diagnostic concept. *Dialogues Clin Neurosci*. 2020;22(1):65-72. Epub 2020/07/24. doi: 10.31887/DCNS.2020.22.1/macrocq. PubMed PMID: 32699506; PMCID: PMC7365295.
5. van Loo KM, Martens GJ. Genetic and environmental factors in complex neurodevelopmental disorders. *Current genomics*. 2007;8(7):429-44. Epub 2007/11/01. doi: 10.2174/138920207783591717. PubMed PMID: 19412416; PMCID: PMC2647153.
6. Yang W, Hamilton JL, Kopil C, Beck JC, Tanner CM, Albin RL, Ray Dorsey E, Dahodwala N, Cintina I, Hogan P, Thompson T. Current and projected future economic burden of Parkinson's disease in the U.S. *NPJ Parkinsons Dis*. 2020;6:15. Epub 2020/07/16. doi: 10.1038/s41531-020-0117-1. PubMed PMID: 32665974; PMCID: PMC7347582.

7. Marras C, Beck JC, Bower JH, Roberts E, Ritz B, Ross GW, Abbott RD, Savica R, Van Den Eeden SK, Willis AW, Tanner CM, Parkinson's Foundation PG. Prevalence of Parkinson's disease across North America. *NPJ Parkinsons Dis.* 2018;4:21. Epub 2018/07/14. doi: 10.1038/s41531-018-0058-0. PubMed PMID: 30003140; PMCID: PMC6039505.
8. Hariz GM, Lindberg M, Bergenheim AT. Impact of thalamic deep brain stimulation on disability and health-related quality of life in patients with essential tremor. *J Neurol Neurosurg Psychiatry.* 2002;72(1):47-52. Epub 2002/01/11. doi: 10.1136/jnnp.72.1.47. PubMed PMID: 11784825; PMCID: PMC1737710.
9. Herzog J, Volkmann J, Krack P, Kopper F, Potter M, Lorenz D, Steinbach M, Klebe S, Hamel W, Schrader B, Weinert D, Muller D, Mehdorn HM, Deuschl G. Two-year follow-up of subthalamic deep brain stimulation in Parkinson's disease. *Mov Disord.* 2003;18(11):1332-7. Epub 2003/11/26. doi: 10.1002/mds.10518. PubMed PMID: 14639676.
10. Jankovic J. Parkinson's disease: clinical features and diagnosis. *J Neurol Neurosurg Psychiatry.* 2008;79(4):368-76. Epub 2008/03/18. doi: 10.1136/jnnp.2007.131045. PubMed PMID: 18344392.
11. Rodriguez-Oroz MC, Obeso JA, Lang AE, Houeto JL, Pollak P, Rehncrona S, Kulisevsky J, Albanese A, Volkmann J, Hariz MI, Quinn NP, Speelman JD, Guridi J, Zamarbide I, Gironell A, Molet J, Pascual-Sedano B, Pidoux B, Bonnet AM, Agid Y, Xie J, Benabid AL, Lozano AM, Saint-Cyr J, Romito L, Contarino MF, Scerrati M, Fraix V, Van Blercom N. Bilateral deep brain stimulation in Parkinson's disease: a multicentre study with 4 years follow-up. *Brain.* 2005;128(Pt 10):2240-9. Epub 2005/06/25. doi: 10.1093/brain/awh571. PubMed PMID: 15975946.
12. Schrader B, Hamel W, Weinert D, Mehdorn HM. Documentation of electrode localization. *Mov Disord.* 2002;17(S3):S167-S74. doi: 10.1002/mds.10160.
13. Levine D. Deep Brain Stimulation for Mental Illnesses Raises Ethical Concerns. *leapsmag.* 2018.

14. Kruger MT, Kurtev-Rittstieg R, Kagi G, Naseri Y, Hagele-Link S, Brugger F. Evaluation of Automatic Segmentation of Thalamic Nuclei through Clinical Effects Using Directional Deep Brain Stimulation Leads: A Technical Note. *Brain Sci.* 2020;10(9). Epub 2020/09/23. doi: 10.3390/brainsci10090642. PubMed PMID: 32957437; PMCID: PMC7563258.
15. McClelland S, 3rd, Ford B, Senatus PB, Winfield LM, Du YE, Pullman SL, Yu Q, Frucht SJ, McKhann GM, 2nd, Goodman RR. Subthalamic stimulation for Parkinson disease: determination of electrode location necessary for clinical efficacy. *Neurosurg Focus.* 2005;19(5):E12. Epub 2006/01/10. PubMed PMID: 16398462.
16. Burchiel KJ, McCartney S, Lee A, Raslan AM. Accuracy of deep brain stimulation electrode placement using intraoperative computed tomography without microelectrode recording. *J Neurosurg.* 2013;119(2):301-6. Epub 2013/06/04. doi: 10.3171/2013.4.JNS122324. PubMed PMID: 23724986.
17. Farina D, Negro F. Common synaptic input to motor neurons, motor unit synchronization, and force control. *Exercise and sport sciences reviews.* 2015;43(1):23-33. Epub 2014/11/13. doi: 10.1249/jes.0000000000000032. PubMed PMID: 25390298.
18. Fernandez J, Zhang J, Heidlauf T, Sartori M, Besier T, Rohrlé O, Lloyd D. Multiscale musculoskeletal modelling, data-model fusion and electromyography-informed modelling. *Interface Focus.* 2016;6(2):20150084. Epub 2016/04/07. doi: 10.1098/rsfs.2015.0084. PubMed PMID: 27051510; PMCID: PMC4759749.
19. Lloyd DG, Besier TF. An EMG-driven musculoskeletal model to estimate muscle forces and knee joint moments in vivo. *Journal of Biomechanics.* 2003;36(6):765-76. doi: 10.1016/s0021-9290(03)00010-1.
20. Ma Y, Xie S, Zhang Y. A patient-specific EMG-driven neuromuscular model for the potential use of human-inspired gait rehabilitation robots. *Comput Biol Med.* 2016;70:88-98. Epub 2016/01/26. doi: 10.1016/j.combiomed.2016.01.001. PubMed PMID: 26807802.

21. Sartori M, Yavuz US, Farina D. In Vivo Neuromechanics: Decoding Causal Motor Neuron Behavior with Resulting Musculoskeletal Function. *Sci Rep*. 2017;7(1):13465. Epub 2017/10/19. doi: 10.1038/s41598-017-13766-6. PubMed PMID: 29044165; PMCID: PMC5647446.
22. Wiedemann LG, Jayaneththi VR, Kimpton J, Chan A, Muller MA, Hogan A, Lim E, Wilson NC, McDaid AJ. Neuromuscular characterisation in Cerebral Palsy using hybrid Hill-type models on isometric contractions. *Comput Biol Med*. 2018;103:269-76. Epub 2018/11/09. doi: 10.1016/j.compbiomed.2018.10.027. PubMed PMID: 30408656.
23. Sartori M, Llyod DG, Farina D. Neural Data-Driven Musculoskeletal Modeling for Personalized Neurorehabilitation Technologies. *IEEE Trans Biomed Eng*. 2016;63(5):879-93. Epub 2016/04/06. doi: 10.1109/TBME.2016.2538296. PubMed PMID: 27046865.
24. Callahan DM, Umberger BR, Kent-Braun JA. A computational model of torque generation: neural, contractile, metabolic and musculoskeletal components. *PLoS One*. 2013;8(2):e56013. Epub 2013/02/14. doi: 10.1371/journal.pone.0056013. PubMed PMID: 23405245; PMCID: PMC3566067.
25. Heidlauf T, Rohrlé O. Modeling the chemoelectromechanical behavior of skeletal muscle using the parallel open-source software library OpenCMISS. *Comput Math Methods Med*. 2013;2013:517287. Epub 2013/12/19. doi: 10.1155/2013/517287. PubMed PMID: 24348739; PMCID: PMC3855958.
26. Siddiqi A, Poosapadi Arjunan S, Kumar DK. Computational model to investigate the relative contributions of different neuromuscular properties of tibialis anterior on force generated during ankle dorsiflexion. *Med Biol Eng Comput*. 2018;56(8):1413-23. Epub 2018/01/18. doi: 10.1007/s11517-018-1788-1. PubMed PMID: 29335929.

27. Cisi RR, Kohn AF. Simulation system of spinal cord motor nuclei and associated nerves and muscles, in a Web-based architecture. *J Comput Neurosci*. 2008;25(3):520-42. Epub 2008/05/29. doi: 10.1007/s10827-008-0092-8. PubMed PMID: 18506610.
28. Elias LA, Watanabe RN, Kohn AF. Spinal mechanisms may provide a combination of intermittent and continuous control of human posture: predictions from a biologically based neuromusculoskeletal model. *PLoS Comput Biol*. 2014;10(11):e1003944. Epub 2014/11/14. doi: 10.1371/journal.pcbi.1003944. PubMed PMID: 25393548; PMCID: PMC4230754.
29. Schuurmans J, van der Helm FC, Schouten AC. Relating reflex gain modulation in posture control to underlying neural network properties using a neuromusculoskeletal model. *J Comput Neurosci*. 2011;30(3):555-65. Epub 2010/09/25. doi: 10.1007/s10827-010-0278-8. PubMed PMID: 20865310; PMCID: PMC3108017.
30. Sreenivasa M, Ayusawa K, Nakamura Y. Modeling and Identification of a Realistic Spiking Neural Network and Musculoskeletal Model of the Human Arm, and an Application to the Stretch Reflex. *IEEE Trans Neural Syst Rehabil Eng*. 2016;24(5):591-602. Epub 2015/09/24. doi: 10.1109/TNSRE.2015.2478858. PubMed PMID: 26394432.
31. Stienen AH, Schouten AC, Schuurmans J, van der Helm FC. Analysis of reflex modulation with a biologically realistic neural network. *J Comput Neurosci*. 2007;23(3):333-48. Epub 2007/05/16. doi: 10.1007/s10827-007-0037-7. PubMed PMID: 17503169; PMCID: PMC2799624.
32. Seth A, Hicks JL, Uchida TK, Habib A, Dembia CL, Dunne JJ, Ong CF, DeMers MS, Rajagopal A, Millard M, Hamner SR, Arnold EM, Yong JR, Lakshmikanth SK, Sherman MA, Ku JP, Delp SL. OpenSim: Simulating musculoskeletal dynamics and neuromuscular control to study human and animal movement. *PLoS Comput Biol*. 2018;14(7):e1006223. Epub 2018/07/27. doi: 10.1371/journal.pcbi.1006223. PubMed PMID: 30048444; PMCID: PMC6061994.

33. Cook RD, Malkus DS, Plesha ME, Witt RJ. Concepts and Applications of Finite Element Analysis: John Wiley & Sons, Inc.; 2007.
34. Thelen DG, Won Choi K, Schmitz AM. Co-simulation of neuromuscular dynamics and knee mechanics during human walking. *J Biomech Eng*. 2014;136(2):021033. Epub 2014/01/07. doi: 10.1115/1.4026358. PubMed PMID: 24390129; PMCID: PMC4023657.
35. Lin YC, Walter JP, Pandy MG. Predictive Simulations of Neuromuscular Coordination and Joint-Contact Loading in Human Gait. *Ann Biomed Eng*. 2018;46(8):1216-27. Epub 2018/04/20. doi: 10.1007/s10439-018-2026-6. PubMed PMID: 29671152.
36. Farina D, Negro F, Dideriksen JL. The effective neural drive to muscles is the common synaptic input to motor neurons. *J Physiol*. 2014;592(16):3427-41. Epub 2014/05/27. doi: 10.1113/jphysiol.2014.273581. PubMed PMID: 24860172; PMCID: PMC4229341.
37. Hines ML, Carnevale NT. NEURON: a tool for neuroscientists. *The Neuroscientist : a review journal bringing neurobiology, neurology and psychiatry*. 2001;7(2):123-35. Epub 2001/08/11. doi: 10.1177/107385840100700207. PubMed PMID: 11496923.
38. Kim H. Muscle length-dependent contribution of motoneuron Cav1.3 channels to force production in model slow motor unit. *J Appl Physiol*. 2017;123(1):88-105. Epub 2017/03/25. doi: 10.1152/jappphysiol.00491.2016. PubMed PMID: 28336534.
39. Fuglevand AJ, Winter DA, Patla AE. Models of recruitment and rate coding organization in motor-unit pools. *J Neurophysiol*. 1993;70(6):2470-88. Epub 1993/12/01. doi: 10.1152/jn.1993.70.6.2470. PubMed PMID: 8120594.
40. Henneman E, Somjen G, Carpenter DO. FUNCTIONAL SIGNIFICANCE OF CELL SIZE IN SPINAL MOTONEURONS. *J Neurophysiol*. 1965;28:560-80. Epub 1965/05/01. doi: 10.1152/jn.1965.28.3.560. PubMed PMID: 14328454.

41. Kozinetz CA, Skender ML, MacNaughton N, Almes MJ, Schultz RJ, Percy AK, Glaze DG. Epidemiology of Rett syndrome: a population-based registry. *Pediatrics*. 1993;91(2):445-50. Epub 1993/02/01. PubMed PMID: 8424025.
42. Tarquinio DC, Percy AK. Chapter 19 - Rett Syndrome: Clinical Aspects. In: Sala C, Verpelli C, editors. *Neuronal and Synaptic Dysfunction in Autism Spectrum Disorder and Intellectual Disability*. San Diego: Academic Press; 2016. p. 301-23.
43. Neul JL, Zoghbi HY. Rett syndrome: a prototypical neurodevelopmental disorder. *The Neuroscientist : a review journal bringing neurobiology, neurology and psychiatry*. 2004;10(2):118-28. Epub 2004/04/09. doi: 10.1177/1073858403260995. PubMed PMID: 15070486.
44. Chahrour M, Zoghbi HY. The story of Rett syndrome: from clinic to neurobiology. *Neuron*. 2007;56(3):422-37. Epub 2007/11/09. doi: 10.1016/j.neuron.2007.10.001. PubMed PMID: 17988628.
45. Rodriguez RA, Nam YE, Hines DJ, Hines RM. Axon initial segment tortuosity and synaptic connectivity underlie prodromal impairments in motor coordination in a model of Rett syndrome. Final Preparation for Submission.
46. Barry JJ, Sing DC, Vail TP, Hansen EN. Early Outcomes of Primary Total Hip Arthroplasty After Prior Lumbar Spinal Fusion. *J Arthroplasty*. 2017;32(2):470-4. Epub 2016/09/01. doi: 10.1016/j.arth.2016.07.019. PubMed PMID: 27578537.
47. Fan Y, Du JP, Liu JJ, Zhang JN, Qiao HH, Liu SC, Hao DJ. Accuracy of pedicle screw placement comparing robot-assisted technology and the free-hand with fluoroscopy-guided method in spine surgery: An updated meta-analysis. *Medicine (Baltimore)*. 2018;97(22):e10970. Epub 2018/06/01. doi: 10.1097/MD.0000000000010970. PubMed PMID: 29851848; PMCID: PMC6392558.

48. Martin BI, Mirza SK, Spina N, Spiker WR, Lawrence B, Brodke DS. Trends in Lumbar Fusion Procedure Rates and Associated Hospital Costs for Degenerative Spinal Diseases in the United States, 2004 to 2015. *Spine (Phila Pa 1976)*. 2019;44(5):369-76. Epub 2018/08/04. doi: 10.1097/BRS.0000000000002822. PubMed PMID: 30074971.
49. Mobbs RJ, Phan K, Malham G, Seex K, Rao PJ. Lumbar interbody fusion: techniques, indications and comparison of interbody fusion options including PLIF, TLIF, MI-TLIF, OLIF/ATP, LLIF and ALIF. *J Spine Surg*. 2015;1(1):2-18. Epub 2016/09/30. doi: 10.3978/j.issn.2414-469X.2015.10.05. PubMed PMID: 27683674; PMCID: PMC5039869.
50. Teng I, Han J, Phan K, Mobbs R. A meta-analysis comparing ALIF, PLIF, TLIF and LLIF. *J Clin Neurosci*. 2017;44:11-7. Epub 2017/07/06. doi: 10.1016/j.jocn.2017.06.013. PubMed PMID: 28676316.
51. Chen C, Cao X, Zou L, Hao G, Zhou Z, Zhang G. Minimally invasive unilateral versus bilateral technique in performing single-segment pedicle screw fixation and lumbar interbody fusion. *J Orthop Surg Res*. 2015;10:112. Epub 2015/07/17. doi: 10.1186/s13018-015-0253-1. PubMed PMID: 26179281; PMCID: PMC4504127.
52. Gertzbein SD, Robbins SE. Accuracy of pedicular screw placement in vivo. *Spine (Phila Pa 1976)*. 1990;15(1):11-4. Epub 1990/01/01. doi: 10.1097/00007632-199001000-00004. PubMed PMID: 2326693.
53. Schatlo B, Molliqaj G, Cuvinciuc V, Kotowski M, Schaller K, Tessitore E. Safety and accuracy of robot-assisted versus fluoroscopy-guided pedicle screw insertion for degenerative diseases of the lumbar spine: a matched cohort comparison. *J Neurosurg Spine*. 2014;20(6):636-43. Epub 2014/04/15. doi: 10.3171/2014.3.SPINE13714. PubMed PMID: 24725180.

54. Youkilis AS, Quint DJ, McGillicuddy JE, Papadopoulos SM. Stereotactic navigation for placement of pedicle screws in the thoracic spine. *Neurosurgery*. 2001;48(4):771-8; discussion 8-9. Epub 2001/04/27. doi: 10.1097/00006123-200104000-00015. PubMed PMID: 11322437.
55. Rampersaud YR, Pik JH, Salonen D, Farooq S. Clinical accuracy of fluoroscopic computer-assisted pedicle screw fixation: a CT analysis. *Spine (Phila Pa 1976)*. 2005;30(7):E183-90. Epub 2005/04/02. doi: 10.1097/01.brs.0000157490.65706.38. PubMed PMID: 15803068.
56. Walker CT, Kakarla UK, Chang SW, Sonntag VKH. History and advances in spinal neurosurgery. *J Neurosurg Spine*. 2019;31(6):775-85. Epub 2019/12/02. doi: 10.3171/2019.9.SPINE181362. PubMed PMID: 31786543.
57. Ghasem A, Sharma A, Greif DN, Alam M, Maaieh MA. The Arrival of Robotics in Spine Surgery: A Review of the Literature. *Spine (Phila Pa 1976)*. 2018;43(23):1670-7. Epub 2018/04/20. doi: 10.1097/BRS.0000000000002695. PubMed PMID: 29672420.
58. Joseph JR, Smith BW, Liu X, Park P. Current applications of robotics in spine surgery: a systematic review of the literature. *Neurosurg Focus*. 2017;42(5):E2. Epub 2017/05/04. doi: 10.3171/2017.2.FOCUS16544. PubMed PMID: 28463618.
59. Lefranc M, Peltier J. Evaluation of the ROSA Spine robot for minimally invasive surgical procedures. *Expert review of medical devices*. 2016;13(10):899-906. Epub 2016/09/21. doi: 10.1080/17434440.2016.1236680. PubMed PMID: 27649314.
60. Li HM, Zhang RJ, Shen CL. Accuracy of Pedicle Screw Placement and Clinical Outcomes of Robot-assisted Technique Versus Conventional Freehand Technique in Spine Surgery From Nine Randomized Controlled Trials: A Meta-analysis. *Spine (Phila Pa 1976)*. 2020;45(2):E111-E9. Epub 2019/08/14. doi: 10.1097/BRS.0000000000003193. PubMed PMID: 31404053.

61. Yu L, Chen X, Margalit A, Peng H, Qiu G, Qian W. Robot-assisted vs freehand pedicle screw fixation in spine surgery - a systematic review and a meta-analysis of comparative studies. *Int J Med Robot*. 2018;14(3):e1892. Epub 2018/02/20. doi: 10.1002/rcs.1892. PubMed PMID: 29457345.
62. Liu H, Chen W, Wang Z, Lin J, Meng B, Yang H. Comparison of the accuracy between robot-assisted and conventional freehand pedicle screw placement: a systematic review and meta-analysis. *Int J Comput Assist Radiol Surg*. 2016;11(12):2273-81. Epub 2016/06/24. doi: 10.1007/s11548-016-1448-6. PubMed PMID: 27334134.
63. Gao S, Lv Z, Fang H. Robot-assisted and conventional freehand pedicle screw placement: a systematic review and meta-analysis of randomized controlled trials. *Eur Spine J*. 2018;27(4):921-30. Epub 2017/10/17. doi: 10.1007/s00586-017-5333-y. PubMed PMID: 29032475.
64. Kantelhardt SR, Martinez R, Baerwinkel S, Burger R, Giese A, Rohde V. Perioperative course and accuracy of screw positioning in conventional, open robotic-guided and percutaneous robotic-guided, pedicle screw placement. *Eur Spine J*. 2011;20(6):860-8. Epub 2011/03/09. doi: 10.1007/s00586-011-1729-2. PubMed PMID: 21384205; PMCID: PMC3099153.
65. Hyun SJ, Kim KJ, Jahng TA, Kim HJ. Minimally Invasive Robotic Versus Open Fluoroscopic-guided Spinal Instrumented Fusions: A Randomized Controlled Trial. *Spine (Phila Pa 1976)*. 2017;42(6):353-8. Epub 2016/07/12. doi: 10.1097/BRS.0000000000001778. PubMed PMID: 27398897.
66. Roser F, Tatagiba M, Maier G. Spinal robotics: current applications and future perspectives. *Neurosurgery*. 2013;72 Suppl 1:12-8. Epub 2013/01/04. doi: 10.1227/NEU.0b013e318270d02c. PubMed PMID: 23254800.

67. Keric N, Doenitz C, Haj A, Rachwal-Czyzewicz I, Renovanz M, Wesp DMA, Boor S, Conrad J, Brawanski A, Giese A, Kantelhardt SR. Evaluation of robot-guided minimally invasive implantation of 2067 pedicle screws. *Neurosurg Focus*. 2017;42(5):E11. Epub 2017/05/04. doi: 10.3171/2017.2.FOCUS16552. PubMed PMID: 28463624.
68. Medtronic. Technical Specifications: Mazor X Stealth Edition Robotic Guidance System2020.
69. Lefranc M, Zouitina Y, Tir M, Merle P, Ouendo M, Constans JM, Godefroy O, Peltier J, Krystkowiak P. Asleep Robot-Assisted Surgery for the Implantation of Subthalamic Electrodes Provides the Same Clinical Improvement and Therapeutic Window as Awake Surgery. *World Neurosurg*. 2017;106:602-8. Epub 2017/07/25. doi: 10.1016/j.wneu.2017.07.047. PubMed PMID: 28735132.
70. Ho AL, Ali R, Connolly ID, Henderson JM, Dhall R, Stein SC, Halpern CH. Awake versus asleep deep brain stimulation for Parkinson's disease: a critical comparison and meta-analysis. *J Neurol Neurosurg Psychiatry*. 2018;89(7):687-91. Epub 2017/03/03. doi: 10.1136/jnnp-2016-314500. PubMed PMID: 28250028.
71. Abosch A, Timmermann L, Bartley S, Rietkerk HG, Whiting D, Connolly PJ, Lanctin D, Hariz MI. An international survey of deep brain stimulation procedural steps. *Stereotact Funct Neurosurg*. 2013;91(1):1-11. Epub 2012/11/17. doi: 10.1159/000343207. PubMed PMID: 23154755.
72. Chen T, Mirzadeh Z, Chapple KM, Lambert M, Shill HA, Moguel-Cobos G, Troster AI, Dhall R, Ponce FA. Clinical outcomes following awake and asleep deep brain stimulation for Parkinson disease. *J Neurosurg*. 2018;130(1):109-20. Epub 2018/03/17. doi: 10.3171/2017.8.JNS17883. PubMed PMID: 29547091.
73. Jacob RL, Geddes J, McCartney S, Burchiel KJ. Cost analysis of awake versus asleep deep brain stimulation: a single academic health center experience. *J Neurosurg*. 2016;124(5):1517-23. Epub 2015/11/21. doi: 10.3171/2015.5.JNS15433. PubMed PMID: 26587660.

74. Krack P, Batir A, Van Blercom N, Chabardes S, Fraix V, Ardouin C, Koudsie A, Limousin PD, Benazzouz A, LeBas JF, Benabid A, Pollak P. Five-year follow-up of bilateral stimulation of the subthalamic nucleus in advanced Parkinson's disease. *New England Journal of Medicine*. 2003;349(20):1925-34.
75. Khoo VS, Dearnaley DP, Finnigan DJ, Padhani A, Tanner SF, Leach MO. Magnetic resonance imaging (MRI): considerations and applications in radiotherapy treatment planning. *Radiotherapy and oncology : journal of the European Society for Therapeutic Radiology and Oncology*. 1997;42(1):1-15. Epub 1997/01/01. doi: 10.1016/s0167-8140(96)01866-x. PubMed PMID: 9132820.
76. Barrett JF, Keat N. Artifacts in CT: Recognition and Avoidance 2004;24(6):1679-91. doi: 10.1148/rg.246045065. PubMed PMID: 15537976.
77. Foltynie T, Zrinzo L, Martinez-Torres I, Tripoliti E, Petersen E, Holl E, Aviles-Olmos I, Jahanshahi M, Hariz M, Limousin P. MRI-guided STN DBS in Parkinson's disease without microelectrode recording: efficacy and safety. *J Neurol Neurosurg Psychiatry*. 2011;82(4):358-63. Epub 2010/06/24. doi: 10.1136/jnnp.2010.205542. PubMed PMID: 20571041.
78. Mirzadeh Z, Chapple K, Lambert M, Evidente VG, Mahant P, Ospina MC, Samanta J, Moguel-Cobos G, Salins N, Lieberman A, Troster AI, Dhall R, Ponce FA. Parkinson's disease outcomes after intraoperative CT-guided "asleep" deep brain stimulation in the globus pallidus internus. *J Neurosurg*. 2016;124(4):902-7. Epub 2015/10/10. doi: 10.3171/2015.4.JNS1550. PubMed PMID: 26452116.
79. Mirzadeh Z, Chapple K, Lambert M, Dhall R, Ponce FA. Validation of CT-MRI fusion for intraoperative assessment of stereotactic accuracy in DBS surgery. *Mov Disord*. 2014;29(14):1788-95. Epub 2014/11/08. doi: 10.1002/mds.26056. PubMed PMID: 25377213.

80. Ostrem JL, Ziman N, Galifianakis NB, Starr PA, Luciano MS, Katz M, Racine CA, Martin AJ, Markun LC, Larson PS. Clinical outcomes using ClearPoint interventional MRI for deep brain stimulation lead placement in Parkinson's disease. *J Neurosurg.* 2016;124(4):908-16. Epub 2015/10/27. doi: 10.3171/2015.4.JNS15173. PubMed PMID: 26495947.
81. Faria C, Erhagen W, Rito M, De Momi E, Ferrigno G, Bicho E. Review of Robotic Technology for Stereotactic Neurosurgery. *IEEE Rev Biomed Eng.* 2015;8:125-37. Epub 2015/05/09. doi: 10.1109/RBME.2015.2428305. PubMed PMID: 25955851.
82. Zimmermann M, Krishnan R, Raabe A, Seifert V. Robot-assisted Navigated Neuroendoscopy. *Neurosurgery.* 2002;51(6):1446-52. doi: 10.1227/01.NEU.0000309121.39958.26 %J Neurosurgery.
83. Vadera S, Chan A, Lo T, Gill A, Morenkova A, Phielipp NM, Hermanowicz N, Hsu FP. Frameless Stereotactic Robot-Assisted Subthalamic Nucleus Deep Brain Stimulation: Case Report. *World Neurosurg.* 2017;97:762 e11- e14. Epub 2015/11/21. doi: 10.1016/j.wneu.2015.11.009. PubMed PMID: 26585721.
84. Lefranc M, Capel C, Pruvot-Ocean AS, Fichten A, Desenclos C, Toussaint P, Le Gars D, Peltier J. Frameless robotic stereotactic biopsies: a consecutive series of 100 cases. *J Neurosurg.* 2015;122(2):342-52. Epub 2014/11/08. doi: 10.3171/2014.9.JNS14107. PubMed PMID: 25380111.
85. Joskowicz L, Shamir R, Freiman M, Shoham M, Zehavi E, Umansky F, Shoshan Y. Image-guided system with miniature robot for precise positioning and targeting in keyhole neurosurgery. *Comput Aided Surg.* 2006;11(4):181-93. Epub 2006/10/14. doi: 10.3109/10929080600909351. PubMed PMID: 17038306.
86. Ho AL, Pendharkar AV, Brewster R, Martinez DL, Jaffe RA, Xu LW, Miller KJ, Halpern CH. Frameless Robot-Assisted Deep Brain Stimulation Surgery: An Initial Experience. *Operative neurosurgery (Hagerstown, Md).* 2019;17(4):424-31. Epub 2019/01/11. doi: 10.1093/ons/opy395. PubMed PMID: 30629245.

87. von Langsdorff D, Paquis P, Fontaine D. In vivo measurement of the frame-based application accuracy of the Neuromate neurosurgical robot. *J Neurosurg*. 2015;122(1):191-4. Epub 2014/11/02. doi: 10.3171/2014.9.JNS14256. PubMed PMID: 25361490.
88. Neudorfer C, Hunsche S, Hellmich M, El Majdoub F, Maarouf M. Comparative Study of Robot-Assisted versus Conventional Frame-Based Deep Brain Stimulation Stereotactic Neurosurgery. *Stereotact Funct Neurosurg*. 2018;96(5):327-34. Epub 2018/11/28. doi: 10.1159/000494736. PubMed PMID: 30481770.
89. American College of Radiology. MR accreditation program testing instructions. [https://www.acraccreditation.org/~media/ACRAccreditation/Documents/MRI/MR AccreditationTestingInstructions.pdf](https://www.acraccreditation.org/~media/ACRAccreditation/Documents/MRI/MR%20AccreditationTestingInstructions.pdf). Revised 2018.
90. Geevarghese R, O'Gorman Tuura R, Lumsden DE, Samuel M, Ashkan K. Registration Accuracy of CT/MRI Fusion for Localisation of Deep Brain Stimulation Electrode Position: An Imaging Study and Systematic Review. *Stereotact Funct Neurosurg*. 2016;94(3):159-63. Epub 2016/06/20. doi: 10.1159/000446609. PubMed PMID: 27318464.
91. Bjercknes S, Skogseid IM, Saehle T, Dietrichs E, Toft M. Surgical site infections after deep brain stimulation surgery: frequency, characteristics and management in a 10-year period. *PLoS One*. 2014;9(8):e105288. Epub 2014/08/15. doi: 10.1371/journal.pone.0105288. PubMed PMID: 25122445; PMCID: PMC4133346.
92. Devito DP, Kaplan L, Dietl R, Pfeiffer M, Horne D, Silberstein B, Hardenbrook M, Kiriyanthan G, Barzilay Y, Bruskin A, Sackerer D, Alexandrovsky V, Stuer C, Burger R, Maeurer J, Donald GD, Schoenmayr R, Friedlander A, Knoller N, Schmieder K, Pechlivanis I, Kim IS, Meyer B, Shoham M. Clinical acceptance and accuracy assessment of spinal implants guided with SpineAssist surgical robot: retrospective study. *Spine (Phila Pa 1976)*. 2010;35(24):2109-15. Epub 2010/11/17. doi: 10.1097/BRS.0b013e3181d323ab. PubMed PMID: 21079498.

93. van Dijk JD, van den Ende RP, Stramigioli S, Kochling M, Hoss N. Clinical pedicle screw accuracy and deviation from planning in robot-guided spine surgery: robot-guided pedicle screw accuracy. *Spine (Phila Pa 1976)*. 2015;40(17):E986-91. Epub 2015/05/07. doi: 10.1097/BRS.0000000000000960. PubMed PMID: 25943084.
94. Molliqaj G, Schatlo B, Alaid A, Solomiichuk V, Rohde V, Schaller K, Tessitore E. Accuracy of robot-guided versus freehand fluoroscopy-assisted pedicle screw insertion in thoracolumbar spinal surgery. *Neurosurg Focus*. 2017;42(5):E14. Epub 2017/05/04. doi: 10.3171/2017.3.FOCUS179. PubMed PMID: 28463623.
95. Solomiichuk V, Fleischhammer J, Molliqaj G, Warda J, Alaid A, von Eckardstein K, Schaller K, Tessitore E, Rohde V, Schatlo B. Robotic versus fluoroscopy-guided pedicle screw insertion for metastatic spinal disease: a matched-cohort comparison. *Neurosurg Focus*. 2017;42(5):E13. Epub 2017/05/04. doi: 10.3171/2017.3.FOCUS1710. PubMed PMID: 28463620.
96. Jiang B, Pennington Z, Azad T, Liu A, Ahmed AK, Zygorakis CC, Westbroek EM, Zhu A, Cottrill E, Theodore N. Robot-Assisted versus Freehand Instrumentation in Short-Segment Lumbar Fusion: Experience with Real-Time Image-Guided Spinal Robot. *World Neurosurg*. 2020;136:e635-e45. Epub 2020/02/01. doi: 10.1016/j.wneu.2020.01.119. PubMed PMID: 32001398.
97. Avrumova F, Morse KW, Heath M, Widmann RF, Lebl DR. Evaluation of K-wireless robotic and navigation assisted pedicle screw placement in adult degenerative spinal surgery: learning curve and technical notes. *J Spine Surg*. 2021;7(2):141-54. Epub 2021/07/24. doi: 10.21037/jss-20-687. PubMed PMID: 34296026; PMCID: PMC8261565.
98. VanSickle D, Volk V, Freeman P, Henry J, Baldwin M, Fitzpatrick CK. Electrode Placement Accuracy in Robot-Assisted Awake Deep Brain Stimulation. *Ann Biomed Eng*. 2019;47(5):1212-22. Epub 2019/02/24. doi: 10.1007/s10439-019-02230-3. PubMed PMID: 30796551.

99. Hu X, Lieberman IH. What is the learning curve for robotic-assisted pedicle screw placement in spine surgery? *Clin Orthop Relat Res.* 2014;472(6):1839-44. Epub 2013/09/21. doi: 10.1007/s11999-013-3291-1. PubMed PMID: 24048889; PMCID: PMC4016454.
100. D'Souza M, Gendreau J, Feng A, Kim LH, Ho AL, Veeravagu A. Robotic-Assisted Spine Surgery: History, Efficacy, Cost, And Future Trends. *Robot Surg.* 2019;6:9-23. Epub 2019/12/07. doi: 10.2147/RSRR.S190720. PubMed PMID: 31807602; PMCID: PMC6844237.
101. Galbusera F, Volkheimer D, Reitmaier S, Berger-Roscher N, Kienle A, Wilke HJ. Pedicle screw loosening: a clinically relevant complication? *Eur Spine J.* 2015;24(5):1005-16. Epub 2015/01/27. doi: 10.1007/s00586-015-3768-6. PubMed PMID: 25616349.
102. Marie-Hardy L, Pascal-Moussellard H, Barnaba A, Bonaccorsi R, Scemama C. Screw Loosening in Posterior Spine Fusion: Prevalence and Risk Factors. *Global Spine J.* 2020;10(5):598-602. Epub 2020/07/18. doi: 10.1177/2192568219864341. PubMed PMID: 32677565; PMCID: PMC7359691.
103. Herrera A, Ibarz E, Cegonino J, Lobo-Escolar A, Puertolas S, Lopez E, Mateo J, Gracia L. Applications of finite element simulation in orthopedic and trauma surgery. *World J Orthop.* 2012;3(4):25-41. Epub 2012/05/03. doi: 10.5312/wjo.v3.i4.25. PubMed PMID: 22550621; PMCID: PMC3329620.
104. Hume DR, Rullkoetter PJ, Shelburne KB. ReadySim: A computational framework for building explicit finite element musculoskeletal simulations directly from motion laboratory data. *Int J Numer Method Biomed Eng.* 2020:e3396. Epub 2020/08/20. doi: 10.1002/cnm.3396. PubMed PMID: 32812382.
105. McDougal RA, Morse TM, Carnevale T, Marengo L, Wang R, Migliore M, Miller PL, Shepherd GM, Hines ML. Twenty years of ModelDB and beyond: building essential modeling tools for the future of neuroscience. *J Comput Neurosci.* 2017;42(1):1-10. Epub 2016/09/16. doi: 10.1007/s10827-016-0623-7. PubMed PMID: 27629590; PMCID: PMC5279891.

106. Spitzer VM, Whitlock DG. The visible human dataset: The anatomical platform for human simulation. *The Anatomical Record*. 1998;253(2):49-57. doi: 10.1002/(sici)1097-0185(199804)253:2<49::Aid-ar8>3.0.Co;2-9.
107. Jankowska E, Hammar I. Spinal interneurons; how can studies in animals contribute to the understanding of spinal interneuronal systems in man? *Brain research Brain research reviews*. 2002;40(1-3):19-28. Epub 2003/02/19. doi: 10.1016/s0165-0173(02)00185-6. PubMed PMID: 12589903.
108. Kim H. Muscle length-dependent contribution of motoneuron Ca(v)1.3 channels to force production in model slow motor unit. *Journal of applied physiology (Bethesda, Md : 1985)*. 2017;123(1):88-105. Epub 2017/03/25. doi: 10.1152/jappphysiol.00491.2016. PubMed PMID: 28336534.
109. Dura-Bernal S, Suter BA, Gleeson P, Cantarelli M, Quintana A, Rodriguez F, Kedziora DJ, Chadderdon GL, Kerr CC, Neymotin SA, McDougal RA, Hines M, Shepherd GM, Lytton WW. NetPyNE, a tool for data-driven multiscale modeling of brain circuits. *Elife*. 2019;8. Epub 2019/04/27. doi: 10.7554/eLife.44494. PubMed PMID: 31025934; PMCID: PMC6534378.
110. Boyd IAMRD. *Composition of peripheral nerves*. Edinburgh: E. & S. Livingstone Ltd.; 1968.
111. Buchthal F, Schmalbruch H. Motor unit of mammalian muscle. *Physiological reviews*. 1980;60(1):90-142. Epub 1980/01/01. doi: 10.1152/physrev.1980.60.1.90. PubMed PMID: 6766557.
112. Burke RE, Levine DN, Salcman M, Tsairis P. Motor units in cat soleus muscle: physiological, histochemical and morphological characteristics. *J Physiol*. 1974;238(3):503-14. Epub 1974/05/01. doi: 10.1113/jphysiol.1974.sp010540. PubMed PMID: 4277582; PMCID: PMC1330899.
113. Feinstein B, Lindegard B, Nyman E, Wohlfart G. Morphologic studies of motor units in normal human muscles. *Acta anatomica*. 1955;23(2):127-42. Epub 1955/01/01. doi: 10.1159/000140989. PubMed PMID: 14349537.

114. Holobar A, Farina D, Gazzoni M, Merletti R, Zazula D. Estimating motor unit discharge patterns from high-density surface electromyogram. *Clin Neurophysiol.* 2009;120(3):551-62. Epub 2009/02/12. doi: 10.1016/j.clinph.2008.10.160. PubMed PMID: 19208498.
115. Desmedt JE, Godaux E. Ballistic contractions in man: characteristic recruitment pattern of single motor units of the tibialis anterior muscle. *J Physiol.* 1977;264(3):673-93. Epub 1977/01/01. doi: 10.1113/jphysiol.1977.sp011689. PubMed PMID: 845820; PMCID: PMC1307786.
116. Thompson CK, Negro F, Johnson MD, Holmes MR, McPherson LM, Powers RK, Farina D, Heckman CJ. Robust and accurate decoding of motoneuron behaviour and prediction of the resulting force output. *J Physiol.* 2018;596(14):2643-59. Epub 2018/05/05. doi: 10.1113/JP276153. PubMed PMID: 29726002; PMCID: PMC6046070.
117. Oya T, Riek S, Cresswell AG. Recruitment and rate coding organisation for soleus motor units across entire range of voluntary isometric plantar flexions. *J Physiol.* 2009;587(Pt 19):4737-48. Epub 2009/08/26. doi: 10.1113/jphysiol.2009.175695. PubMed PMID: 19703968; PMCID: PMC2768026.
118. Del Vecchio A, Negro F, Felici F, Farina D. Distribution of muscle fibre conduction velocity for representative samples of motor units in the full recruitment range of the tibialis anterior muscle. *Acta Physiol (Oxf).* 2018;222(2). Epub 2017/08/02. doi: 10.1111/apha.12930. PubMed PMID: 28763156.
119. Ezquerro F, Simón A, Prado M, Pérez A. Combination of finite element modeling and optimization for the study of lumbar spine biomechanics considering the 3D thorax–pelvis orientation. *Medical Engineering & Physics.* 2004;26(1):11-22. doi: 10.1016/s1350-4533(03)00128-0.

120. Halloran JP, Erdemir A, van den Bogert AJ. Adaptive surrogate modeling for efficient coupling of musculoskeletal control and tissue deformation models. *J Biomech Eng.* 2009;131(1):011014. Epub 2008/12/03. doi: 10.1115/1.3005333. PubMed PMID: 19045930; PMCID: PMC2891249.
121. Hume DR, Navacchia A, Rullkoetter PJ, Shelburne KB. A lower extremity model for muscle-driven simulation of activity using explicit finite element modeling. *J Biomech.* 2019;84:153-60. Epub 2019/01/12. doi: 10.1016/j.jbiomech.2018.12.040. PubMed PMID: 30630624; PMCID: PMC6361714.
122. Lu YT, Zhu HX, Richmond S, Middleton J. Modelling skeletal muscle fibre orientation arrangement. *Comput Methods Biomech Biomed Engin.* 2011;14(12):1079-88. Epub 2010/10/07. doi: 10.1080/10255842.2010.509100. PubMed PMID: 20924862.
123. Navacchia A, Hume DR, Rullkoetter PJ, Shelburne KB. A computationally efficient strategy to estimate muscle forces in a finite element musculoskeletal model of the lower limb. *J Biomech.* 2019;84:94-102. Epub 2019/01/09. doi: 10.1016/j.jbiomech.2018.12.020. PubMed PMID: 30616983.
124. Guy J, Gan J, Selfridge J, Cobb S, Bird A. Reversal of neurological defects in a mouse model of Rett syndrome. *Science.* 2007;315(5815):1143-7. Epub 2007/02/10. doi: 10.1126/science.1138389. PubMed PMID: 17289941; PMCID: PMC7610836.
125. Liroy DT, Garg SK, Monaghan CE, Raber J, Foust KD, Kaspar BK, Hirrlinger PG, Kirchhoff F, Bissonnette JM, Ballas N, Mandel G. A role for glia in the progression of Rett's syndrome. *Nature.* 2011;475(7357):497-500. Epub 2011/07/01. doi: 10.1038/nature10214. PubMed PMID: 21716289; PMCID: PMC3268776.

126. Goffin D, Allen M, Zhang L, Amorim M, Wang IT, Reyes AR, Mercado-Berton A, Ong C, Cohen S, Hu L, Blendy JA, Carlson GC, Siegel SJ, Greenberg ME, Zhou Z. Rett syndrome mutation MeCP2 T158A disrupts DNA binding, protein stability and ERP responses. *Nat Neurosci.* 2011;15(2):274-83. Epub 2011/11/29. doi: 10.1038/nn.2997. PubMed PMID: 22119903; PMCID: PMC3267879.
127. Wood L, Gray NW, Zhou Z, Greenberg ME, Shepherd GM. Synaptic circuit abnormalities of motor-frontal layer 2/3 pyramidal neurons in an RNA interference model of methyl-CpG-binding protein 2 deficiency. *J Neurosci.* 2009;29(40):12440-8. Epub 2009/10/09. doi: 10.1523/JNEUROSCI.3321-09.2009. PubMed PMID: 19812320; PMCID: PMC2782478.
128. Dani VS, Nelson SB. Intact long-term potentiation but reduced connectivity between neocortical layer 5 pyramidal neurons in a mouse model of Rett syndrome. *J Neurosci.* 2009;29(36):11263-70. Epub 2009/09/11. doi: 10.1523/JNEUROSCI.1019-09.2009. PubMed PMID: 19741133; PMCID: PMC2765053.
129. Dani VS, Chang Q, Maffei A, Turrigiano GG, Jaenisch R, Nelson SB. Reduced cortical activity due to a shift in the balance between excitation and inhibition in a mouse model of Rett syndrome. *Proceedings of the National Academy of Sciences of the United States of America.* 2005;102(35):12560-5. Epub 2005/08/24. doi: 10.1073/pnas.0506071102. PubMed PMID: 16116096; PMCID: PMC1194957.
130. Gemelli T, Berton O, Nelson ED, Perrotti LI, Jaenisch R, Monteggia LM. Postnatal loss of methyl-CpG binding protein 2 in the forebrain is sufficient to mediate behavioral aspects of Rett syndrome in mice. *Biol Psychiatry.* 2006;59(5):468-76. Epub 2005/10/04. doi: 10.1016/j.biopsych.2005.07.025. PubMed PMID: 16199017.

131. Samaco RC, Mandel-Brehm C, Chao HT, Ward CS, Fyffe-Maricich SL, Ren J, Hyland K, Thaller C, Maricich SM, Humphreys P, Greer JJ, Percy A, Glaze DG, Zoghbi HY, Neul JL. Loss of MeCP2 in aminergic neurons causes cell-autonomous defects in neurotransmitter synthesis and specific behavioral abnormalities. *Proceedings of the National Academy of Sciences of the United States of America*. 2009;106(51):21966-71. Epub 2009/12/17. doi: 10.1073/pnas.0912257106. PubMed PMID: 20007372; PMCID: PMC2799790
L.L.C. The authors do not advocate or recommend ongoing cerebrospinal fluid (CSF) analysis in girls with Rett syndrome, as it does not contribute to the treatment or diagnosis of the disorder.
132. Adachi M, Autry AE, Covington HE, 3rd, Monteggia LM. MeCP2-mediated transcription repression in the basolateral amygdala may underlie heightened anxiety in a mouse model of Rett syndrome. *J Neurosci*. 2009;29(13):4218-27. Epub 2009/04/03. doi: 10.1523/JNEUROSCI.4225-08.2009. PubMed PMID: 19339616; PMCID: PMC3005250.
133. Fyffe SL, Neul JL, Samaco RC, Chao HT, Ben-Shachar S, Moretti P, McGill BE, Goulding EH, Sullivan E, Tecott LH, Zoghbi HY. Deletion of *Mecp2* in *Sim1*-expressing neurons reveals a critical role for MeCP2 in feeding behavior, aggression, and the response to stress. *Neuron*. 2008;59(6):947-58. Epub 2008/09/27. doi: 10.1016/j.neuron.2008.07.030. PubMed PMID: 18817733; PMCID: PMC2597031.
134. Townend GS, van de Berg R, de Breet LHM, Hiemstra M, Wagter L, Smeets E, Widdershoven J, Kingma H, Curfs LMG. Oculomotor Function in Individuals With Rett Syndrome. *Pediatr Neurol*. 2018;88:48-58. Epub 2018/10/21. doi: 10.1016/j.pediatrneurol.2018.08.022. PubMed PMID: 30340908.
135. Volk V, Hamilton L, Hume D, Shelburne K, Fitzpatrick C. Integration of Neural Architecture within a Finite Element Framework for Improved Neuromusculoskeletal Modeling. ORS Annual Conference. 2021.

136. Charles JP, Cappellari O, Spence AJ, Wells DJ, Hutchinson JR. Muscle moment arms and sensitivity analysis of a mouse hindlimb musculoskeletal model. *J Anat.* 2016;229(4):514-35. Epub 2016/05/14. doi: 10.1111/joa.12461. PubMed PMID: 27173448; PMCID: PMC5013061.
137. Hines DJ, Contreras A, Garcia B, Barker JS, Boren AJ, Moufawad El Achkar C, Moss SJ, Hines RM. Human ARHGEF9 intellectual disability syndrome is phenocopied by a mutation that disrupts collybistin binding to the GABAA receptor alpha2 subunit. *Mol Psychiatry.* 2022. Epub 2022/02/17. doi: 10.1038/s41380-022-01468-z. PubMed PMID: 35169261.
138. Hu W, Tian C, Li T, Yang M, Hou H, Shu Y. Distinct contributions of Na(v)1.6 and Na(v)1.2 in action potential initiation and backpropagation. *Nat Neurosci.* 2009;12(8):996-1002. Epub 2009/07/28. doi: 10.1038/nn.2359. PubMed PMID: 19633666.
139. McHanwell S, Biscoe TJ. The localization of motoneurons supplying the hindlimb muscles of the mouse. *Philosophical transactions of the Royal Society of London Series B, Biological sciences.* 1981;293(1069):477-508. Epub 1981/08/12. doi: 10.1098/rstb.1981.0082. PubMed PMID: 6115428.
140. Biewener AA, Wakeling JM, Lee SS, Arnold AS. Validation of Hill-type muscle models in relation to neuromuscular recruitment and force-velocity properties: predicting patterns of in vivo muscle force. *Integr Comp Biol.* 2014;54(6):1072-83. Epub 2014/06/15. doi: 10.1093/icb/icu070. PubMed PMID: 24928073; PMCID: PMC4296201.
141. Chen RZ, Akbarian S, Tudor M, Jaenisch R. Deficiency of methyl-CpG binding protein-2 in CNS neurons results in a Rett-like phenotype in mice. *Nature genetics.* 2001;27(3):327-31. Epub 2001/03/10. doi: 10.1038/85906. PubMed PMID: 11242118.